Odborný on-line časopis pro metalurgii a příbuzné obory

# Hutnické listy

## Metallurgical Journal

Speciální vydání
Special Issue

PROFESSIONAL ONLINE JOURNAL FOR METALLURGY AND RELATED FIELDS
WWW.HUTNICKELISTY.CZ

ROČNÍK/VOL. LXXIX
ROK/YEAR 2026

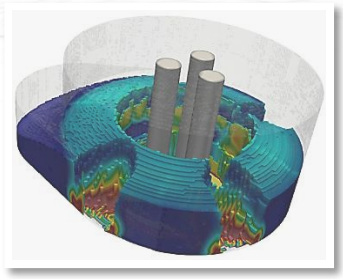

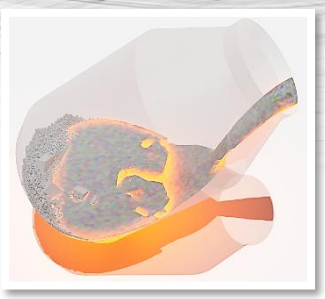

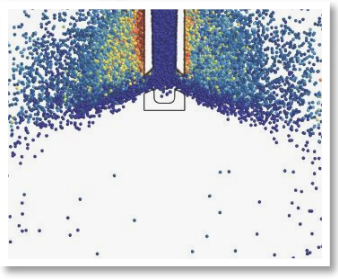

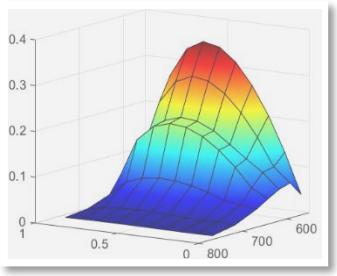


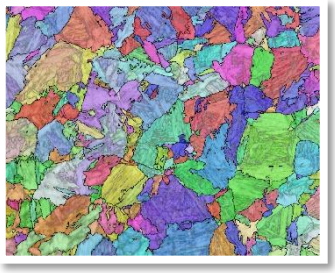

# STEELSIM 2025

## 11TH INTERNATIONAL CONFERENCE ON MODELLING AND SIMULATION OF METALLURGICAL PROCESSES IN STEELMAKING

2-4 SEPTEMBER · TŘINEC · CZ

ČESKÁ HUTNICKÁ SPOLEČNOST
CZECH METALLURGICAL SOCIETY

ISSN: 3029-8350

TŘINECKÉ ŽELEZÁRNY

OCEL
Z TŘINCE

# OCEL
# PRO BUDOUCNOST

TRZ.CZ

Odborný on-line časopis pro metalurgii a příbuzné obory

# Hutnické listy

Metallurgical Journal

**Ročník / Volume: LXXIX**
**Rok / Year: 2026**
**Číslo / No.: Speciální vydání / Special Edition**

**www.hutnickelisty.cz**
**ISSN: 3029-8350**

**Vydavatel / Publisher**

Česká hutnická společnost, z.s.
Průmyslová 1034
739 61 Třinec – Staré Město
IČ: 00538671
e-mail: redakce@hutnickelisty.cz

# Foreword

*Dear Colleagues,*

*You are holding a special issue of Hutnické listy dedicated to the 11th International Conference "Modelling and Simulation of Metallurgical Processes in Steelmaking – STEELSIM 2025," which took place at TRISIA in Třinec from September 2 to 4, 2025. The conference was organized by the Czech Metallurgical Society under the auspices of Třinecké železárny, a.s., acting as the general partner.*

*The aim of the conference was to facilitate the exchange of current experience and knowledge in a highly attractive field of modern science that employs modelling and simulation to predict the behavior of various natural and techno-economic phenomena, in this case within the domain of steel production and processing. Modelling and simulation have steadily penetrated all areas of our lives; they are widely applied in industrial practice, form an integral part of education at most universities, and the knowledge gained is subsequently utilized across numerous industrial companies.*

*It is my pleasure to note that, within Třinecké železárny, physical modelling methods using scaled models of industrial equipment have been employed for more than 35 years. With the development of high-performance computing, these approaches have later been complemented by numerical modelling methods utilizing professional software tools such as Ansys Fluent, MAGMASOFT, and ProCAST. Among the first major tasks addressed using physical modelling methods was the study of melt flow in tundishes of both continuous casting machines operated at Třinecké železárny, with the aim of optimizing their internal arrangement. This subsequently led to a significant reduction in casting defects and an improvement in steel quality.*

*Over time, these activities expanded to include the modelling of mixing zones in continuously cast products, the development of new impact zones in tundishes, the modelling of steel behaviour in moulds including the design of innovative submerged entry nozzles, as well as a number of other important technical tasks.*

*At present, physical modelling in the model laboratory of Třinecké železárny focuses on the behaviour of the melt and slag in ladles during secondary metallurgy, particularly under inert gas stirring, with the aim of optimizing the placement of porous plugs in the ladle bottom.*

*In this context, the exchange of experience, knowledge, and scientific insights among professionals engaged in this field is of great importance, which was the primary objective of the STEELSIM 2025 conference. An equally important secondary outcome was the establishment of new professional contacts and personal connections during the accompanying social events. In my opinion, as well as in the view of other participants, the conference fully achieved its intended goals and will undoubtedly contribute to further innovations in the challenging environment of modern metallurgical production. A selection of the most interesting contributions presented at the conference can be found in this special issue of Hutnické listy.*

*In conclusion, I would like to express my sincere thanks to the conference organizers for their excellent and flawless preparation of the event, to the management of Třinecké železárny, as the general partner, for their support, and to all participants for their inspiring and innovative contributions in the field of metallurgical process modelling. The next STEELSIM conference will be held in Düsseldorf in June 2027.*

***Prof. Ing. Karel Michalek, CSc.***

# Předmluva

*Vážení kolegové,*

*do rukou se vám dostává speciální číslo Hutnických listů, věnované 11. mezinárodní konferenci „Modelování a simulace metalurgických procesů v ocelářství – STEELSIM2025“, která proběhla v třinecké TRISII ve dnech 2. - 4. 9. 2025 za organizačního zajištění České hutnické společnosti, z.s. a pod záštitou Třineckých železáren, a.s. jako generálního partnera.*

*Konference měla za cíl výměnu současných zkušeností a poznatků z velmi atraktivní oblasti současné vědy, která používá modelování a simulace k predikci chování mnohých přírodních a technicko-ekonomických jevů, v tomto případě z oblasti výroby a zpracování oceli. Modelování a simulace neodbytně proniklo do všech sfér našeho života, je široce používáno v praxi, je nedílnou součástí vzdělávání na většině univerzitních pracovišť, nabyté poznatky jsou pak využívány v řadě průmyslových společností.*

*S potěšením mohu konstatovat, že v podmínkách Třineckých železáren jsou metody fyzikálního modelování na zmenšených modelech provozních zařízení využívány již více než 35 let. Později, s rozvojem velmi výkonné výpočetní techniky, k tomu přibyly i metody numerického modelování využívající profesionální softwarové produkty jako např. AnsysFluent, Magmasoft, Procast. Mezi prvními zásadními úkoly, řešenými pomocí metod fyzikálního modelování, byl výzkum proudění lázně v mezipánvích obou zařízení plynulého odlévání provozovaných v TŽ, a.s., s cílem optimalizovat vnitřní uspořádání mezipánve, které následně vedlo k razantnímu snížení poruchových stavů během odlévání a zvýšení jakosti odlévané oceli. Postupně časem k těmto úkolům přibylo modelování směsných oblastí v plynule litých předlitcích, vývoj nových dopadových míst v mezipánvi, modelování chování oceli v krystalizátorech s návrhem inovativních ponorných výlevek a celá řada dalších neméně důležitých technických úkolů.*

*V současné době probíhá v modelové laboratoři Třineckých železáren fyzikální modelování chování lázně a strusky v licích pánvích během sekundárního zpracování prodmýcháváním inertním plynem s cílem optimalizovat umístění dmyšných elementů ve dně licí pánve.*

*V tomto kontextu je proto velmi důležitá výměna zkušeností, poznatků a vědeckých zdůvodnění s pracovníky, kteří se této problematice profesionálně věnují, což bylo tím primárním cílem proběhlé konference STEELSIM2025. Neméně důležitým sekundárním efektem konference bylo pak navázání nových kontaktů a vytvoření osobních vazeb na neformálních setkáních v doprovodných akcích konference. Dle mého názoru, ale i názoru ostatních účastníků, konference beze zbytku splnila svůj plánovaný cíl a zcela určitě povede i k dalším inovacím v nelehkém prostředí současné metalurgické výroby. Některé nejzajímavější práce prezentované na této konferenci najdete v tomto speciálním čísle Hutnických listů.*

*Na závěr bych si dovolil poděkovat organizátorům konference za vzornou a bezchybnou přípravu celé akce, vedení Třineckých železáren, jako generálnímu partneru, za podporu této akce a rovněž pak i účastníkům konference za podnětné a inovativní poznatky z oblasti modelování metalurgických procesů. Následná konference STEELSIM se bude konat v Düsseldorfu v červnu 2027.*

***Prof. Ing. Karel Michalek, CSc.***

# Editorial

*Dear Readers of Hutnické listy,*

*On behalf of the Czech Metallurgical Society, we are pleased to present this special issue highlighting the importance of the STEELSIM conference as a key professional forum for sharing the latest advances in the modelling and simulation of metallurgical processes.*

*The STEELSIM 2025 conference, held in the industrial heart of the Czech Republic – Třinec, brought together leading researchers, engineers, and industry professionals from both academia and practice. It was a truly international event, with 122 participants from 18 countries (Austria, Canada, the Czech Republic, Finland, France, Germany, China, India, Italy, Japan, the Netherlands, Poland, the Republic of Korea, Saudi Arabia, Slovakia, Sweden, the United Kingdom, and the United States). In total, 49 oral presentations and 13 posters were delivered, contributing significantly to the high scientific and professional level of the conference.*

*The diversity of perspectives provided a comprehensive insight into the current state of modelling and simulation in metallurgical processes, fostering not only the exchange of knowledge but also the establishment of new professional collaborations.*

*The papers included in this issue represent a selected collection of contributions presented at the conference and reflect both current trends and future directions in the field. We believe this issue will serve as a valuable resource for the professional community and inspire further research as well as closer cooperation between academia and industry.*

*This issue also includes a foreword by Prof. Ing. Karel Michalek, CSc., a mentor and pioneer in the field of metallurgical process modelling in the Czech Republic. We would like to express our sincere gratitude for his invaluable contribution to laying the foundations of this conference and to the development of simulation methods in metallurgy.*

*We would also like to thank all authors and conference participants for their active contribution to the high professional standard of both the conference and this special issue.*

***Czech Metallurgical Society***
*Organizer of the STEELSIM 2025 conference and publisher of Hutnické listy – Metallurgical Journal*

# Úvodník

*Vážení čtenáři Hutnických listů,*

*jménem České hutnické společnosti chceme tímto speciálním číslem podtrhnout význam konference STEELSIM jako důležité odborné akce sloužící ke sdílení nejnovějších poznatků v oblasti modelování a simulace metalurgických procesů.*

*Konference STEELSIM 2025, která se konala v průmyslovém srdci České republiky – v Třinci, přilákala přední výzkumné pracovníky, inženýry i vedoucí pracovníky z akademické sféry a průmyslu. Šlo o skutečně mezinárodní setkání, kterého se zúčastnilo 122 odborníků z celkem 18 zemí (Rakousko, Kanada, Česká republika, Finsko, Francie, Německo, Čína, Indie, Itálie, Japonsko, Nizozemsko, Polsko, Korejská republika, Saúdská Arábie, Slovensko, Švédsko, Spojené království a Spojené státy). Tito účastníci přispěli 49 ústními prezentacemi a 13 postery, čímž významně podpořili odbornou úroveň konference.*

*Jedinečné propojení různých pohledů umožnilo komplexní nahlédnutí na současný stav modelování a simulace metalurgických procesů a podpořilo nejen sdílení znalostí, ale také navazování nových profesních vztahů.*

*Příspěvky předložené v této publikaci představují reprezentativní výběr prací prezentovaných na konferenci a odrážejí aktuální trendy i budoucí směřování oboru. Věříme, že toto číslo bude cenným zdrojem informací pro odbornou komunitu a zároveň inspirací pro další výzkum a rozvoj spolupráce mezi akademickou sférou a průmyslem.*

*Součástí tohoto čísla je předmluva pana prof. Ing. Karla Michalka, CSc., mentora a průkopníka modelování metalurgických procesů v České republice, kterému chceme touto cestou znovu poděkovat za neocenitelný přínos k položení základů této konference a rozvoji simulačních metod v oboru hutnictví.*

*Rádi bychom tímto zároveň poděkovali všem autorům i účastníkům konference za jejich aktivní přínos k vysoké odborné úrovni této akce i tohoto speciálního čísla.*

***Česká hutnická společnost, z.s.***
*Organizátor konference STEELSIM 2025 a vydavatel Hutnických listů*

# Content / Obsah



## Selected Conference Articles / Vybrané články z konference

Hutnické listy – *Metallurgical Journal*
Speciální vydání / Special Issue, roč. / vol. LXXIX
ISSN Online: 3029-8350

# Integrated CFD Models for Optimizing Scrap Melting in DC EAF

# Integrované CFD modely pro optimalizaci tavení šrotu ve stejnosměrné EOP

**Shiyu Wang[1], Orlando Ugarte[1], Tyamo Okosun[1], Sunday Abraham[2], Yufeng Wang[2], Randy Petty[2], Chenn Q.Zhou[1]**

[1] Center for Innovation through Visualization and Simulation (CIVS) and Steel Manufacturing Simulation and Visualization Consortium (SMSVC), Purdue University Northwest; Hammond, IN, U.S.A. *Correspondence: ougarte@pnw.edu; Tel.: 1-219-989-2089

[2] SSAB Americas, Muscatine, IA, U.S.A.

## Abstract

*In the U.S., ~70% of steel is produced in electric arc furnaces (EAFs), and significant investment is devoted to increase EAF production capacity. EAFs integrate chemical and electrical energy to melt scrap, precipitating phase changes and reactions that need to be controlled to achieve the desired molten steel. The multi-phenomena nature of EAF operations presents challenges for optimization. This study applies an advanced CFD methodology to simulate the operation of an industrial DC-EAF to study the impact of electrical arc power on melting. Namely, a CFD tool integrating a coherent-jet model, a DC arc heating model and a scrap melting model is applied to a DC-EAF heat provided by SSAB. After validating CFD predictions against actual data, simulations of scenarios with modified arc power (10% and 20% reduction from baseline) are performed. All other conditions such as burner power and charge recipe remain the same. Results indicate that each 10% power reduction extends the melting time for 60 tonnes of scrap by two minutes. Also, a boost in melting performance is observed when the average molten bath temperature rises above the liquidus temperature. Non-uniformity of arc heating is also described and potential optimization of EAF melting is discussed.*

***Keywords:*** *electric arc furnace, DC, arc heating, CFD, scrap layering, melting*

## Abstrakt

*V USA se přibližně 70% oceli vyrábí v elektrických obloukových pecích (EOP) a významné investice směřují do zvyšování jejich výrobní kapacity. Elektrické obloukové pece kombinují chemickou a elektrickou energii k tavení šrotu, přičemž dochází k fázovým přeměnám a reakcím, které je nutné řídit pro dosažení požadovaného stavu roztavené oceli. Více-jevová povaha provozu EOP představuje významnou výzvu z hlediska optimalizace. Tato studie využívá pokročilou metodiku CFD k simulaci provozu průmyslové stejnosměrné elektrické obloukové pece (DC-EAF) za účelem posouzení vlivu výkonu elektrického oblouku na proces tavení. Konkrétně je aplikován CFD nástroj integrující model koherentního proudu, model ohřevu stejnosměrným obloukem a model tavení šrotu na případ průmyslové DC-EAF dodané společností SSAB. Po validaci výsledků CFD simulací na základě reálných provozních dat byly provedeny simulace scénářů se sníženým výkonem oblouku (o 10% a 20% oproti referenčnímu stavu), přičemž ostatní parametry, jako výkon hořáků a složení vsázky, zůstaly nezměněny. Výsledky ukazují, že každé snížení výkonu o 10% prodlužuje dobu tavení 60 tun šrotu přibližně o dvě minuty. Dále bylo zjištěno zlepšení tavicího procesu při překročení teploty likvidu průměrnou teplotou roztavené lázně. Práce rovněž popisuje nerovnoměrnost ohřevu obloukem a diskutuje možnosti optimalizace procesu tavení v EOP.*

***Klíčová slova:*** *elektrická oblouková pec, stejnosměrný proud, obloukový ohřev, CFD, vrstvení šrotu, tavení*

Hutnické listy – *Metallurgical Journal*
Speciální vydání / Special Issue, roč. / vol. LXXIX
ISSN Online: 3029-8350

## 1. Introduction

Electric arc furnaces (EAFs) play a critical role in modern steelmaking, contributing a significant fraction of production capacity in North America. In particular, DC EAFs present some key advantages in energy efficiency, power input flexibility, and consistent spatial melting due to the central location of the arc, among others [1]. The melting process in EAFs is influenced by various factors, with electrical power input being a key determinant of melting performance. Understanding and accurately predicting melting behavior under different electrode power conditions is essential for optimizing operational efficiency and minimizing energy consumption.

CFD modelling offers key advantages for analysing and optimizing complex EAF processes. It provides detailed, spatially resolved insights into process behavior which can be difficult to measure directly and enables analysis of parameters like electrode power in isolation, without trial-and-error testing. Once validated, CFD can also be used to optimize operations, improving EAF efficiency and reliability.

Many researchers have utilized simulation methods of various techniques (including CFD) to investigate components of the EAF process. Kazak et al. conducted numerical modelling to investigate the electromagnetic, temperature, and hydrodynamic distributions in a DC EAF. It was found that raising the bottom electrode to the electrode radius above the fettle surface reduced shear stress by 30%, while lowering it by the same distance below the surface reduced stress by 10% [2].

Fathi et al. developed a computational model and algorithm to estimate the arc energy distribution in an EAF, accounting for conductive, convective, and radiative heat transfer. The proposed algorithm uses a channel arc model (CAM) to reduce computational load, requiring only arc length and arc current as inputs. Results show high similarity with experimental data, validating the model effectiveness while maintaining low computational complexity [3].

Samet et al. developed and compared three computational approaches to calculate optimal set-points for series reactors and transformer taps in a DC EAF. Results highlight that improving the transferred power by adjusting transformer taps and reactor configurations can significantly enhance EAF productivity [4]. Martell-Chávez et al. introduced the concept of “useful arc power” and used a thermal model to theoretically estimate the peak arc power in AC-EAFs. The influence of arc length and stability on energy efficiency was analysed. Industrial-scale EAF tests confirmed that optimizing current setpoints can improve energy efficiency [5]. Bhonsle et al. developed a novel time domain EAF model to investigate power quality issues in electric arc furnaces, focusing on non-linear loads that introduce voltage flicker and harmonic distortion in distribution networks.

Simulations conducted in the SIMULINK/MATLAB environment confirmed the model effectiveness in analysing and addressing power quality problems in EAF operation [6]. Logar et al. performed a statistical analysis of over 2500 heats of EAF data, focusing on how input feeds and the carbon-to-oxygen ratio affect electrical energy consumption (EEC). The study found that besides scrap weight and tapping temperature, fluctuations in the added carbon and oxygen also significantly impact EEC. These insights can help identify operational improvements to reduce energy consumption [7].

The subject of this study is to simulate and validate a real-world DC EAF operation based on a furnace operated by SSAB Americas and to use the integrated model for prediction. This study focuses on the impact of electrode power input on melting performance.

Hutnické listy – *Metallurgical Journal*
Speciální vydání / Special Issue, roč. / vol. LXXIX
ISSN Online: 3029-8350

Three cases with different electrode power conditions were developed: the baseline case and two cases with electrical power input reduced to 90% and 80% of the baseline, respectively. The operation time considered in this study starts from the moment the electrode begins operation, covering the bore-in stage and extending 20 minutes beyond this stage.

## 2. Methodology

The focus of this paper is on the impact of electrode power on melting performance. **Fig. 1** provides a schematic overview of the comprehensive CFD DC scrap melting model developed by researchers at Purdue University Northwest for the Steel Manufacturing Simulation and Visualization Consortium (SMSVC). This comprehensive CFD EAF scrap melting simulator is used to simulate the melting process in a real DC EAF operation provided by SSAB. The simulator consists of three sub-models: the scrap melting model, the coherent jet model, and the electric arc model.

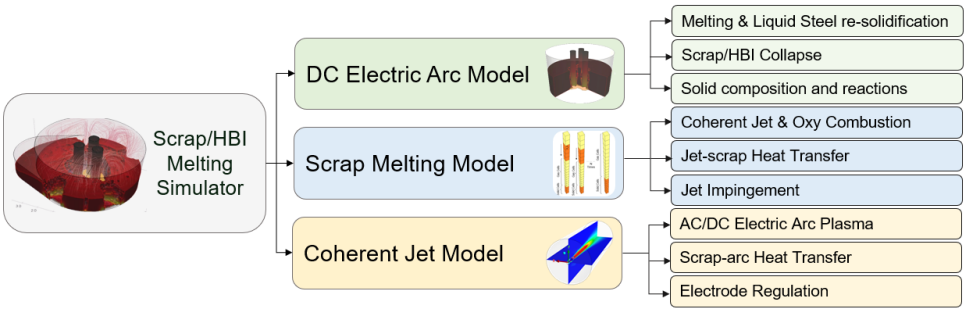


**Fig. 1** Schematic overview of the comprehensive CFD DC Scrap Melting Model

**Obr. 1** Schematický přehled komplexního CFD modelu DC Scrap Melting Model

Details of these models are presented in previous publications [9], while the functionality is summarized here. The DC electric arc model uses constant impedance control to maintain arc voltage and current, with arc impingement modelled as additional liquid bath momentum. Arc heating distribution is determined using lab-scale 2D simulations and a database of DC parameters [3], integrated into the scrap melting model to capture heating effects in industrial EAF scenarios. Additionally, the coherent jet model [8] accounts for combustion reactions and heat exchange between gas and solid phases, using species conservation equations and heat transfer coefficients. Heat transfer is determined by temperature-dependent expressions.

The scrap melting model uses a two-phase (liquid and gas) Eulerian-Eulerian approach for modelling fluids and incorporates solid-liquid mass transfer, inter-phase forces, and arc-induced momentum. Solid scrap melting and collapse is modelled using a dual-cell approach. Melting and re-solidification are captured via latent heat and effective specific heat capacity, with complete details can be found in previous publications [9] [10]. **Fig. 2** demonstrates the flowchart specific to this study for investigating the effect of electric arc power on melting performance. After preprocessing the operational data provided by SSAB, the arc profile, scrap layering condition, and burner profile needed for the simulation are provided as inputs to the electric arc model, scrap melting model, and coherent jet model, respectively. The outputs of the simulation model, such as melting rate, temperature, and electrode motion, can be used for validation by comparing results with real-world data. Once the model is validated, scenario cases with different electrode power profiles are established to study the impact of electrode power.

Hutnické listy – *Metallurgical Journal*
Speciální vydání / Special Issue, roč. / vol. LXXIX
ISSN Online: 3029-8350

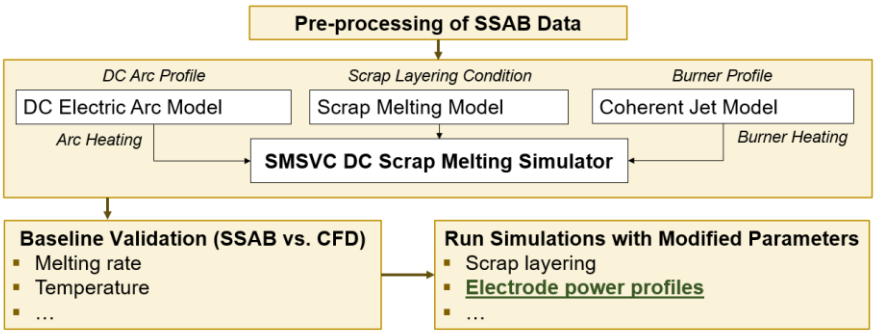


**Fig. 2** Flowchart for the Effect of Electrode Power on Melting Performance

**Obr. 2** Schéma vlivu výkonu elektrody na vlastnosti tavení

## 3. Simulation Parameters

**Fig. 3** illustrates the timeline of an SSAB tap-to-tap process. The first 40 minutes employ a hold-fire mode for the burners with no electrode power. In this stage, two scrap buckets are charged while the shell awaits the next opportunity for the electrode and melting. The following 37 minutes comprise the melting and refining stage, when both the electrode and burners are on. The entire process lasts 87 minutes.

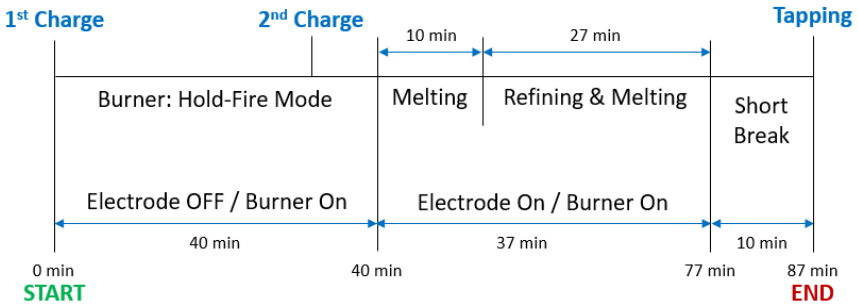


**Fig. 3** SSAB DC EAF Tap-to-Tap Process Timeline

**Obr. 3** Časová „tap-to-tap“ osa v elektrické obloukové peci SSAB DC

**Tab. 1** and **Fig. 4** separately present the scrap layering condition and the burner profile. The scrap density varies across different locations in the furnace. In the simulation, this variation is captured by incorporating the bulk density and weight of each material according to the actual SSAB recipe. There are eight layers of scrap in the first bucket and one layer in the second bucket. Regarding the burner profile, all burners operate in combustion mode before 3000 seconds. After this, the oxygen injection rates for burners 1 and 3 increase significantly, initiating the lancing mode, while burners 4 and 5 continue operating in combustion mode. The figure on the right side of **Fig. 4** shows the locations of these four burners, with burner 2 turned off during this heat.

**Tab. 1** Scrap Layering Conditions / **Tab. 1** Podmínky pro vrstvení šrotu

| | **Commodity** | **Weight [kgs]** |
|---|---|---|
| 1st Bucket | PROCREVERT/2HM/HM1/CAST FE/PIT SCRAP/#1.5 DE BUNDLES/MXTN/FRAG | 108,636.4 |
| 2nd Bucket | FARG | 53,090.9 |

Hutnické listy – *Metallurgical Journal*
Speciální vydání / Special Issue, roč. / vol. LXXIX
ISSN Online: 3029-8350

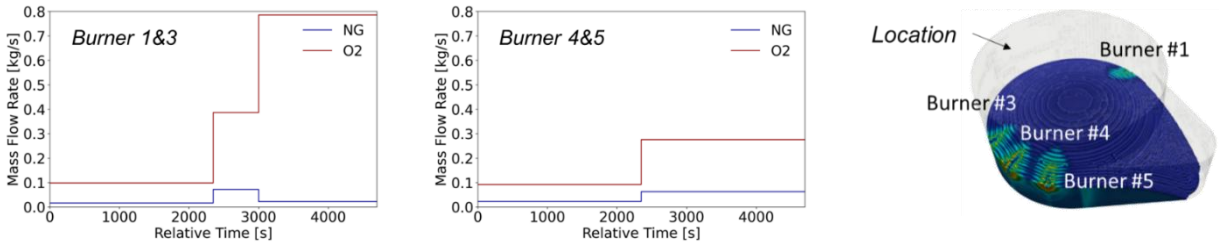


**Fig. 4** Burner Profiles / **Obr. 4** Profily hořáků

**Fig. 5** shows the different input profiles for the three study cases, which vary in arc power, arc length, and current. In this study, the arc power is adjusted by changing the arc current, which consequently causes changes in both arc length and current. The arc power levels in the three cases are set at 100% (baseline case, based on SSAB actual power profile), 90%, and 80%, respectively.

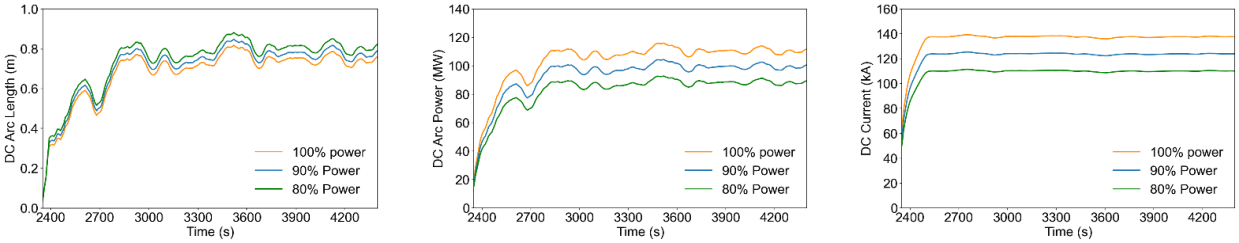


**Fig. 5** Different Input Profile for Three Parametric Study Cases (80%, 90% & 100%)

**Obr. 5** Různé vstupní profily pro tři parametrické případové studie (80%, 90% a 100%)

**Tab. 2** shows the detailed setup for these three cases with different inputs. The only differences among the three cases are the inputs shown in **Fig. 5**. Besides this, all three cases have the same number of burners, burner power input, and initial recipe.

**Tab. 2** CFD Cases Setup: Different Power Condition / **Tab. 2** Nastavení CFD modelů: Různé podmínky napájení

| Case | Power | Total Electrode Power Input | Burner | Total Burner Input | Recipe |
|---|---|---|---|---|---|
| 1 | 100% Power | 65412 kwh | 4 Burners | ~6.42 kwh | 2 Buckets 7 Layers |
| 2 | 90% Power | 58871 kwh | | | |
| 3 | 80% Power | 52329 kwh | | | |

## 4. Validation

Results shown in this section are up to 4500 seconds, representing approximately 96% of the actual SSAB operation. The method for validation is to compare the melting rate predicted by the CFD simulation with the one expected in actual SSAB operation. Also, the average melting temperature is compared with data collected near tapping.

**Fig. 6** shows the solid mass and liquid mass over time from the CFD results, while **Tab. 3** presents the differences between the SSAB data and simulation results. The average melting rate for the first 2170 seconds of melting in this case is 59 kg/s. For SSAB's industrial operation, assuming all scrap is melted at the end of the heat, the average melting rate is 68 kg/s.

Hutnické listy – *Metallurgical Journal*
Speciální vydání / Special Issue, roč. / vol. LXXIX
ISSN Online: 3029-8350

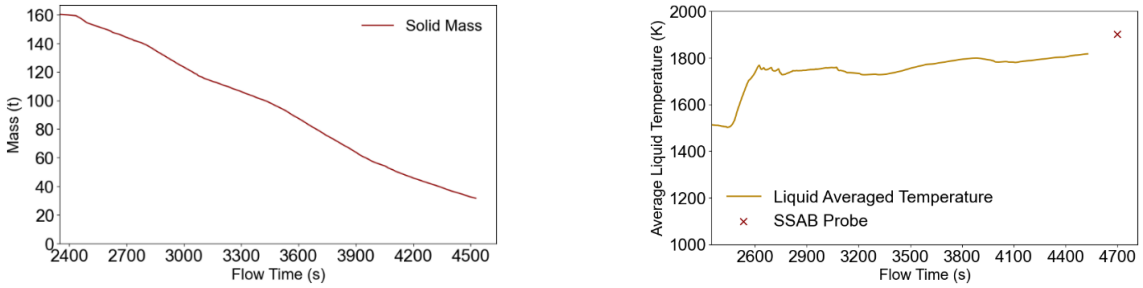


**Fig. 6** Simulation Results: Liquid Mass, Solid Mass & Average Liquid Temperature

**Obr. 6** Výsledky simulace: podíl kapalné fáze, podíl pevné fáze a průměrná teplota kapalné fáze

Therefore, the difference at this stage is approximately 13.2%. It should be noted that the current case does not include the effect of arc shrouding by foamy slag, which is to be considered in future simulations. This effect is anticipated to reduce energy losses and increase the simulated average melting rate. **Fig. 6** also shows the average liquid temperature over time. The temperature increases rapidly during the first 400 seconds, then stabilizes. In SSAB heat the liquid temperature reached 1902 K near the end of the operation. Therefore, the current difference between average liquid temperature in CFD simulation and the one provided by SSAB probe is 4.5%.

**Tab. 3** Difference between SSAB Data and Simulation Results / **Tab. 3** Rozdíl mezi daty SSAB a výsledky simulace

| | SSAB | CFD | Difference |
|---|---|---|---|
| Melting Rate (kg/s) | 68 | 59 | 13.2% |
| Molten Steel Temperature (k) | 1902 | 1816 | 4.5% |

## 5. Results

**Fig. 7** illustrates the simulation results of the bore-in stage and melting stage. In this study, it is assumed that only vertical collapse occurs during melting. The bore-in stage ends at 2510 seconds and lasts for 160 seconds, with re-solidification observed beneath the electrode tip. Following the bore-in stage is the main melting stage, where the melting pattern goes from the inside to the outside and from bottom to top.

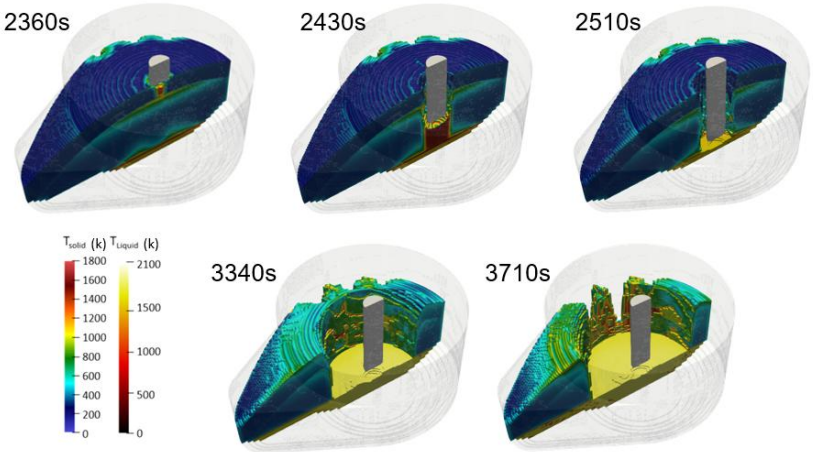


**Fig. 7** Simulation Results: Bore-in Stage & Melting Stage

**Obr. 7** Výsledky simulace: Počáteční a hlavní fáze tavení

Hutnické listy – *Metallurgical Journal*
Speciální vydání / Special Issue, roč. / vol. LXXIX
ISSN Online: 3029-8350

**Fig. 8** shows the simulation results for the three cases with different electrode power inputs. The bore-in rate for the baseline case (100% power) is the fastest (see left **Fig. 8**), as expected. Regarding energy transfer, the total energy transferred from the electrode to the solid scrap and molten steel is plotted (center). The peak of the total energy input for the baseline case can reach 120MW. However, the energy received by the scrap is less than 120MW due to common energy losses during operation. In the plot showing the energy transferred to the solid only (right side), it can be observed that the energy transferred to the solid decreases after the bore-in stage is completed. This is because the electrode tip begins to heat the molten steel bath, causing more energy to be transferred to the liquid phase instead.

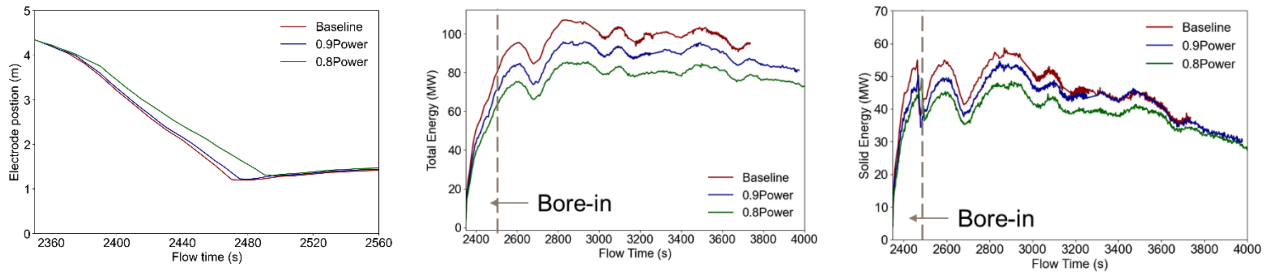


**Fig. 8** Simulation Results: Electrode Position & Energy Transfer Distribution

**Obr. 8** Výsledky simulace: Poloha elektrod a rozložení přenosu energie

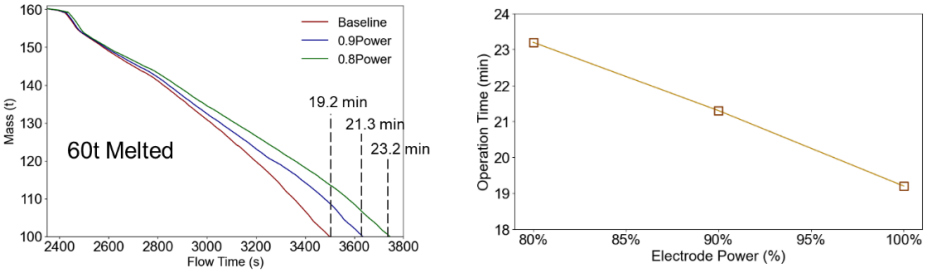


**Fig.9** Time Needed to Melt 60 tonnes of Scrap

**Obr. 9** Doba potřebná k roztavení 60 tun šrotu

Since different energy inputs lead to varying energy transfer distributions, the melting performance of these three cases with different electrode power inputs will also differ. **Fig. 9** illustrates the change in solid mass after the electrode power is turned on. The red line represents the case with the highest electrode power input, showing the fastest solid melting rate. Comparing the time needed to melt the same amount of solid scrap (60 tonnes), it is observed that it takes 19.2 minutes to melt 60 tonnes of scrap when the electrode power input is 100%. When the power is decreased to 90%, the melting time is increased to 21.3 minutes, a difference of 2.1 minutes, as shown in **Tab. 4**. The plot on the right in **Fig. 9** shows the near-linear relationship between operation time and electrode power.

**Tab. 4** Time and Electrode Power Input Needed to Melt 60 tonnes of Scrap
**Tab. 4** Čas a příkon elektrod potřebný k roztavení 60 tun šrotu

| Case | Time Needed to Melt 60 t | Difference | Electrode Energy Input |
|---|---|---|---|
| 100% Power | 19.2 min | | 31,486 kWh |
| 90% Power | 21.3 min | 2.1 min | 31,341 kWh |
| 80% Power | 23.2 min | 4.0 min | 31,010 kWh |

Hutnické listy – *Metallurgical Journal*
Speciální vydání / Special Issue, roč. / vol. LXXIX
ISSN Online: 3029-8350

**Tab. 4** focuses on the melting time, while **Tab. 5** presents the average melting rate for the first 20 minutes of melting. This set of data does not show a linear trend. When the electrode power is reduced from 100 % to 90%, the average melting rate decreases by approximately 14%. However, the difference drops to 23% when the power is decreased from 100% to 80%.

**Tab. 5** Average Melting Rate for the First 20 Minutes / **Tab. 5** Průměrná rychlost tavení během prvních 20 minut

| Case | Melting Rate for First 20 Minutes | Difference (%) |
|---|---|---|
| 100% Power | 53.9 kg/s | |
| 90% Power | 46.4 kg/s | 14 % |
| 80% Power | 41.3 kg/s | 23 % |

To explain the non-linear relationship observed here between electrode power input and the average melting rate for the first 20 minutes, **Fig. 10** presents the instantaneous melting rate for the three cases. Overall, during the bore-in stage, the melting rate increases and then remains relatively constant, with minimal differences between the three cases at this point. Subsequently, each case exhibits a distinct increase at different times.

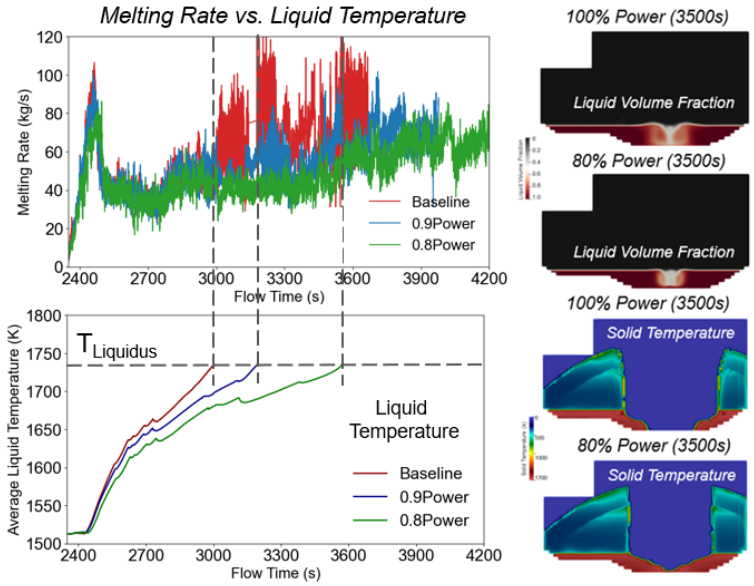


**Fig. 10** The Impact of Liquid Temperature on Melting Performance

**Obr. 10** Vliv teploty kapalné fáze na vlastnosti tavení

The red line, representing the highest power input, consistently shows the fastest melting rate. However, a noticeable increase in the melting rate only occurs after approximately 3000 seconds. In comparison, for the 80% power case (green line), this increase begins around 3600 seconds. The plot below also indicate that the average molten steel temperature influences the melting rate. The dashed line represents the liquidus temperature, approximately 1734 K. It can be seen from these two plots that once the average molten steel temperature of the entire bath exceeds the liquidus point, the melting rate begins to increase significantly, driven by convection from the liquid steel to the melting solid material in addition to the radiation heat transfer provided directly from the arc. This convection can transport heat to a broader portion of the solid scrap at the bottom of the furnace compared to radiation alone. This trend is observed consistently across all three cases.

Hutnické listy – *Metallurgical Journal*
Speciální vydání / Special Issue, roč. / vol. LXXIX
ISSN Online: 3029-8350

With a higher electrode energy input, the liquid temperature rises more quickly, enabling the liquid phase to begin contributing to the melting process earlier in the 100% power case. This leads to a faster overall melting rate within the first 20 minutes. This is further confirmed by the two contours that show the liquid volume at the same moment. In the 100% power case, more molten steel is present, increasing the contact area of liquid steel with solid scrap and allowing the liquid phase to support the melting process more effectively.

Additionally, the liquid temperature plot demonstrates that the 80% power case requires a longer time to reach the liquidus temperature. This delay can be attributed to non-uniform heating, which makes it more challenging to heat distant regions when the energy input is lower.

The two contours also illustrate the liquid volume at the same time point, highlighting the much stronger heating effect in the baseline case, which helps to extend the temperature rise further into the distant region. Finally, the two contours below show the corresponding solid temperature distribution. From the melting pattern, the molten steel in this case is already assisting the melting process, as indicated by the clear vertical collapse.

## 6. Conclusions

This study focused on the simulation and validation of a SSAB DC-EAF heat. A discrepancy of approximately 13.2% in the melting rate and 4.5% in the liquid temperature was observed between CFD and actual data. The accuracy of the CFD simulation during the refining stage can be improved through the consideration of slag effects.

Furthermore, electrode power input was identified as a major determinant of melting performance. Variations in DC power input result in different arc current and arc length values, directly influencing the melting rate. It was found that each 10% reduction in arc energy increased the melting time by approximately two minutes.

Additionally, a peak in the melting rate was observed during the bore-in stage, and a significant boost in the melting rate was triggered once the average molten bath temperature exceeds the liquidus point.

### References

[1] ODENTHAL, H.-J., KEMKMINGER, A., KRAUSE, F., SANKOWSKI, L., UEBBER, N. and VOGL, N., 2018. Review on modelling and simulation of the electric arc furnace (EAF). *Steel Research International*, 89(1).

[2] KAZAK, O., 2013. Modelling of vortex flows in direct current (DC) electric arc furnace with different bottom electrode positions. *Metallurgical and Materials Transactions B*, 44, pp.1243-1250.

[3] FATHI, A., SABOOHI, Y., ŠKRJANC, I. and LOGAR, V., 2015. Low computational-complexity model of EAF arc-heat distribution. ISIJ International, 55(7), pp.1353–1360.

[4] SAMET, H., GHANBARI, T. and GHAISARI, J., 2014. Maximizing the transferred power to electric arc furnace for having maximum production. *Energy*, 72, pp.752–759.

[5] MARTELL-CHÁVEZ, F., RAMÍREZ-ARGÁEZ, M., LLAMAS-TERRES, A. and MICHELOUD-VERNACKT, O., 2013. Theoretical estimation of peak arc power to increase energy efficiency in electric arc furnaces. *ISIJ International*, 53(5), pp.743–750.

[6] BHONSLE, D.C. and KELKAR, R.B., 2016. Analyzing power quality issues in electric arc furnace by modelling. *Energy*, 115, pp.830–839.

[7] LOGAR, V. and ŠKRJANC, I., 2021. The influence of electric-arc-furnace input feeds on its electrical energy consumption. Journal of Sustainable Metallurgy, 7, pp.1013–1026.

[8] CHEN, Y., LUO, Q., RYAN, S., BUSA, N., SILAEN, A.K. and ZHOU, C.Q., 2022. Effect of coherent jet burner on scrap melting in electric arc furnace. *Applied Thermal Engineering*, 212, 118596.

[9] WANG, S., UGARTE, O., RYAN, S., OKOSUN, T. and ZHOU, C.Q., 2024. Computational fluid dynamics simulation of industrial electric arc furnace operation: validation and performance of melting phenomena. *Steel Research International*, p.2400509.

[10] CHEN, Y., RYAN, S., SILAEN, A.K. and ZHOU, C.Q., 2022. Numerical investigation of AC electric arc plasma heat dissipation in EAF. *Ironmaking & Steelmaking*, 49(3), pp.255–267.

Hutnické listy – *Metallurgical Journal*
Speciální vydání / Special Issue, roč. / vol. LXXIX
ISSN Online: 3029-8350

# CFD-DEM Simulation of the Scrap Hot Metal Interaction in Steelmaking Furnace

# Numerická CFD-DEM simulace: Interakce mezi šrotem a roztaveným kovem v konvertoru

**Mohammed B. A. Hassan[1], Florian Charruault[2], Bapin Kumar Rout[2], Frank N. H. Schrama[1,2], Neslihan Dogan[1], Johannes A. M. Kuipers[3], Yongxiang Yang[1]**

[1] Department of Materials Science and Engineering, Delft University of Technology, Delft 2628 CD, The Netherlands *Corresponding author: m.b.a.hassan@tudelft.nl

[2] Tata Steel, IJmuiden 1970 CA, The Netherlands

[3] Chemical Engineering and Chemistry, Eindhoven University of Technology, Eindhoven 5612AZ, The Netherlands

## Abstract

*Increasing scrap usage in the Basic Oxygen Furnace (BOF) process is essential for improving sustainability and circularity in steel production. However, this approach poses challenges such as scrap distribution forming piles and refractory wear. To better understand the hydrodynamic interactions between hot metal and steel scrap during hot metal charging and rotation of the BOF, this study employs a coupled computational fluid dynamics – discrete element method (CFD-DEM) approach. The two-phase flow of hot metal and air is modelled using the Volume of Fluid (VOF) method, while the motion of individual scrap particles is simulated using the DEM. The current study simulates 100 tonnes of scrap charged from the scrap-box into an industrial-scale 330-tonne BOF furnace. It evaluates two scrap packing strategies (horizontal and vertical) by quantifying refractory wear using DEM. The results show that the horizontal packing strategy leads to a less worn area compared to its counterpart (the vertical strategy). The coupled CFD-DEM model is used to predict a potential iceberg formation near the converter wall during furnace rotation (before blowing) for a case of retarded melting. The CFD-DEM framework presented here provides a valuable tool for simulating and optimizing BOF operations, thereby increasing the efficiency of scrap usage in the modern steelmaking industry.*

***Keywords:*** *CFD-DEM, scrap, hot metal, BOF, steelmaking*

## Abstrakt

*Zvyšování podílu šrotu v procesu kyslíkového konvertoru (BOF) je klíčové pro zlepšení udržitelnosti a cirkularity výroby oceli. Tento přístup však přináší řadu výzev, jako je nerovnoměrná distribuce šrotu vedoucí k tvorbě shluků a zvýšenému opotřebení žáruvzdorné vyzdívky. Pro lepší pochopení hydrodynamických interakcí mezi tekutým surovým železem a ocelovým šrotem během vsázky surového železa a naklápění konvertoru využívá tato studie sdružený přístup výpočetní dynamiky tekutin a metody diskrétních prvků (CFD-DEM). Dvoufázové proudění surového železa a vzduchu je modelováno metodou Volume of Fluid (VOF), zatímco pohyb jednotlivých částic šrotu je simulován pomocí metody DEM. Studie simuluje vsázku 100 tun šrotu ze šrotového koryta do průmyslového kyslíkového konvertoru o kapacitě 330 tun. Jsou hodnoceny dvě strategie uspořádání šrotu (horizontální a vertikální) na základě kvantifikace opotřebení vyzdívky pomocí DEM. Výsledky ukazují, že horizontální uspořádání vede k menší míře opotřebení ve srovnání s vertikální variantou. Propojený model CFD-DEM je dále využit k predikci potenciální tvorby tzv. „iceberg" struktury v blízkosti stěny konvertoru během jeho naklápění (před dmýcháním) v případě pomalejšího tavení. Představený modelový rámec CFD-DEM prezentuje účinný nástroj pro simulaci a optimalizaci provozu BOF, a tím i pro zvýšení efektivity využití šrotu v moderním ocelářském průmyslu.*

***Klíčová slova:*** *CFD-DEM model, šrot, surové železo, kyslíkový konvertor (BOF), výroba oceli*

Hutnické listy – *Metallurgical Journal*
Speciální vydání / Special Issue, roč. / vol. LXXIX
ISSN Online: 3029-8350

## 1. Introduction

The Basic Oxygen Furnace (BOF) route accounts for approximately 70% of the global crude steel production. To reduce raw material consumption and enhance the circularity of the BOF process, scrap has become an essential input for operations. However, increasing scrap usage presents several challenges, such as refractory wear and iceberg formation (unmelted scrap in the hot metal).

Increasing scrap usage in BOF process under current industry conditions demands further detailed investigation of scrap melting efficiency and mechanisms. For this purpose, it is essential to understand the characteristics of solid-fluid phase interactions including mechanical (particle-particle and particle-fluid interactions), chemical (carbon dissolution and decarburization reactions), and thermal (heat transfer and phase change) phenomena - in order to maximize scrap usage without compromising metallurgical performance. Therefore, numerical simulations, more specifically VOF/CFD-DEM, are widely used to investigate fluid-solid interactions in such high-temperature systems [1], [2], [3]. In this study, we investigate the interaction of these phases from a hydrodynamic point of view.

## 2. Methods

### 2.1 Process Description

An industrial scale 330-tonne BOF is simulated using CFD-DEM. The process cycle begins with loading the scrap-box with various types and sizes of scrap. The scrap-box is tilted to discharge the scrap into the tilted BOF. The furnace is then rocked to promote a more uniform distribution of the scrap. This operation is important for preventing hazardous events associated with volatile materials, such as water, and for mitigating the risk of iceberg formation (apparent scrap above the hot metal interface).

Following scrap charging, the furnace is tilted again to allow hot metal charging. It is subsequently repositioned to a vertical orientation to initiate the refining stage, which combines top-blown oxygen injection with bottom stirring. Finally, the refined crude steel is tapped for downstream processing, and the converter is deslagged in preparation for the next process cycle.

### 2.2 Numerical Model

The BOF process operation involves principally 3 phases: solid steel scrap, liquid hot metal, and gas (for simplicity different gases e.g., oxygen, CO, $CO_2$ and slag formation are not included in the model). The two-phase flow of air and hot metal is modelled using the VOF approach. The advection equation is employed to track the interfaces of the volume fraction $\alpha_i$. For more details about the variables definitions in Equation 1, refer to [4]. The void fraction $\varepsilon$ is incorporated into the governing equations to account for the volume occupied by the discrete phase. The governing equations for the phase fraction $\alpha_i$, mass, and momentum are presented in Equations 1, 2, 3, respectively.

$$\frac{\partial \varepsilon \alpha_i}{\partial t} + \nabla \cdot \left(\varepsilon \alpha_i \boldsymbol{u_f}\right) - \nabla \cdot \left(\boldsymbol{u_c} \alpha_i (1 - \alpha_i)\right) = 0 \tag{1}$$

$$\frac{\partial \varepsilon}{\partial t} + \nabla \cdot \left(\varepsilon \boldsymbol{u_f}\right) = 0 \tag{2}$$

$$\frac{\partial \varepsilon \rho_f \boldsymbol{u_f}}{\partial t} + \nabla \cdot \left(\varepsilon \rho_f \boldsymbol{u_f} \boldsymbol{u_f}\right) = -\nabla p^* + \nabla \cdot \boldsymbol{\tau} - \varepsilon \boldsymbol{g} \cdot \boldsymbol{x} \nabla \rho_f + \varepsilon \boldsymbol{F}^{\sigma} + \boldsymbol{F}^{B} \tag{3}$$

Hutnické listy – *Metallurgical Journal*
Speciální vydání / Special Issue, roč. / vol. LXXIX
ISSN Online: 3029-8350

Here, $p^* \equiv p - \rho_f g \cdot x$ denotes the dynamic pressure (up to a constant), where g is the gravitational acceleration and x is the position vector. $F^\sigma$ represent the surface tension force between the two phases, modeled using the Continuum Surface Force (CSF) approach. $F^B$ denotes the fluid–particle interaction forces, calculated using Model B. This model assumes steady and uniform fluid flow through the solid phase. For more details, the reader is referred to [5] [6]. The drag force is computed using the Koch & Hill drag model [7].

For the solid scrap particles, the DEM, introduced by Cundall [8], is used to obtain particle trajectories by solving Newton–Euler Equation 4 and Equation 5 for translational and rotational motion, respectively.

$$m_i \frac{dv_i}{dt} = m_i \frac{d^2 x_i}{dt^2} = \vec{f}_i \left( \vec{x}_j, \vec{v}_j, \vec{\phi}_j, \vec{\omega}_j \right) \quad for\ j = 1 \dots N \tag{4}$$

$$I_i \frac{d\vec{\omega}_i}{dt} = I_i \frac{d^2 \vec{\phi}_i}{dt^2} = \vec{M}_i \left( \vec{x}_j, \vec{v}_j, \vec{\phi}_j, \vec{\omega}_j \right) \quad for\ j = 1 \dots N \tag{5}$$

The contact force $\vec{f}_i$ in Equation 4, is computed using the Hertz–Mindlin model. The force consists of both normal and tangential components. The normal component is calculated directly, while the tangential component is derived using a tangential history model until the Coulomb friction criterion is met ($f_t \leq \mu f_n$). In this study, the commercial software Aspherix (version 6.5.0) from DCS Computing [9] coupled with OpenFOAM-10 [10] using CFDEM-multiphase-6.5.0 framework was used to model the current system.

## 3. Simulation Results

There are different possible scrap arrangements and charging strategies. **Fig. 1** shows horizontally distributed scrap particles in the scrap-box with three different sizes (namely heavy, medium and light colored by red, gray and blue, respectively) being discharged. Heavy scrap particles are at the top and medium ones in the middle while light ones at the bottom. Another possible distribution strategy is vertically arranged scrap. In this work, we assumed similar density for all types of scrap particles. The influence of various scrap arrangements on the refractory wear is quantified using the Finne model [11].

**Fig. 1** Horizontally packed scrap of three types namely heavy, medium, and light (colored red, gray, and blue, respectively) being discharged from the scrap box into the converter

**Obr. 1** Typ šrotu – těžký, střední a lehký (označený červeně, šedě a modře) – se vykládá z šrotového koryta do konvertoru

Hutnické listy – *Metallurgical Journal*
Speciální vydání / Special Issue, roč. / vol. LXXIX
ISSN Online: 3029-8350

**Fig. 2** compares the wear distribution of Heavy-Light-Medium (HLM) scenarios for the two scrap arrangements (Horizontal (a) and Vertical (b)). The wear distribution in the vertically distributed case is greater than in the horizontally distributed case. This is attributed to the difference in kinetic energy between the two cases. It is found to be more uniform in the horizontal compared to the vertical case.

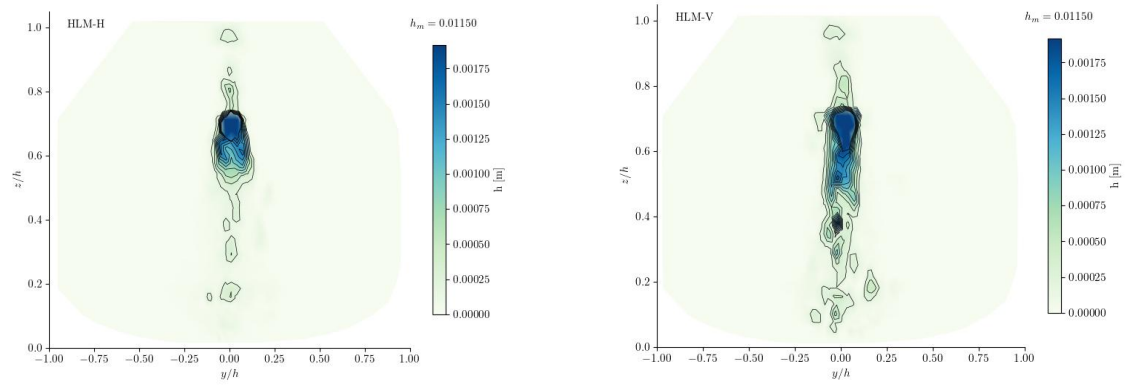


(a) (b)

**Fig. 2** Contour of refractory wear in the converter for different scrap arrangements: (a) horizontal and (b) vertical, using a total scrap weight of 100 tonnes

**Obr. 2** Průběh opotřebení vyzdívky konvertoru při různém rozložení šrotu: (a) horizontální a (b) vertikální, při celkové hmotnosti šrotu 100 tun

As highlighted in the process description, rocking is employed to achieve a more uniform distribution of scrap within the converter. The simple rocking operation is defined as tilting the converter from the scrap charging position (50° relative to the y-axis) to the vertical position and back to the scrap charging position again. **Fig. 3** illustrates the state of the scrap after a simple rocking operation, with the furnace tilted to the vertical position, along with the unoccupied furnace volume shown at the bottom right. Such a configuration is unwanted during operation due to the resulting inhomogeneous distribution of scrap relative to the hot metal.

**Fig. 3** Non-uniform scrap distribution inside the converter after simple rocking

**Obr. 3** Nerovnoměrné rozložení šrotu uvnitř konvertoru po jednoduchém naklopení

This is further evident in **Fig. 4**, where both iceberg formation and non-uniformly distributed scrap persist, even after interaction with the hot metal during pouring and subsequent furnace rotation. It is important to note that in real situation, the scrap pile begins to melt upon initial contact with the hot metal due to the temperature gradient and carbon diffusion (commonly referred to as dissolution melting). As melting progresses, the pile gradually collapses, leading to potential reduction of iceberg formation. Therefore, these phenomena will be further investigated by the current author.

Hutnické listy – *Metallurgical Journal*
Speciální vydání / Special Issue, roč. / vol. LXXIX
ISSN Online: 3029-8350

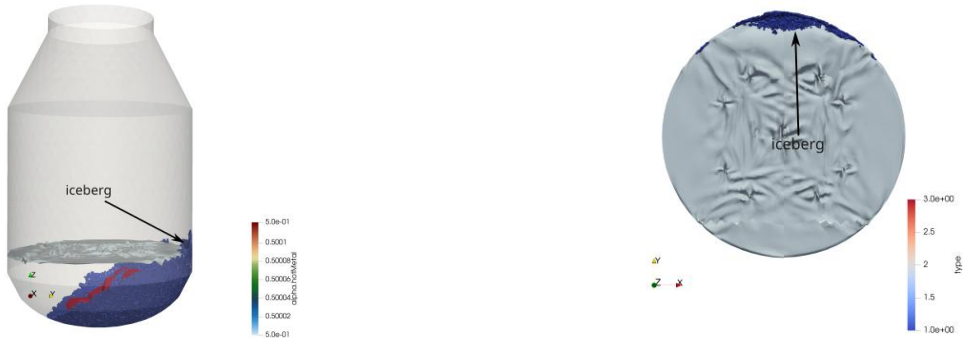


(a) (b)

**Fig. 4** Iceberg formation near the furnace wall as a result of simple rocking furnace leading to uneven distribution of scrap (colored by type Red for heavy, gray for medium and blue for light) at the end of the furnace rotation and prior to the blowing stage. (a) the side view of the furnace, (b) the top of the scrap hot metal interface (colored by volume fraction)

**Obr. 4** Vznik tzv. *iceberg* struktur u stěny konvertoru v důsledku jejího naklápění, vedoucího k nerovnoměrnému rozložení šrotu (červeně těžký, šedě střední, modře lehký) před foukáním: (a) boční pohled na pec, (b) horní část rozhraní šrot–tekutý kov

## 3. Conclusion

CFD-DEM model of the BOF converter is developed to simulate the scrap and the hot metal interaction in an industrial scale furnace. Results of DEM simulation indicate the importance of scrap arrangements within the scrap-box on refractory wear. Specifically, horizontally packed scrap tends to concentrate in localized regions (compared to vertical packing), increasing wear potential. The model further demonstrates the significance of rocking operations by capturing the redistribution of scrap inside the converter, which becomes even more pronounced during interaction with the hot metal. Additionally, the model successfully predicts iceberg formation along the furnace walls in case of retarded melting.

## Acknowledgements

***This research was carried out under project number T20010 in the framework of the research Program of the Material innovation institute (M2i) (www.m2i.nl) supported by the Dutch government and TATA STEEL NETHERLANDS.***

## References

[1] A. Kemminger, F. Krause,and H.-J. Odenthal, "CFD simulation of top-blown converters," Oct. 2022.
[2] M. Lv, R. Zhu, Y. G. Guo, and Y. W. Wang, "Simulation of flow fluid in the BOF steelmaking process," *Metall. Mater. Trans. B Process Metall. Mater. Process. Sci.*, vol. 44, no. 6, pp. 1560–1571, Dec. 2013, doi: 10.1007/S11663-013-9935-4/FIG.S/12.
[3] Y. Wu, T. Oudshoorn, and P. Rem, "Modelling and optimization of an innovative facility for automated sorting of aluminium scraps," *Waste Manag.*, vol. 189, pp. 103–113, Dec. 2024, doi: 10.1016/j.wasman.2024.08.018.
[4] M. Vångö, S. Pirker, and T. Lichtenegger, "Unresolved CFD–DEM modelling of multiphase flow in densely packed particle beds," *Appl. Math. Model.*, vol. 56, pp. 501–516, Apr. 2018, doi: 10.1016/J.APM.2017.12.008.
[5] T. M. J. Nijssen, J. A. M. Kuipers, J. Van Der Stel, A. T. Adema, and K. A. Buist, "Large-scale VOF/CFD-DEM Simulation of Blast Furnace Hearth Dynamics," *ISIJ Int.*, vol. 62, no. 6, pp. 1146–1158, Jun. 2022, doi: 10.2355/ISIJINTERNATIONAL.ISIJINT-2021-521.
[6] H. R. Norouzi, R. Zarghami, R. Sotudeh-Gharebagh, and N. Mostoufi, *Coupled CFD-DEM Modelling: Formulation, Implementation and Application to Multiphase Flows*. wiley, 2016. doi: 10.1002/9781119005315.
[7] C. Goniva, C. Kloss, N. G. Deen, J. A. M. Kuipers, and S. Pirker, "Influence of rolling friction on single spout fluidized bed simulation," *Particuology*, vol. 10, no. 5, pp. 582–591, Oct. 2012, doi: 10.1016/J.PARTIC.2012.05.002.
[8] P. A. Cundall and O. D. L. Strack, "A discrete numerical model for granular assemblies," *https://doi.org/10.1680/geot.1979.29.1.47*, vol. 29, no. 1, pp. 47–65, May 2015, doi: 10.1680/GEOT.1979.29.1.47.
[9] "DCS Computing," DCS Computing GmbH. Accessed: Jun. 19, 2025. [Online]. Available: https://www.aspherix-dem.com/
[10] "OpenFOAM 10 | OpenFOAM." Accessed: Jun. 19, 2025. [Online]. Available: https://openfoam.org/version/10/
[11] I. Finnie, "Erosion of surfaces by solid particles," *Wear*, vol. 3, no. 2, pp. 87–103, Mar. 1960, doi: 10.1016/0043-1648(60)90055-7.

Hutnické listy – *Metallurgical Journal*
Speciální vydání / Special Issue, roč. / vol. LXXIX
ISSN Online: 3029-8350

# Numerical and Water Modelling Study on Electromagnetic Stirring Technology in Steelmaking

# Numerické a vodní modelování technologie elektromagnetického míchání používané při výrobě oceli

**Monika Zielinska[1,2], Lidong Teng[3], Lukasz Madej[2], Lukasz Malinowski[1]**

[1] ABB Corporate Technology Center, ABB Sp. z o. o., 1 Żeganska Street, 04-713 Warsaw, Poland, *Contact e-mail: monika.zielinska@pl.abb.com

[2] Department of Applied Computer Science and Modelling, AGH University of Krakow, Mickiewicza 30 av., 30-059 Krakow, Poland

[3] ABB Metallurgy, Process Automation, ABB AB, Terminalvägen 24, SE-72159, Västerås, Sweden

## Abstract

*Electromagnetic stirring (EMS) technology has been applied for electric arc furnace (EAF), ladle furnace (LF) and tundish. The general purpose of such an application is to increase mixing and improve process control, while there is a specific demand for each type of analysed devices. A numerical study is executed for EAF, LF and tundish, focusing on stirring speed, specific stirring energy and mixing time evaluations. The comprehensive research is extended with water modelling for both LF and tundish. The results confirm the good performance of the electromagnetic stirring solutions and full control of the flow inside the metallurgical devices.*

***Keywords:*** *electromagnetic stirring, electric arc furnace, ladle furnace, tundish, computational fluid dynamics*

## Abstrakt

*Technologie elektromagnetického míchání (EMS) se uplatňuje v elektrických obloukových pecích (EOP), pánvových pecích (LF) a mezipánvích. Obecným cílem těchto aplikací je zvýšení intenzity promíchání a zlepšení řízení procesu, přičemž pro každý typ zařízení existují specifické požadavky. Byla provedena numerická studie pro EOP, LF a mezipánve se zaměřením na vyhodnocení rychlosti míchání, specifické energie míchání a doby homogenizace. Výzkum byl dále rozšířen o fyzikální modelování na vodních modelech pro LF i mezipánve. Výsledky potvrzují vysokou účinnost elektromagnetického míchání a možnost efektivního řízení proudění uvnitř metalurgických zařízení.*

***Klíčová slova:*** *elektromagnetické míchání, elektrická obloukova pec, pánvová pec, mezipánev, numerická analýza proudění*

## 1. Introduction

Nowadays, the steelmaking industry is one of the most significant industries globally. The demand for steel has been increasing over the last 50 years, and currently, steel accounts for approximately 95% of total metal production. Importantly, this growing demand is anticipated to continue in the near future, driven by the rapid development of various industries [1]. Conversely, steelmaking processes are highly intensive in carbon dioxide emissions, accounting for up to 10% of the total global emission [2-4]. A similar scenario exists regarding greenhouse gas emissions, which account for 7% of the global total. Consequently, restrictive environmental regulations have been implemented, compelling the steelmaking industry to make substantial changes in both local and global operations [5].

Hutnické listy – *Metallurgical Journal*
Speciální vydání / Special Issue, roč. / vol. LXXIX
ISSN Online: 3029-8350

Meeting these regulations will require significant effort from the steel industry to comply and enhance technologies to reach the established goals [6, 7]. All of these factors indicate that the steelmaking industry is in a transition phase, with the primary goal of significantly reduction of the $CO_2$ emissions and achieving climate neutrality as much as possible [2, 5, 8, 9]. Reducing $CO_2$ emissions and greenhouse gases requires the exploration of new technologies. One solution is electric steelmaking. This technology is based on electricity and currently accounts for 28% of global steel production, resulting in $CO_2$ emissions of about 7% [10]. However, to effectively replace blast furnace technology, large EAF units ranging from 150 to 350 tons are necessary. In this scenario, processes like stirring are essential to maintain high efficiency and steel quality. Without stirring in the EAF, the process efficiency would be considerably lower than that of the basic oxygen furnace [11, 12]. Further mixing can be achieved with neutral gas injection or enhanced electromagnetic stirring (EMS) technologies [13]. For the electric arc furnace (EAF), supplementary equipment such as a ladle furnace (LF) and tundish is necessary to improve steel quality. In these processes, stirring technologies play a vital role.

The above factors drive the rapid development of EMS technologies for EAF, LF, and tundish, including the need for efficient mixing throughout the bath and enhancing steel productivity while maintaining high-quality final products.

Given the challenges in conducting real experiments, this work presents a numerical approach that will be extended to water modelling for selected devices.

## 2. Methodology

The study was conducted on specific full-scale industrial devices, including a 450-ton electric arc furnace (EAF), a 160-ton ladle furnace (LF), and a 40-ton multi-strand billet caster tundish. **Fig. 1** shows the geometries of these devices along with the position of the EMS stirrer.

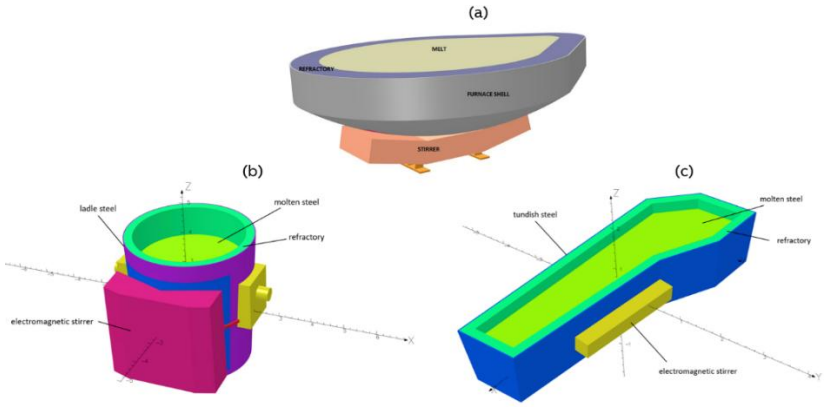


**Fig. 1** Geometry of the selected devices: (a) 450-ton EAF, (b) 160-ton LF and (c) 40-ton tundish

**Obr. 1** Geometrie vybraných zařízení: (a) 450 t EOP, (b) 160 t pánvová pec a (c) 40 t mezipánev

## 3. Numerical simulation approach

The numerical simulations rely on the computational fluid dynamics (CFD) method and are conducted using the commercial software ANSYS Fluent. However, the modelling of the electromagnetic forces influencing the melt and driving the steel flow in the EMS approach is accomplished through User Defined Functions (UDFs) developed in this work, which are thoroughly detailed in the paper [14].

Hutnické listy – *Metallurgical Journal*
Speciální vydání / Special Issue, roč. / vol. LXXIX
ISSN Online: 3029-8350

The CFD numerical investigations focus on analyzing the melt behavior. The refractory, shell, and geometry of the stirrer are included only for illustration and are not part of the analysis. Additionally, the slag layer is not considered in this research. The electromagnetic forces are represented by an additional source term that acts on the melt. The numerical method incorporates both single-phase and multiphase models to predict mixing and temperature uniformity throughout the entire geometry of the furnace. For the multiphase approach, this model is further enhanced to include phases of steel and top gas. It features defined boundary conditions to accurately represent real-world conditions. The external surfaces of the melt are treated as walls with no-slip boundary conditions, except for the top surface, which is modelled as a wall with zero shear stress in the single-phase model and as a pressure outlet in the multiphase model to accurately reflect the external atmosphere of the furnace.

The molten steel is treated as an incompressible, viscous fluid because of the turbulent flow within the vessel. For the simulation, where the temperature distribution and temperature homogenization are considered, additional properties such as specific heat and thermal conductivity are defined. The material properties are gathered in **Tab. 1**.

**Tab. 1** Material properties of steel used in the numerical simulation
**Tab. 1** Materiálové vlastnosti oceli použité pro numerickou simulaci

| Material properties | EAF | LF | Tundish |
|---|---|---|---|
| Melt density [kg/m$^3$] | 6900 | 6900 | 7200 |
| Melt viscosity [kg/(m s)] | 0.0072 | 0.0069 | 0.0072 |
| Specific heat [J/(kg K)] | 792 | - | 692 |
| Thermal conductivity [W/(m K)] | 35 | - | 35 |

In the numerical study, to confirm the effectiveness of the stirring, three different analyses are conducted:

1. EAF – temperature homogenization, where the temperature gradient between the bottom temperature equal to 1560 °C and the top temperature equal to 1620 °C is assumed as a starting point. The goal of the simulation is to measure the homogenization time, when the difference between the maximum and minimum temperature in the bath is less than 5 °C. The simulation with an electromagnetic stirrer is compared to the simulation with a non-stirred bath, whereas a natural stirring, assuming 5% of the maximum EMS power, is considered and is treated as a reference.
2. LF – the mixing time simulation involves an additional tracer defined by the User Defined Scalar (UDS), with concentration monitored over time at specific locations. The initial UDS concentration is defined in the designated open-eye area [15], after which it is mixed and tracked throughout the entire melt domain. The dimensionless concentration of the tracer allows to determine the mixing time when 95% of the homogenization is achieved [16]. The numerical simulation of the tundish with vertical and horizontal EMS systems is compared to the reference case with gas stirring.
3. Tundish – similar to LF, the numerical simulation for tundish is prepared to assess the mixing efficiency realized by the UDS tracer. However, for tundish, the flow control theory [17, 18] is included to designate the active and dead zones in the volume of tundish. The CFD simulation with the EMS system is compared to the reference case without any flow control device.

Hutnické listy – *Metallurgical Journal*
Speciální vydání / Special Issue, roč. / vol. LXXIX
ISSN Online: 3029-8350

The schematic presentation of the LF numerical setup with the location of the measurement points is presented in **Fig. 2**.

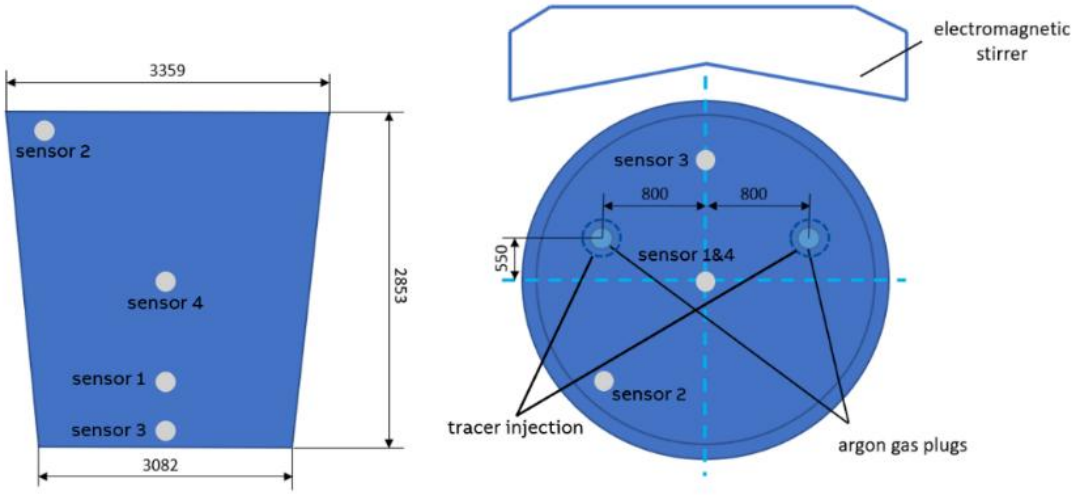


**Fig. 2** The scheme of the 160-ton LF geometry with position of the sensors to monitor of the tracer concentration injected above the gas plugs position

**Obr. 2** Schéma geometrie 160 tun pánvové pece s umístěním senzorů pro monitorování koncentrace indikátoru vstřikovaného nad dmyšnými elementy

## 4. Water modelling

The water model experiment was conducted in the dedicated water laboratory and executed only for LF and tundish. Water serves as an effective alternative to molten steel because the kinematic viscosity of water at 20 °C is similar to that of steel at 1600 °C [19]. An added benefit of this solution is that the experiment can be conducted at room temperature under isothermal conditions or with temperature variations, without the need to heat to extremely high temperatures like those required for steel to achieve a liquid state. This makes it easy to prepare and safe for individuals [20].

Both models for the LF and tundish are geometrically scaled. Additionally, to maintain similarity between the numerical and water models, the conditions for the submerged water pumps, which create the EMS stirring, must be accurately scaled. Since the primary aim of the analysis is to comprehend the flow behaviour and demonstrate mixing efficiency, the Froude number is chosen to ensure flow behaviour similarity [21-24]:

$$Fr = \frac{u_m}{\sqrt{gD_m}} = \frac{u_s}{\sqrt{gD_s}}, \tag{1}$$

where: $Fr$ – Froude number, $u_m$ – velocity in the water model [m/s], $u_s$ – velocity in the steel [m/s], $g$ – gravitational acceleration [m/s$^2$], $D_m$ – diameter of the water model [m], $D_s$ – diameter of the real furnace [m].

The numerical simulations allowed for the selection of a specific area in the furnace to assess the steel's velocity. This same area was examined in the water models, where the velocity in key regions was measured using a velocity meter.

Hutnické listy – *Metallurgical Journal*
Speciální vydání / Special Issue, roč. / vol. LXXIX
ISSN Online: 3029-8350

In the water model experiments, the setup of the analysis reflects the process simulated by the CFD approach.

To assess the effectiveness of the EMS stirring, the following analyses are conducted:

1. LF – the mixing time measurement is realized by the injection of the 20% salt solution on the surface of the water in the same position as in the CFD simulation. Again, the dimensionless concentration of the salt is measured in the same places as in the numerical simulation. The same condition of 95% of the homogenization is included to be able to compare the obtained results with the numerical solution.
2. Tundish – again, the setup of the water model experiment includes tracking of the injected salt solution. Based on the measurements, the active and dead zones based on the flow control theory were designated to compare the laboratory experiment to the numerical simulations. Moreover, the additional analysis with the injection of the dye via the inlet into the tundish enables the measurements of the mixing time. The measurements were performed for a reference case without stirring and for a case with stirring.

The water model setup for LF and tundish is presented in **Fig. 3**.

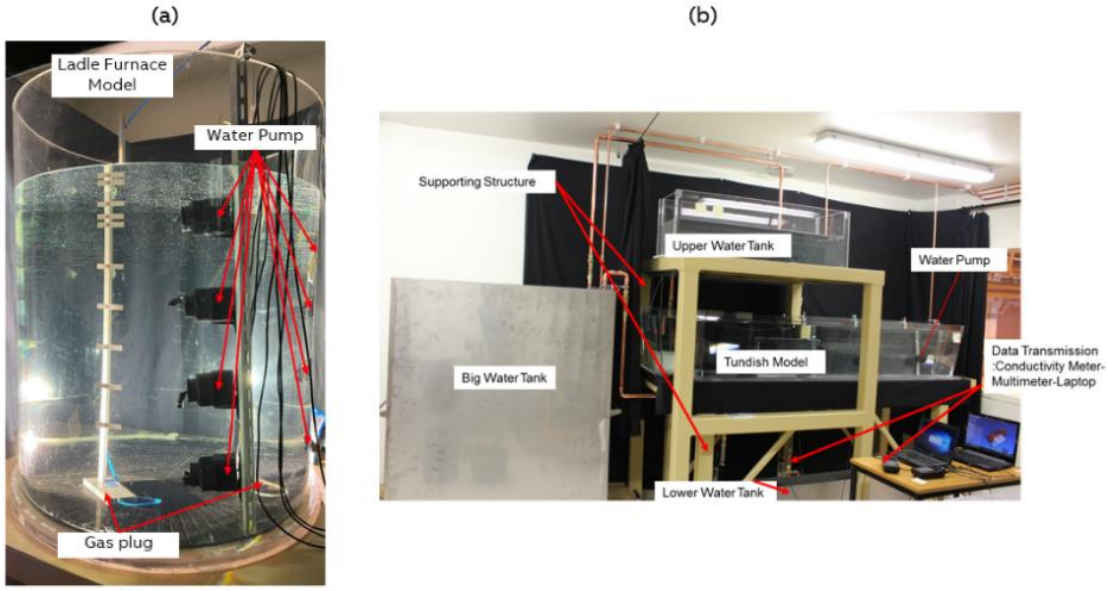


**Fig. 3** The water model setup prepared for (a) ladle furnace and (b) tundish

**Obr. 3** Sestava vodního modelu: (a) pánvová pec a (b) mezipánev

## 5. Results

The numerical simulation of the EAF, assuming a temperature gradient at the beginning of the simulation, enables the investigation of the temperature homogenization time, when the temperature difference between the maximum and minimum values in the bath is less than 5 °C. The temperature changes in time for two cases: 5% of the EMS corresponding to the natural processes inside the furnace and 100% of the EMS acting from the slag door to the EBT (Eccentric Bottom Tapping) direction is presented in **Fig. 4**, while the graphical interpretation of the changes is presented in **Fig. 5**.

Hutnické listy – *Metallurgical Journal*
Speciální vydání / Special Issue, roč. / vol. LXXIX
ISSN Online: 3029-8350

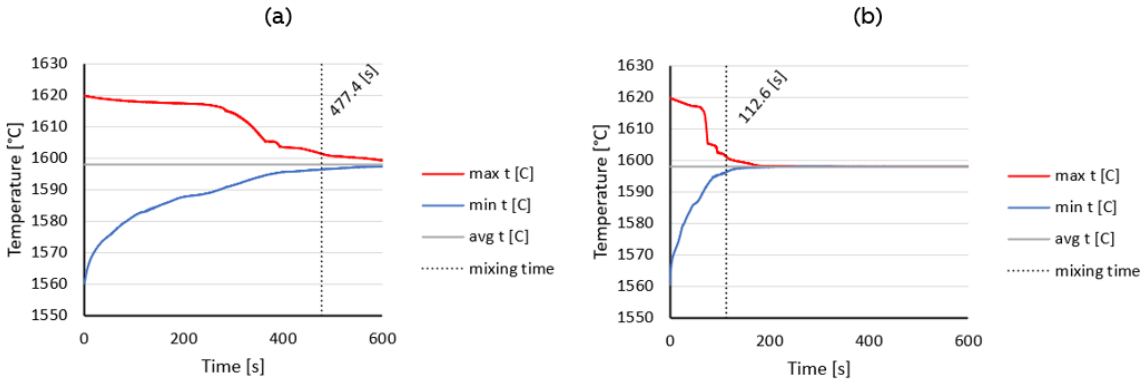


**Fig. 4** The temperature changes in time for (a) 5% of the EMS power corresponding to the natural processes and (b) 100% of the EMS power with the direction of stirring from door to EBT in the 450-ton EAF

**Obr. 4** Změny teploty v čase při (a) 5% výkonu EMS, což odpovídá přirozeným procesům a (b) 100% výkonu EMS se směrem míchání od struskového k odpichovému otvoru u 450 t EOP

The 5% of the EMS power as an indicator of natural mixing processes was designated based on a separately conducted experiment for a 90-ton furnace, where a copper tracer was implemented into the molten steel.

The measurements of the Cu content confirm that the homogenization time for EMS power on is equal to 62 s, while with EMS power off is equal to 260 s. It means that the mixing time with EMS is 24% of the time without EMS, which can be directly compared to the CFD simulation and confirms that the 5% of the EMS power is a correct assumption to include the impact of natural mixing inside the bath. The measurements are treated as a validation of the numerical approach [25].

The numerical and water model study conducted for LF enables a comparison of the efficiency of the EMS solution with the reference case that includes gas stirring. The dimensionless mixing time curves were prepared to assess the efficiency of the homogenization of the composition of the steel in the case of the alloy additions mixing process.

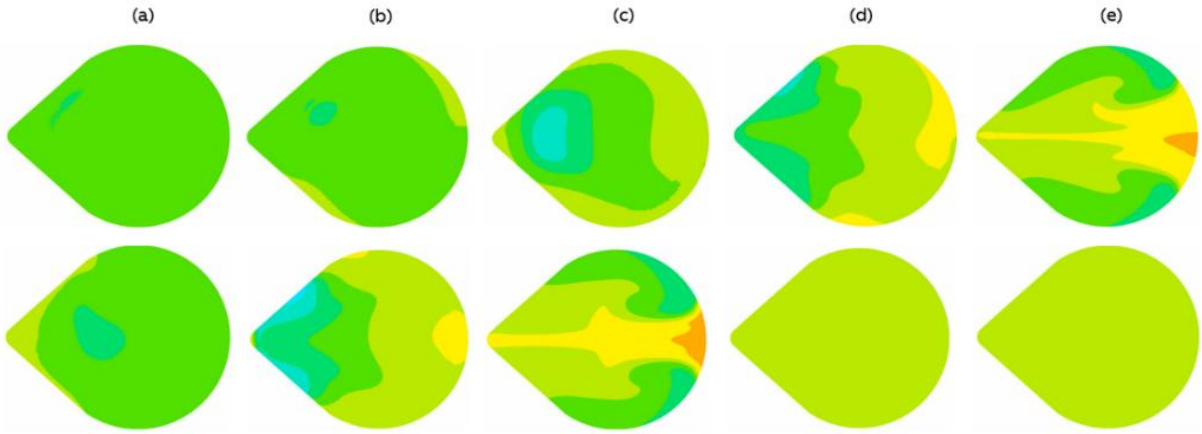


**Fig. 5** Temperature distribution in time for 5% of EMS (top) and 100% of EMS (bottom) with the stirring direction from door to EBT in the 450-ton EAF for (a) 5 s, (b) 20 s, (c) 50 s, (d) 100 s and (e) 200 s

**Obr. 5** Časový průběh rozložení teploty pro 5% EMS (nahoře) a 100% EMS (dole) při směru míchání od struskového k odpichovému otvoru u 450 t EOP po (a) 5 s, (b) 20 s, (c) 50 s, (d) 100 s a (e) 200 s

Hutnické listy – *Metallurgical Journal*
Speciální vydání / Special Issue, roč. / vol. LXXIX
ISSN Online: 3029-8350

The numerical results and the water modelling confirm, that the EMS stirrer is definitely a more efficient solution for mixing. Moreover, the new proposed horizontal stirring in ladle furnace, which is characterised by an elongated mixing time, is expected to have a controllable flow pattern and can be beneficial in refining processes [14, 26]. The comparison between the mixing curves for numerical simulation and water experiment is presented in **Fig. 6**.

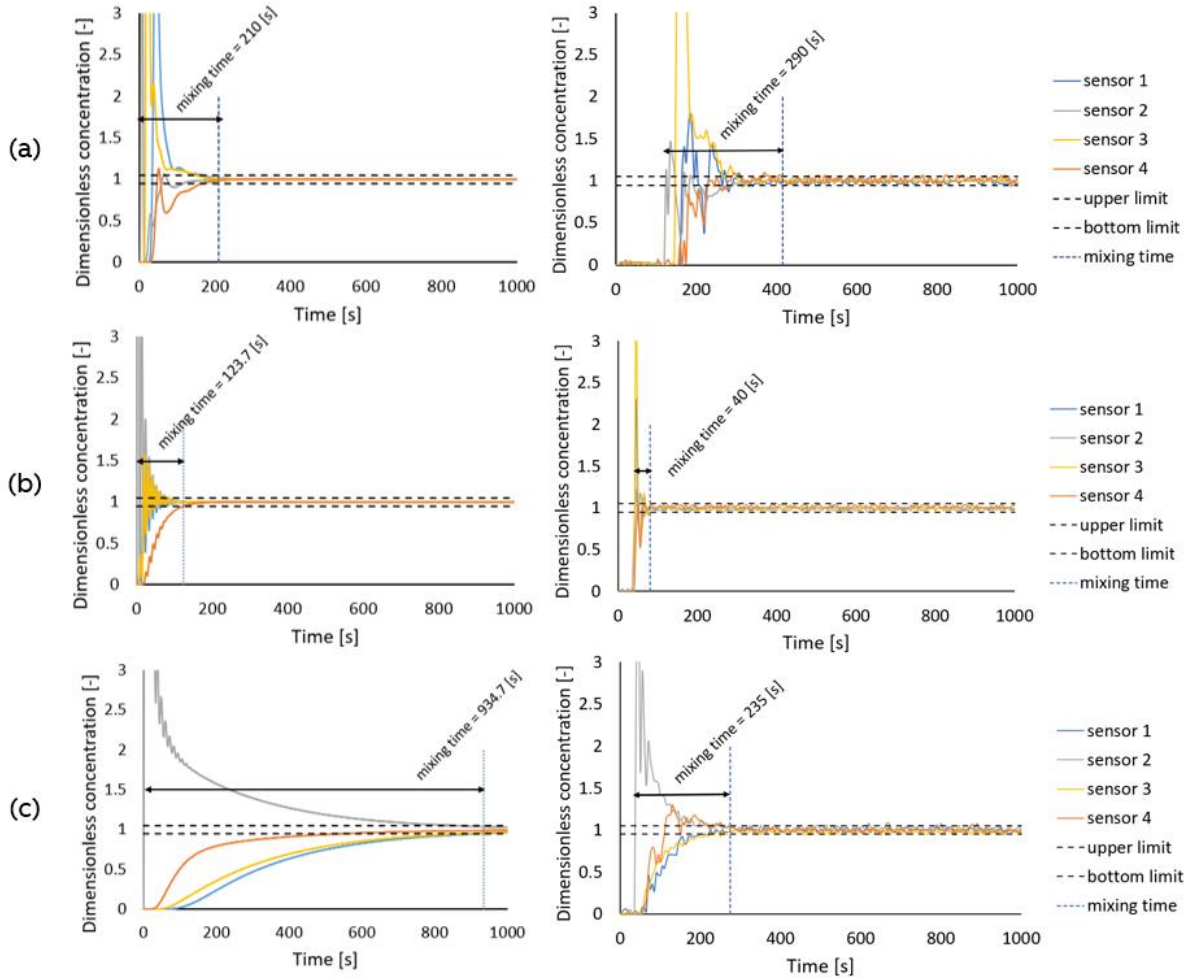


**Fig. 6** Mixing time comparison for numerical simulation (left) and water experiment (right) for (a) reference case with gas stirring, (b) vertical EMS stirring and (c) horizontal EMS stirring in the 160-ton ladle furnace

**Obr. 6** Srovnání doby míchání v numerické simulaci (vlevo) a na vodním modelu (vpravo) pro (a) referenční případ s mícháním plynem, (b) vertikální míchání pomocí EMS a (c) horizontální míchání pomocí EMS u 160 t pánvové peci

The additional analysis focuses on the numerical simulation and water experiment for the 40-ton multi-strand tundish. In similarity like in the LF, the tundish is investigated in the efficiency of the mixing process. The RTD curves are measured based on the salt concentration to be able to assess the active and dead zones.

The conducted research confirms the high efficiency of the EMS stirring, as the mixing curves are similar to those of ideal mixing. Moreover, all strands are characterized by similar behaviour, what confirms the great homogeneity of the flow. The comparison between the numerical and water models is presented in **Fig. 7**.

Hutnické listy – *Metallurgical Journal*
Speciální vydání / Special Issue, roč. / vol. LXXIX
ISSN Online: 3029-8350

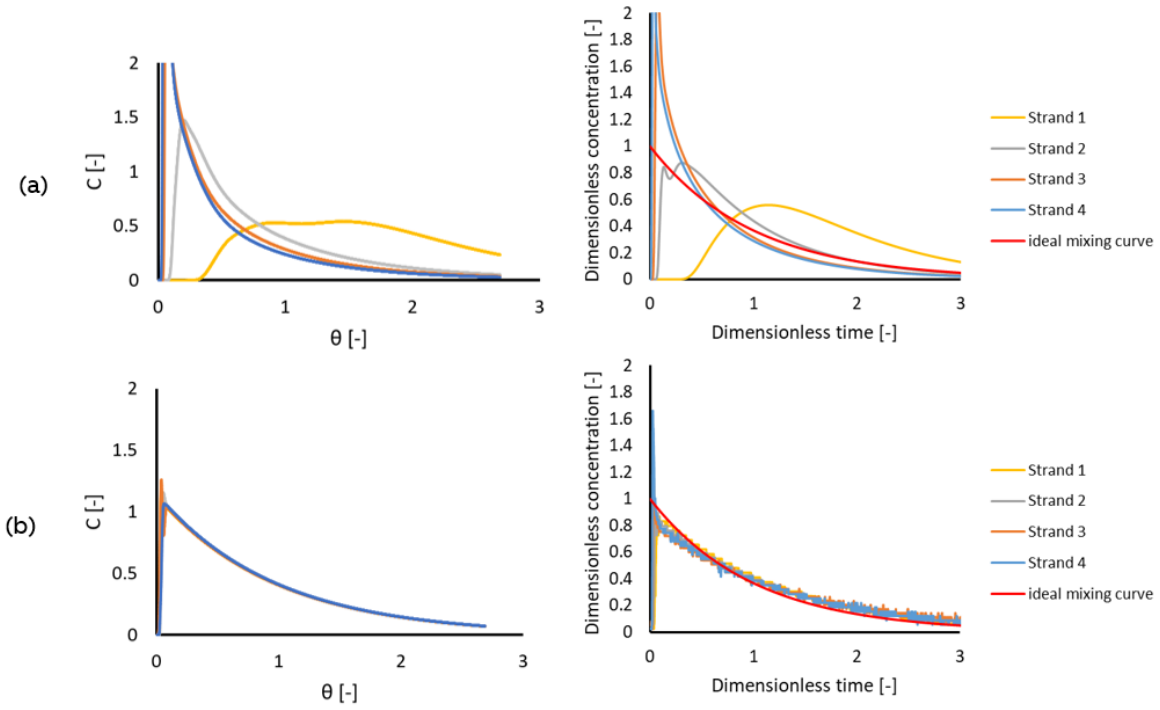


**Fig. 7** RTD curves comparison for numerical simulation (left) and water experiment (right) for (a) reference case without any control device and (b) EMS stirring in the 40-ton multi-strand billet caster tundish

**Obr. 7** Porovnání RTD křivek získaných numerickou simulaci (vlevo) a vodním modelem (vpravo) pro (a) referenční případ bez jakéhokoli regulačního zařízení a (b) míchání pomocí systému EMS ve víceproudé mezipánvi

To extend the research, mixing time measurements were conducted using the dye implementation via the inlet to the water. The study confirmed, that the homogenization time for EMS stirring is only 29 s, while for reference case without stirring, the mixing time is around 567 s.

## 6. Conclusions

- The conducted research clearly confirms that the EMS stirrer implementation improves the performance of the metallurgical vessels and is characterized by the high efficiency of the mixing on different stages of the molten steel path.
- The processes can be easily controlled by the EMS power changes and can be fitted to the existing furnace's geometries and capacities, which can be beneficial in the case of the replacement process of blast furnaces by EAFs.
- Moreover, thanks to the additional electromagnetic stirring, a more homogeneous composition of the steel is expected, which can directly influence the quality of the final product and reduce operational issues during the processes.

**Acknowledgements**

***The research within the industrial doctorate project co-financed by the Ministry of Science and Education.***

Hutnické listy – *Metallurgical Journal*
Speciální vydání / Special Issue, roč. / vol. LXXIX
ISSN Online: 3029-8350

## References

[1] Sovacool, B. K., Kim, J. & Yang, M. The hidden costs of energy and mobility: A global meta-analysis and research synthesis of electricity and transport externalities. *Energy Res Soc Sci* 72, 101885 (2021).
[2] Vogl, V., Olsson, O. & Nykvist, B. Phasing out the blast furnace to meet global climate targets. *Joule* 5, 2646–2662 (2021).
[3] European Commission. *Emissions Database for Global Atmospheric Research (EDGAR).* (2020).
[4] IEA. *Iron and Steel Roadmap (International Energy Agency).* (2020).
[5] Nilsson, L. J. *et al.* An industrial policy framework for transforming energy and emissions intensive industries towards zero emissions. *Climate Policy* 21, 1053–1065 (2021).
[6] Rogelj, J. *et al.* A new scenario logic for the Paris Agreement long-term temperature goal. *Nature* 573, 357–363 (2019).
[7] Rogelj, J. *et al.* Energy system transformations for limiting end-of-century warming to below 1.5 °C. *Nat Clim Chang* 5, 519–527 (2015).
[8] Somers, J. *Technologies to Decarbonise the EU Steel Industry*. (2021).
[9] Griffin, P. W. & Hammond, G. P. The prospects for 'green steel' making in a net-zero economy: A UK perspective. *Glob Transit* 3, 72–86 (2021).
[10] Wang, P. *et al.* Efficiency stagnation in global steel production urges joint supply- and demand-side mitigation efforts. *Nat Commun* 12, 2066 (2021).
[11] Cicutt, C. E., Valdez, M., Pérez, T., Donayo, R. & Petroni, J. Analysis of Slag Foaming During the Operation of an Industrial Converter. *Latin American Applied Research - An international journal* 32, 237–240 (2002).
[12] Lee, B. & Sohn, I. Effect of Hot Metal on Decarburization in the EAF and Dissolved Sulfur, Phosphorous, and Nitrogen Content in the Steel. *ISIJ International* 55, 491–499 (2015).
[13] Conejo, A. N. & Yan, Z. Electric Arc Furnace Stirring: A Review. *Steel Res Int* 94, (2023).
[14] Zielinska, M., Yang, H., Madej, L. & Malinowski, L. Development and Validation of Computational Fluid Dynamics Model of Ladle Furnace with Electromagnetic Stirring System. *Materials* 17, 960 (2024).
[15] Ramasetti, E. K. *et al.* Numerical Modelling of Open-Eye Formation and Mixing Time in Argon Stirred Industrial Ladle. *Metals (Basel)* 9, 829 (2019).
[16] Warzecha, M., Hutny, A., Warzecha, P., Kutyła, Z. & Merder, T. Investigations of Dual Plug Argon Blowing for Efficient Mixing at Ladle Furnace Station. *Archives of Metallurgy and Materials* 561–572 (2020) doi:10.24425/amm.2021.135893.
[17] Sahai, Y. & Emi, T. Melt Flow Characterization in Continuous Casting Tundishes. *ISIJ International* 36, 667–672 (1996).
[18] Sahai, Y. & Emi, T. *Tundish Technology for Clean Steel Production*. (WORLD SCIENTIFIC, 2007). doi:10.1142/6426.
[19] Mazumdar, D. & Evans, J. W. Macroscopic Models for Gas Stirred Ladles. *ISIJ International* 44, 447–461 (2004).
[20] Pan, Y. & Björkman, B. Physical and Mathematical Modelling of Thermal Stratification Phenomena in Steel Ladles. *ISIJ International* 42, 614–623 (2002).
[21] Sheng, D.-Y., Kim, C.-S., Yoon, J.-K. & Hsiao, T.-C. Water Model Study on Convection Pattern of Molten Steel Flow in Continuous Casting Tundish. *ISIJ International* 38, 843–851 (1998).
[22] Fukushi, K., Nogi, K. & Iguchi, M. Downward Air–Water Two-phase Flow Near the Outlet of a Model Immersion Nozzle. *ISIJ International* 46, 620–622 (2006).
[23] Kasai, N. & Iguchi, M. Water-model Experiment on Melting Powder Trapping by Vortex in the Continuous Casting Mold. *ISIJ International* 47, 982–987 (2007).
[24] Wuppermann, C. *et al.* A Novel Approach to Determine the Mixing Time in a Water Model of an AOD Converter. *ISIJ International* 52, 1817–1823 (2012).
[25] Teng, L. Yield Improvement with Electromagnetic Stirring in Electric Arc Furnace. in *Proceedings of the 7th International Congress on Science and Technology of Steelmaking (ICS 2018)* (2018).
[26] Zielinska, M., Yang, H., Madej, Ł. & Malinowski, Ł. Influence of Electromagnetic Field on Stirring Energy in Selected Metallurgical Equipment. *Steel Res Int* (2023) doi:10.1002/srin.202300534.

Hutnické listy – *Metallurgical Journal*
Speciální vydání / Special Issue, roč. / vol. LXXIX
ISSN Online: 3029-8350

# Hydrogen Removal during RH Degassing of Molten Steel: Real-Time Recurrence CFD Predictions and Validation using Plant Data

# Odstraňování vodíku během odplynění oceli procesem RH: Predikce v reálném čase pomocí CFD modelu a jeho validace využitím provozních údajů

**Xiaomeng Zhang[1], Maria Thumfart[1], Johann Wachlmayr[1], Christine Gruber[1], Roman Rössler[2], Daniel Queteschiner[3], Stefan Pirker[3]**

[1] K1-MET GmbH, Linz, Austria. *Contact e-mail: Xiaomeng.zhang@k1-met.com
[2] voestalpine Stahl GmbH, Linz, Austria
[3] Department of Particulate Flow Modelling, Johannes Kepler University, Linz, Austria

## Abstract

*In this study, data-assisted recurrence CFD (rCFD) is applied to efficiently simulate hydrogen degassing of molten steel in the RH vacuum process over time spans of tens of minutes. To ensure that numerical predictions are directly comparable to the hydrogen measured in the far-end off-gas stream at the plant, a transfer function is developed based on plant data, specifically, according to the relationship between injected lift-gas and its corresponding output in the off-gas. This function accounts for time delay and mixing effects as the gas reaches the monitoring point in the plant.*

*Initial comparisons show that rCFD predictions of hydrogen removal qualitatively agree well with plant data while enabling real-time predictions. To achieve quantitative agreement, further efforts are required to address uncertainties in hydrogen mass loss in off-gas measurement and to improve the model implementation in rCFD, particularly the calculation of hydrogen partial pressure. With validation established through plant data, rCFD's real-time predictive capability renders it a promising tool for three-dimensional digital twin applications in the RH process.*

***Keyword**: RH plant, CFD, recurrence CFD, hydrogen degassing*

## Abstrakt

*V této studii je využita metoda datově podporované rekurentní CFD (rCFD) k efektivní simulaci odstranění vodíku z roztavené oceli v RH vakuovém procesu odplynění v časovém horizontu desítek minut. Aby bylo zajištěno, že numerické predikce jsou přímo srovnatelné s koncentrací vodíku měřenou ve výstupním proudu odtahového plynu, byla na základě provozních dat navržena přenosová funkce, vycházející ze vztahu mezi vstřikovaným zdvihovým (nosným) plynem a jeho odezvou v odtahovém plynu. Tato funkce zohledňuje časové zpoždění a mísicí efekty při transportu plynu k místu měření.*

*Počáteční srovnání ukazují, že predikce rCFD týkající se odstraňování vodíku jsou v kvalitativní shodě s provozními daty a současně umožňují predikce v reálném čase. Pro dosažení kvantitativní shody je však nutné dále řešit nejistoty spojené s měřením úbytku vodíku v odtahovém plynu a zpřesnit implementaci modelu v rCFD, zejména výpočet parciálního tlaku vodíku. Díky validaci na základě provozních dat a schopnosti predikce v reálném čase představuje rCFD perspektivní nástroj pro aplikace trojrozměrných digitálních dvojčat v RH procesu.*

***Klíčová slova:** RH vakuovací stanice, výpočetní dynamika tekutin CFD, rekurentní CFD (rCDF), odstranění vodíku*

Hutnické listy – *Metallurgical Journal*
Speciální vydání / Special Issue, roč. / vol. LXXIX
ISSN Online: 3029-8350

## 1. Introduction

With the growing demand for sustainable steel production, enhancing the efficiency and precision of control in secondary refining processes, such as the Ruhrstahl-Heraeus (RH) process, has become increasingly critical to the steel industry. Due to the demanding process conditions (high temperatures, opaque liquids, and thick walls), CFD simulations have been an essential tool to better access and provide detailed three-dimensional insights into the fluid flow and mixing phenomena in the RH process. The turbulent and multiphase flow (particularly the interaction of rising bubble plumes and liquid steel) features in the process have been addressed by different models with varying levels of complexity [1-5]. A comprehensive review by Chen et al. [6] summarized recent progress in CFD modelling of argon-steel(-slag) multiphase flow in the RH process, covering aspects such as bubble dynamics, turbulence models, multiphase interactions, and validation techniques.

However, the high computational cost of conventional CFD simulations limits their application to short-term, offline analyses, making them unsuitable for real-time online process monitoring. To overcome this limitation, Lichtenegger and Pirker [7] proposed a fast simulation technique known as recurrence CFD (rCFD). This data-assisted methodology uses a database of characteristic flow patterns generated by conventional short-term CFD simulations and subsequently time-extrapolates these data to industrial process times. Without the need to solve the governing equations at each time step, rCFD dramatically reduces computational time, enabling real-time or even faster than real-time simulations of various industrial-scale cases such as steelmaking converter, ladle and tundish [7-9] and fluidized beds [10–12] as well as pollutant dispersion in built environments [13].

In this study, we apply transport-based rCFD [8] to efficiently simulate long-duration hydrogen degassing in an industrial RH plant. The simulation results are compared with plant off-gas hydrogen measurements to assess the model's predictive capability. Furthermore, we discuss the potential to quantitatively align simulation and plant data by addressing uncertainties in both the numerical model and measurement system. This work is part of an ongoing effort to calibrate and validate a real-time-capable simulation tool using plant data, with the long-term goal of supporting online process monitoring and control.

## 2. Modelling and Simulation

The overall workflow for (transport-based) rCFD simulations is outlined below. A more detailed description of the rCFD methodology can be found in [7, 8].

As a data-assisted method, rCFD simulation generally starts with conducting a conventional CFD simulation until the given process exhibits pseudo-periodic flow characteristics. Then, a recurrence database covering a limited process duration is generated from the CFD simulation. Finally, the transport of passive scalars (e.g., removal of hydrogen) can be simulated over any arbitrary long process time by utilizing the database.

In the context of gas-injection-driven circulating flow in the RH process, the initial CFD simulation employs a combination of: (1) the VOF method for the steel surface motion in the vacuum chamber, (2) the DPM model for the injected gas bubbles from the up-leg snorkel, and (3) LES approach for turbulence modelling.

Hutnické listy – *Metallurgical Journal*
Speciální vydání / Special Issue, roč. / vol. LXXIX
ISSN Online: 3029-8350

The modelling strategy is commonly adopted for bubble plume-induced flow and has delivered reasonable results in comparison with experimental studies and plant observations [1, 14]. For brevity, the CFD modelling details are omitted here and can be found in the references [1, 14].

Once the steel flow reaches pseudo-periodic states, a continuation of CFD simulations of such flow spanning a monitoring period $\tau_{rec}$ feed a recurrence database that is subsequently used for long-duration simulations. There are currently two main versions of rCFD, labeled flow-based rCFD and transport-based rCFD. For the flow-based version of rCFD, the entire flow field is stored in a regular time interval $\Delta t_{rec}$ over the period $\tau_{rec}$ (resulting in the number of $N_{rec}$ instant flow fields or data frames). With these flow fields, a recurrence analysis is performed based on a recurrence norm (rNorm), which is a scalar quantity that quantifies the system's degree of similarity at two different times (here, rNorm is linked to the fluid velocity). Applying rNorm to each pair of these $N_{rec}$ data frames results in a recurrence matrix (rMatrix) with $N_{rec}^2$ entries. The graphical representation of a rMatrix refers to a recurrence plot (as given by **Fig. 1(b)**), which always has a zero main diagonal as the frame is compared to itself and contains non-zero off-diagonal entries indicating whether two data frames are similar or not. Based on this information, a recurrence process (rProcess) can be constructed by stitching these flow sequences, with an emphasis on connecting similar states. For instance, starting at a certain time (or a certain data frame $N_m$), the subsequent ξ frames (ξ denotes a randomly chosen interval) are used consecutively. At frame $N_{m+\xi}$, frame $N_n$, which is the most similar to the current frame, is determined as the connecting frame. Then, having $N_n$ as the starting frame, same method is applied to look for the next frame that fits the previous sequence's end frame. This process can be repeated to obtain an arbitrarily long flow sequence. Then, passive scalars are traced on the extrapolated flow fields by solving transport equations. In contrast to flow-based rCFD, the transport-based rCFD doesn't store flow fields themselves.

Rather, an additional field transport equation is solved which essentially tracks the advection of cell coordinates. These advected cell coordinates are subsequently transformed into a series of cell-to-cell shifts which then constitutes the database. Based on these cell-to-cell shifts a passive scalar quantity is propagated from the very frame's start cells to the receiving end cells in each time step (following the rProcess described previously).

In addition to cell shifts, face swaps among neighbouring cells are adopted to mimic physical diffusion in order to get smooth and complete field information. The transport-based rCFD has shown further computational speed-up compared to the flow-based rCFD and is used in this study. The rCFD functionalities are implemented within the framework of ANSYS Fluent via UDFs.

In applying the transport-based rCFD to hydrogen degassing, the degassing rate under vacuum condition can be described by a first-order reaction model given by Equation (1), considering the mass transfer of [H] in the boundary layer of molten steel the rate-controlling step.

$$-\frac{dm_{[H]}}{dt} = \rho A k_{[H]}([H] - [H]_e) \quad (1)$$

In the above equation, ρ is the steel density, $A$ is reaction area between molten steel and the gas phase and $k_{[H]}$ is mass transfer coefficient with unit m/s. [H] and $[H]_e$ are mass fractions of [H] in steel and at surfaces (also equals to equilibrium content of element).

Hutnické listy – *Metallurgical Journal*
Speciální vydání / Special Issue, roč. / vol. LXXIX
ISSN Online: 3029-8350

$$K_{\mathrm{H}}^{\ominus} = \frac{\left(P_{\mathrm{H_2}}/P^{\ominus}\right)^{\frac{1}{2}}}{f_{[\mathrm{H}]}[\%\mathrm{H}]_{\mathrm{e}}} \tag{2}$$

$$\lg K_{\mathrm{H}}^{\ominus} = 1905/T + 1.591 \tag{3}$$

To implement Equation (1), the reaction area, mass transfer coefficient, and the equilibrium concentration are to be determined. The equilibrium content depends on the partial pressure of the reaction product $H_2$ and the thermodynamic equilibrium constant $K_{\mathrm{H}}^{\ominus}$ according to Equation (2) (the activity coefficient ($f_{[\mathrm{H}]}$) set to 1 for low-alloyed steels). The equilibrium constant is calculated by Equation (3) [15]. The mass transfer coefficient of hydrogen in molten steel is taken to be $k_{[\mathrm{H}]} = 1.42 \times 10^{-3}\mathrm{m.s^{-1}}$ [15]. Regarding reaction sites, this study assumes that the reaction primarily occurs in the vacuum chamber, supported by plant observations of the melt surface obtained from a high-speed camera, which reveals the presence of highly dynamic steel foam [16]. Given the much larger steel volume in the vacuum chamber compared to the up-leg snorkel, along with the high void fraction in the melt, a sufficiently large steel-gas interface is available. This, in turn, promotes an efficient degassing reaction in the vacuum chamber. The results of hydrogen degassing predicted by rCFD are presented subsequently.

## 3. Results and Discussion

The CFD simulation of the flow field in the RH plant, based on the modelling strategy described in the previous section, is shown in **Fig. 1(a)**. The characteristic recirculating flow pattern, driven by the injected bubbles at the up-leg snorkel, is well captured by the model. Once the flow structure is established, its dynamic behavior is further analysed using a recurrence plot, as presented in **Fig. 1(b)**. This plot visualizes the pairwise differences between frames for a total of 200 frames, covering a 20s process duration.

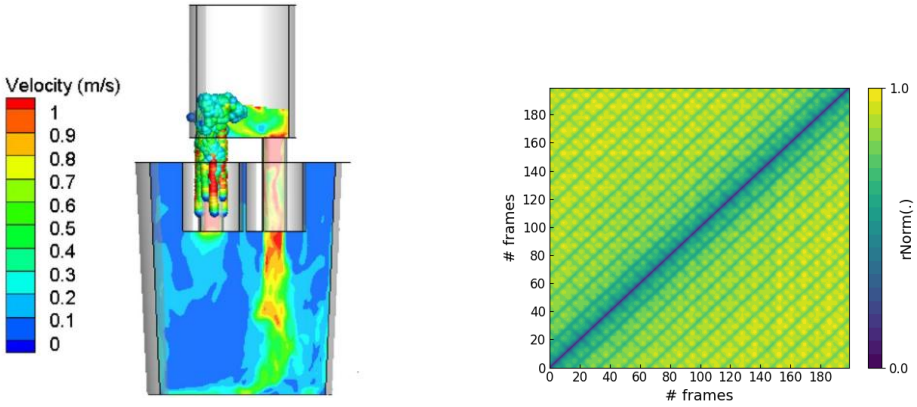


(a) (b)

**Fig. 1** (a) Characteristic circulating flow topology in the RH plant obtained from CFD simulations. (b) Recurrence plot of the global flow field, constructed from 200 data frames and evaluating the flow evolution over a 20s process duration. The color scale indicates the degree of pairwise similarity: dark blue indicates identical frames, while yellow represents the greatest dissimilarity between frames

**Obr. 1** (a) Charakteristika cirkulace proudění na vakuovací stanici RH získaná z CFD simulací. (b) Graf rekurentního pole proudění, sestavený z 200 datových snímků a zachycující vývoj proudění během 20sekundového procesu. Barevná stupnice udává míru párové podobnosti: tmavě modrá barva označuje identické snímky, zatímco žlutá barva představuje největší odlišnost mezi snímky

Hutnické listy – *Metallurgical Journal*
Speciální vydání / Special Issue, roč. / vol. LXXIX
ISSN Online: 3029-8350

Obviously, a zero-valued antidiagonal is present since it represents the comparison of a state with itself, resulting in no difference. In the off-diagonal region, distinct greenish parallel lines appear at constant intervals, indicating the periodic recurrence of similar flow states in the system. This recurrence behavior enables us to proceed with rCFD time extrapolation, as introduced earlier, and thereby efficiently simulate long-duration hydrogen degassing in the steel.

**Fig. 2** shows the evolution of hydrogen concentration in the steel at three-time instances (t = 7, 15, and 23min), as predicted by rCFD simulations. The contour plots clearly show that hydrogen degassing initiates in the vacuum chamber, with hydrogen-depleted steel re-entering the ladle by a downward jet.

Through global steel recirculation, dissolved hydrogen is gradually washed out of the ladle, eventually reaching a low concentration. In addition, the computational cost associated with rCFD simulation of hydrogen degassing is also presented in **Fig. 2**.

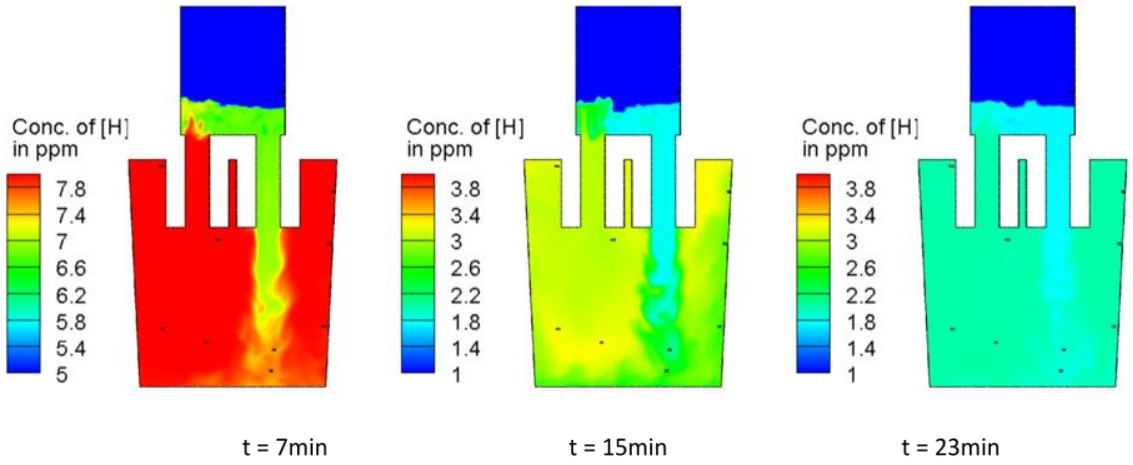


Computational efficiency of rCFD for hydrogen degassing

| $t_{process}$ | $t_{CPU}$ |
|---|---|
| 35min | 45min (rCFD run) |

**Fig. 2** Instantaneous hydrogen [H] concentration in the steel at three-time instances obtained from rCFD simulations, along with the corresponding computational efficiency of rCFD

**Obr. 2** Okamžitá koncentrace vodíku [H] v oceli ve třech časových okamžicích získaná z rCFD simulací spolu s odpovídající výpočetní účinností rCFD

The rCFD approach enables simulations at full grid resolution (2.5 million cells) with near real-time performance relative to the physical process time, which is not achievable using conventional full CFD simulations.

In addition to the time evolution of hydrogen concentration in the steel, the $H_2$ mass flow rate predicted by rCFD is compared with plant measurements of $H_2$ in the off-gas.

Since the simulation provides $H_2$ mass flow at the melt surface, while the measurements are taken at the far end of the off-gas pipeline, a transfer function is developed based on a specific type of plant treatment and applied to the simulation results. This function accounts for gas transport and mixing effects within the off-gas system.

Hutnické listy – *Metallurgical Journal*
Speciální vydání / Special Issue, roč. / vol. LXXIX
ISSN Online: 3029-8350

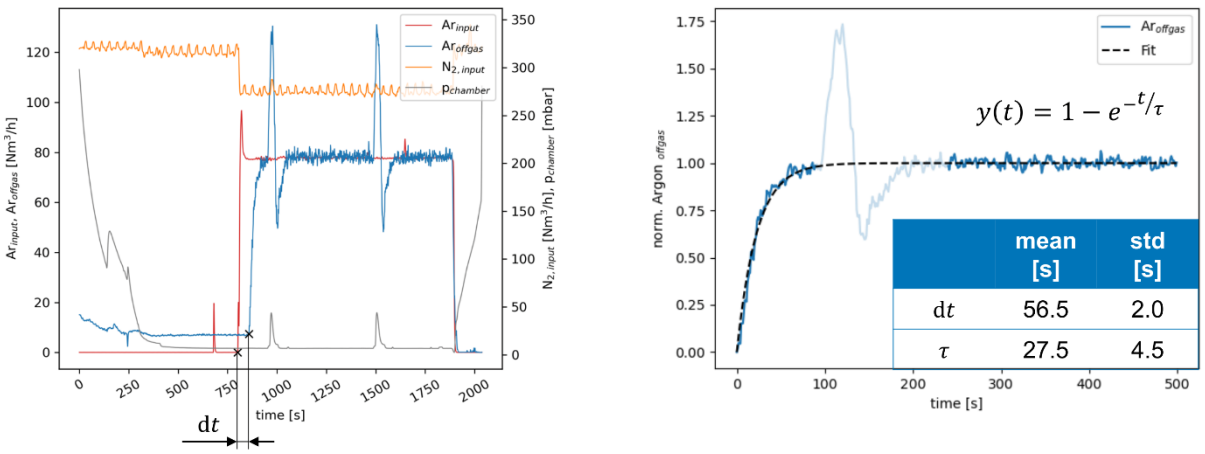


(a) (b)

**Fig. 3** (a) RH operation with a lift-gas switch from $N_2$ to Ar: the Ar flow rate in the off-gas (blue line) exhibits a time-delayed and smoother response compared to the lift-gas signal (red line), due to gas transport and mixing within the off-gas system. (b) Fitted curve of the normalized Ar flow rate measured in the off-gas [16]

**Obr. 3** Provoz RH stanice se změnou nosného plynu z $N_2$ na Ar: průtok Ar v odtahovém plynu (modrá čára) vykazuje oproti signálu nosného plynu (červená čára) zpožděnou a plynulejší odezvu, což je způsobeno transportem a mícháním plynů v odtahovém systému plynu. (b) Křivka normalizovaného průtoku Ar naměřeného v odtahovém plynu [16]

As shown in **Fig. 3(a)**, the plant operation includes a lift-gas switch from $N_2$ to Ar. By comparing the Ar signal in the off-gas (blue line) with the Ar input signal (red line), a time delay of approximately 57s and a smoother (less steep) output are observed. The Ar output, which represents the step response of the Ar input, is fitted with a curve and corresponding equation shown in **Fig. 3(b)**. To make the rCFD-predicted $H_2$ mass flow at the melt surface $\dot{m}_{\mathrm{H2,input}}(t)$ comparable to plant measurements, its output at the end of the off-gas stream $\dot{m}_{\mathrm{H2,output}}(t)$ is approximated by using convolution with the system's impulse response $h(t)$:

$$\dot{m}_{\mathrm{H2,output}}(t) = \dot{m}_{\mathrm{H2,input}}(t) * h(t) \tag{4}$$

Here, $h(t)$ is obtained by differentiating the fitted step response $y(t)$.

In **Fig. 4**, a comparison between rCFD predictions and plant measurements of the $H_2$ mass flow in the off-gas is presented. The rCFD results include the $H_2$ mass flow rate at the melt surface (blue lines) and the adjusted signal at the end of the off-gas stream (green lines), obtained by applying the transfer function described earlier.

The vacuum chamber pressure, which reduces from atmospheric pressure to around 5mbar during treatment, is also shown (black lines). The two subfigures correspond to different assumptions for calculating the equilibrium hydrogen content $[H]_e$: (a) using the chamber pressure as a simplification, and (b) using the $H_2$ partial pressure within the $H_2$-$N_2$-Ar gas mixture. It should be noted that case (b) still represents a simplified model and will be refined in future work.

In both cases, the predicted $H_2$ mass flow curves exhibit an initial rise followed by a gradual decay, which resembles similar main characteristics in comparison with plant data. The applied transfer function introduces a noticeable time delay and smoothing effect, aligning the simulation more closely with the measurement.

Hutnické listy – *Metallurgical Journal*
Speciální vydání / Special Issue, roč. / vol. LXXIX
ISSN Online: 3029-8350

However, the initiation of hydrogen degassing differs between the two cases due to the distinct equilibrium conditions arising from the different pressure assumptions. This leads to variations in the overall degassing behavior.

Given that the majority of the vacuum chamber is expected to be filled with the lift-gas Ar, using the $H_2$ partial pressure within the $H_2$–$N_2$–Ar gas mixture likely provides a more realistic representation on the degassing process.

Nonetheless, further refinement of the model is required to more accurately estimate the equilibrium hydrogen content. In comparison with plant data, a notable discrepancy remains: the total amount of $H_2$ detected in the off-gas is significantly lower in the plant measurements than predicted by simulations.

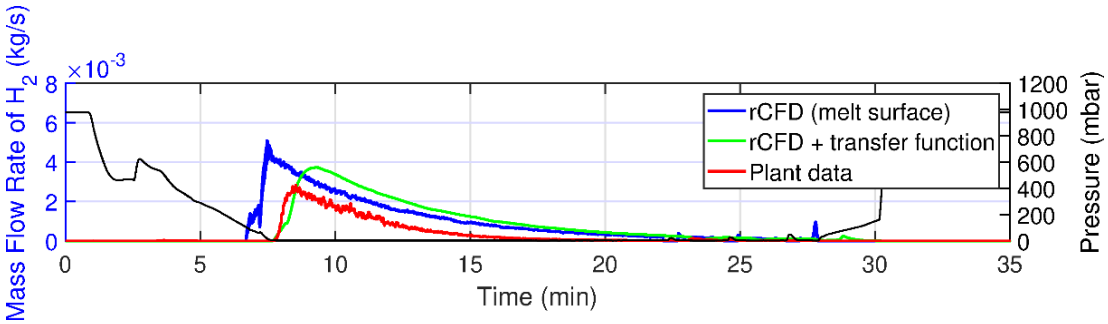


(a)

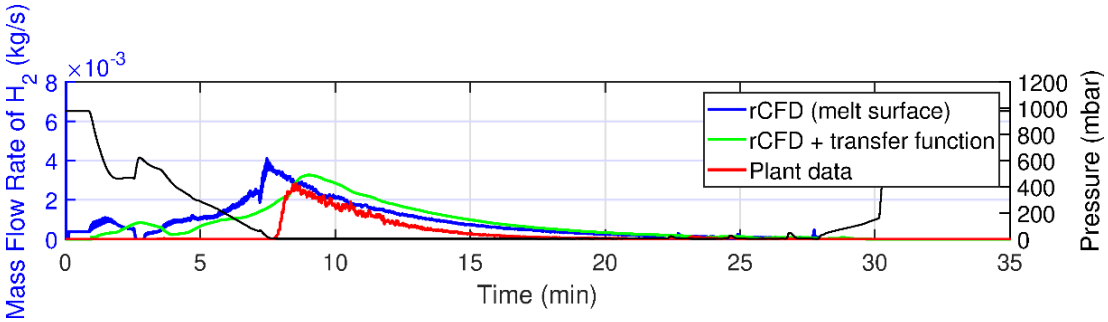


(b)

**Fig. 4** Comparison between rCFD predictions and plant measurements of $H_2$ mass flow rate in the off-gas. Both rCFD-predicted $H_2$ mass flow at the melt surface (bule line) and the corresponding signal after applying the transfer function (green line) are shown, along with the operating pressure (black line). In (a), the chamber pressure is used to calculate equilibrium H concentration for simplification, while (b) presents results using the $H_2$ partial pressure, accounting for the $H_2$-$N_2$-Ar gas mixture

**Obr. 4** Porovnání predikcí z rCFD a měření hmotnostního průtoku $H_2$ v odtahovém plynu provedených v provozních podmínkách. Jsou zde znázorněny jak hmotnostní průtok $H_2$ na povrchu taveniny predikovaný metodou rCFD (modrá čára), tak odpovídající signál po použití přenosové funkce (zelená čára), spolu s provozním tlakem (černá čára). V případě (a) se pro zjednodušení používá tlak v komoře k výpočtu rovnovážné koncentrace H, zatímco (b) představuje výsledky s použitím parciálního tlaku $H_2$, zohledňujícího směs plynů $H_2$-$N_2$-Ar

To further quantify hydrogen loss, the concentration of dissolved hydrogen in the steel before and after RH vacuum treatment is analysed. As shown in **Fig. 5**, the hydrogen loss determined from melt measurements closely matches the rCFD predictions. Minor discrepancies may stem from the assumption of a higher total steel mass in simulation compared to the actual ladle. In contrast, the hydrogen loss derived from the integral off-gas analysis is more than twice as low.

Hutnické listy – *Metallurgical Journal*
Speciální vydání / Special Issue, roč. / vol. LXXIX
ISSN Online: 3029-8350

Seemingly, at the plant, some hydrogen is 'lost' on the way to the final monitoring point. The underlying cause of this mass discrepancy remains uncertain. One hypothesis is that some hydrogen reacts with ambient oxygen in hot regions of the off-gas piping to form water vapor. This possibility is currently under investigation, with the aim of ensuring a reliable off-gas hydrogen signal for validating rCFD predictions.

Meanwhile, further improvement of the degassing model implementation in rCFD is essential to more accurately simulate the process. With proper validation, the real-time capable rCFD approach can be extended to support additional metallurgical processes, such as alloying.

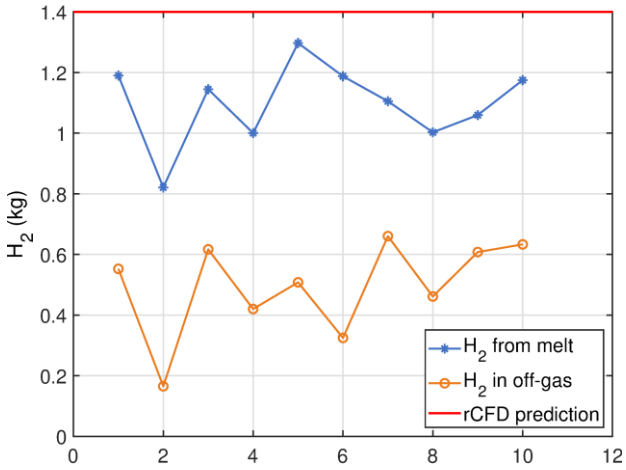


**Fig. 5** Comparison of hydrogen mass loss from the melt estimated by: (1) difference in hydrogen concentration in the melt before and after RH treatment (blue markers, based on analysis of multiple melts), (2) integration of $H_2$ mass flow rate measured in the off-gas (orange markers), and (3) integration of $H_2$ mass flow rate predicted by rCFD simulations (red line). The $H_2$ content estimated from the off-gas analysis is significantly lower than that determined from melt measurements

**Obr. 5** Srovnání úbytku vodíku (kg) z taveniny stanoveného na základě: (1) rozdílu v koncentraci vodíku v tavenině před a po zpracování na RH stanici (modrá křivka, analyzováno více tavenin), (2) integrace hmotnostního průtoku $H_2$ naměřeného v odtahovém plynu (oranožová křivka), a (3) integrace hmotnostního průtoku $H_2$ predikovaného rCFD simulacemi (červená čára). Obsah $H_2$ stanovený z analýzy odtahového plynu je výrazně nižší než obsah stanovený na základě měření taveniny.

## 4. Conclusion

- In this study, transport-based rCFD was applied to predict hydrogen degassing in an RH plant. Comparison with plant measurements of hydrogen in the off-gas shows that rCFD predictions qualitatively agree well with the plant data, while also offering real-time capable performance.
- To achieve quantitative alignment, further work should address uncertainties in hydrogen mass loss measurements and ensure accurate model implementation – particularly in the calculation of hydrogen partial pressure under degassing conditions.
- With validation established based on the hydrogen degassing case, the rCFD framework can be further extended to simulate additional metallurgical processes in the RH plant, such as alloying and decarburization. Ultimately, this paves the way for employing rCFD as a digital twin monitoring tool for efficient RH process operation.

Hutnické listy – *Metallurgical Journal*
Speciální vydání / Special Issue, roč. / vol. LXXIX
ISSN Online: 3029-8350

## Acknowledgements

***The authors gratefully acknowledge the funding support of K1-MET GmbH, metallurgical competence center. The research program of the competence center K1-MET is supported by COMET (Competence Center for Excellent Technologies), the Austrian program for competence centers.***

***COMET is funded by the Federal Ministry for Transport, Innovation and Technology, the Federal Ministry for Science, Research and Economy, the province of Upper Austria, Tyrol, and Styria, the Styrian Business Promotion Agency.***

***The authors moreover gratefully acknowledge financial support from the Austrian Research Promotion Agency (FFG) for the project OpTwinFlow (program "Produktion und Material", project number FO999899007).***

## References

[1] PIRKER, Stefan, PUTTINGER, Stefan, RÖSSLER, Roman and LICHTENEGGER, Thomas. Steel alloy homogenization during Rheinsahl–Heraeus Vacuum Treatment: Conventional computational fluid dynamics, recurrence computational fluid dynamics, and Plant Observations. Steel Research International, 2020, 91(12). DOI 10.1002/srin.202000214.

[2] HAAS, Tim, SCHUBERT, Christian, EICKHOFF, Moritz and PFEIFER, Herbert. Numerical modelling of the ladle flow by a les-based Eulerian–Lagrange Approach: A systematic survey. Metallurgical and Materials Transactions B, 2021, 52(2), pp. 903–921. DOI 10.1007/s11663-021-02064-2.

[3] LI, Baokuan and TSUKIHASHI, Fumitaka. Modelling of circulating flow in rh degassing vessel water model designed for two- and multi-legs operations. ISIJ International, 2000, 40(12), pp. 1203–1209. DOI 10.2355/isijinternational.40.1203.

[4] GENG, Dian-Qiao, ZHENG, Jin-Xing, WANG, Kai, WANG, Ping, LIANG, Ru-Quan, LIU, Hai-Tao, LEI, Hong and HE, Ji-Cheng. Simulation on decarburization and inclusion removal process in the ruhrstahl–heraeus (RH) process with ladle bottom blowing. Metallurgical and Materials Transactions B, 2015, 46(3), pp. 1484–1493. DOI 10.1007/s11663-015-0314-1.

[5] LING, Haitao, LI, Fei, ZHANG, Lifeng and CONEJO, Alberto N. Investigation on the effect of nozzle number on the recirculation rate and mixing time in the rh process using VOF + DPM model. Metallurgical and Materials Transactions B, 2016, 47(3), pp. 1950–1961. DOI 10.1007/s11663-016-0669-y.

[6] CHEN, Gujun, WANG, Qiangqiang and HE, Shengping. Computational fluid dynamics modelling of argon–steel (–slag) multiphase flow in an Ruhrstahl–Heraeus Degasser: A review of past numerical studies. Steel Research International, 2022, 94(1). DOI 10.1002/srin.202200298.

[7] LICHTENEGGER, T. and PIRKER, S. Recurrence CFD – a novel approach to simulate multiphase flows with strongly separated time scales. Chemical Engineering Science, 2016, 153, pp. 394–410. DOI 10.1016/j.ces.2016.07.036.

[8] PIRKER, S. and LICHTENEGGER, T. Efficient time-extrapolation of single- and multiphase simulations by transport based recurrence CFD (rCFD). Chemical Engineering Science, 2018, 188, pp. 65–83. DOI 10.1016/j.ces.2018.04.059.

[9] LUMETZBERGER, H., PIRKER, S. and LICHTENEGGER, T. Propagator-moments approximation for recurrence CFD: Application to species transport in turbulent flows. Chemical Engineering Science, 2025, 311, pp. 121624. DOI 10.1016/j.ces.2025.121624.

[10] LICHTENEGGER, T., PETERS, E.A.J.F., KUIPERS, J.A.M. and PIRKER, S. A recurrence CFD study of heat transfer in a fluidized bed. Chemical Engineering Science, 2017, 172, pp. 310–322. DOI 10.1016/j.ces.2017.06.022.

[11] LICHTENEGGER, T., KIECKHEFEN, P., HEINRICH, S. and PIRKER, S. Dynamics and long-time behavior of gas–solid flows on recurrent-transient backgrounds. Chemical Engineering Journal, 2019, 364, pp. 562–577. DOI 10.1016/j.cej.2019.01.161.

[12] DABBAGH, Firas, PIRKER, Stefan and SCHNEIDERBAUER, Simon. A fast modelling of chemical reactions in industrial-scale olefin polymerization fluidized beds using recurrence cfd. AIChE Journal, 2021, 67(5). DOI 10.1002/aic.17161.

[13] DU, Yaxing, BLOCKEN, Bert and PIRKER, Stefan. A novel approach to simulate pollutant dispersion in the built environment: Transport-based recurrence CFD. Building and Environment, 2020, 170, pp. 106604. DOI 10.1016/j.buildenv.2019.106604.

[14] PIRKER, S., AIGNER, A. and WIMMER, G. Experimental and numerical investigation of sloshing resonance phenomena in a spring-mounted rectangular tank. Chemical Engineering Science, 2012, 68(1), pp. 143–150. DOI 10.1016/j.ces.2011.09.021.

[15] WEI, Ji-He and YU, Neng-Wen. Mathematical modelling of decarburisation and degassing during vacuum circulation refining process of molten steel: Mathematical Model of the process. Steel Research International, 2002, 73(4), pp. 135–142. DOI 10.1002/srin.200200185.

[16] THUMFART, Maria, ZHANG, Xiaomeng, GRUBER, Christine, WACHLMAYR, Johann, PIRKER, Stefan and RÖSSLER, Roman. Making rh fit for green steel production: A multi-method approach to process monitoring. BHM Berg- und Hüttenmännische Monatshefte, 2025. DOI 10.1007/s00501-025-01593-6.

Hutnické listy – *Metallurgical Journal*
Speciální vydání / Special Issue, roč. / vol. LXXIX
ISSN Online: 3029-8350

# Computational Modelling of Sulfur Removal Mechanisms at the Steel–Slag Interface in Secondary Metallurgy

# Výpočetní modelování mechanismů odsíření na rozhraní ocel–struska v sekundární metalurgii

**Lukáš Fogaraš[1], Slavomír Hubatka[1], Branislav Buľko[1], Peter Demeter[1], Jaroslav Demeter[1], Martina Hrubovčáková[1], Róbert Dzurňák[1], Patrik Fedorko[1], Zuzana Miškovičová[1]**

[1] Technical University of Košice, Faculty of Materials, Metallurgy and Recycling, IMTECH, Slovakia;
*Contact e-mail: lukas.fogaras@tuke.sk

## Abstract

*Achieving the required steel purity and composition relies on effective secondary metallurgy processes, particularly during ladle refining. This study investigates sulfur removal mechanisms at the steel–slag interface using computational modelling. The research focuses on how slag composition and physical behaviour influence desulfurization during ladle treatment. A combination of CFD simulations and thermodynamic analysis was used to explore interfacial transport and reaction phenomena under realistic process conditions. Input data for the simulations were based on operational parameters and chemical compositions obtained from an industrial steelmaking plant. Statistical analysis and multi-parameter modelling were used to define the relationships between key slag properties—such as viscosity, basicity, and interfacial tension—and their influence on sulfur transfer efficiency. CFD simulations realized in Ansys Fluent captured the dynamics of multiphase flow and mass transfer, yielding results that closely reflect observed process trends. The study demonstrates that optimizing slag characteristics and refining parameters can significantly enhance sulfur removal during secondary steelmaking. The findings provide a computational basis for improving process control and refining strategies in industrial practice. By accurately modelling the steel–slag interface, this work supports the development of more effective and predictive tools for optimizing desulfurization in ladle metallurgy.*

***Keywords****: secondary metallurgy, CFD-simulation, steel-slag interface, steel desulfurization, ladle slag*

## Abstrakt

*Dosažení požadované čistoty a chemického složení oceli závisí na účinnosti procesů sekundární metalurgie, zejména během pánvové rafinace. Tato studie se zabývá mechanismy odstraňování síry na rozhraní ocel–struska s využitím numerického modelování. Výzkum je zaměřen na vliv složení strusky a jejích fyzikálních vlastností na průběh odsíření během pánvového zpracování. K analýze transportních a reakčních dějů na rozhraní za realistických procesních podmínek byla použita kombinace CFD simulací a termodynamického modelování. Vstupní data pro simulace vycházela z provozních parametrů a chemického složení získaných z průmyslového provozu. Pro stanovení vztahů mezi klíčovými vlastnostmi strusky – jako jsou viskozita, zásaditost a mezifázové napětí – a jejich vlivem na účinnost přenosu síry byla využita statistická analýza a víceparametrové modelování. CFD simulace realizované v prostředí Ansys Fluent zachycují dynamiku vícefázového proudění a přenosu hmoty a poskytují výsledky v dobré shodě s pozorovanými provozními trendy. Studie ukazuje, že optimalizace vlastností strusky a parametrů rafinace může významně zvýšit účinnost odsíření během sekundární metalurgie. Získané poznatky poskytují výpočetní základ pro zlepšení řízení procesu a návrhu rafinačních strategií v průmyslové praxi. Díky přesnému popisu rozhraní ocel–struska tato práce přispívá k vývoji pokročilých prediktivních nástrojů pro optimalizaci odsíření v pánvové metalurgii.*

***Klíčová slova:*** *sekundární metalurgie, CFD simulace, rozhraní ocel-struska, odsíření oceli, pánvová struska*

Hutnické listy – *Metallurgical Journal*
Speciální vydání / Special Issue, roč. / vol. LXXIX
ISSN Online: 3029-8350

## 1. Introduction

Secondary metallurgy plays a key role in producing high-quality steels by enabling precise control over chemical composition and non-metallic inclusions. Among the most important refining steps is sulfur removal, which is typically carried out in the ladle through reactions at the interface between molten steel and slag. The efficiency of desulfurization depends on several factors, including slag composition, basicity, viscosity, interfacial area, and stirring conditions [1-2].

While empirical approaches remain common in industry, computational modelling has become an increasingly valuable tool for analyzing and optimizing interfacial phenomena in steel refining. Modern CFD tools allow for the simulation of complex multiphase flows, interfacial mass transfer, and chemical reactions under conditions that reflect real ladle metallurgy operations [3-4].

This work presents a computational study of sulfur removal mechanisms occurring at the steel–slag interface using CFD simulations supported by thermodynamic analysis:

- The model incorporates realistic physical and chemical parameters derived from industrial data.
- The aim is to investigate how selected slag properties and operating conditions influence desulfurization efficiency, and to provide quantitative insights for improving ladle refining practice.
- The results contribute to a better understanding of interfacial behavior and support the development of more effective process control strategies in secondary steelmaking [5].

## 2. Materials and Methods

The computational model was developed to simulate sulfur removal at the steel–slag interface during ladle treatment using the CFD software Ansys Fluent 2023R1. A two-phase Eulerian multiphase model was applied to capture the interaction between the molten steel and slag layers, along with argon gas injection from the ladle bottom.

The geometry and mesh corresponded to the dimensions of an industrial ladle used for 170–180 tonnes of liquid steel. The mesh was refined in the interfacial zone to improve the resolution of gradients in velocity, concentration, and turbulence quantities. Turbulence was modeled using the realizable k–ε model with standard wall functions.

**Fig. 1** illustrates the ladle geometry and setup used in the simulation. Input parameters—such as slag composition, temperature, viscosity, basicity, and sulfur content—were based on representative values from actual industrial operations. The species transport model was used to simulate sulfur diffusion and its chemical consumption in the slag phase.

Thermodynamic equilibrium constraints for sulfur partitioning were incorporated through user-defined functions (UDFs), allowing the model to dynamically evaluate local desulfurization rates. Argon flow rates were varied in a parametric study to evaluate their influence on interfacial mass transfer and sulfur removal efficiency.

Hutnické listy – *Metallurgical Journal*
Speciální vydání / Special Issue, roč. / vol. LXXIX
ISSN Online: 3029-8350

| | |
|---|---|
| **Top diameter of the ladle** | 3330 mm |
| **Bottom diameter of the ladle** | 3060 mm |
| **Height of the ladle** | 3700 mm |
| **Height of the steel phase** | 3150 mm |
| **Thickness of the slag layer** | 110 mm |
| **Nozzle diameter for gas injection** | 80 mm |
| **Density of liquid steel** | 7020 kg/m$^3$ |
| **Density of slag** | 3500 kg/m$^3$ |
| **Density of argon** | 0.568 kg/m$^3$ |
| **Viscosity of liquid steel** | 0.0055 Pa.s |
| **Viscosity of slag** | 0.124 Pa.s |
| **Viscosity of argon** | 0.000085Pa.s |
| **Surface tension between steel and slag** | 1.15 N.m |
| **Surface tension between steel and argon** | 1.82 N.m |
| **Surface tension between slag and argon** | 0.58 N.m |

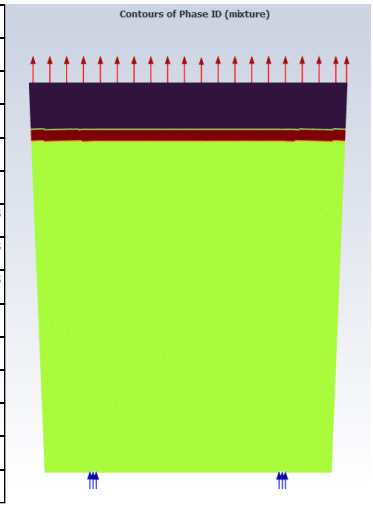


**Fig. 1** Left: Dimensions of the ladle and simulation parameters; right: distribution of individual phases from the bottom view (steel, slag, atmosphere); argon gas inlets for inert media are shown at the bottom

**Obr. 1** Vlevo: Rozměry pánve a parametry simulace; vpravo: rozložení jednotlivých fází při pohledu odspodu (ocel, struska, atmosféra); v dolní části jsou znázorněny přívody argonu pro inertní prostředí

## 3. Results and discussion

The CFD simulations provided detailed insight into the transport phenomena and sulfur removal behavior at the steel–slag interface. The desulfurization process was evaluated under varying argon flow rates (0 to 500 l·min$^{-1}$), while keeping slag composition and steel temperature constant. **Tab. 1** and **Tab. 2** show the input chemical composition of the slag and steel phases.

**Tab. 1** Input chemical composition of ladle slag
**Tab. 1** Vstupní chemické složení pánvové strusky

| CaO [%] | $SiO_2$ [%] | $Al_2O_3$ [%] | MgO [%] | S [%] |
|---|---|---|---|---|
| 54.38 | 3.32 | 36.02 | 5.64 | 0.1550 |

**Tab. 2** Input chemical composition of steel
**Tab. 2** Vstupní chemické složení oceli

| C [%] | Si [%] | Mn [%] | P [%] | S [%] | Al [%] |
|---|---|---|---|---|---|
| 0.0520 | 0.003 | 0.138 | 0.0102 | 0.0077 | 0.338 |

Due to hardware and time constraints, the simulations were performed in a 2D format. The results were recorded in a vertical cross-section located on the left side of the ladle **Fig. 2**, assuming axisymmetric. Based on previously published research, symmetric flow behaviour is expected across both halves of the ladle volume, which justifies the use of a single representative section for analysis.

The computational results were consistent with known theoretical behavior and supported the assumption that both mixing intensity and slag properties strongly influence the desulfurization efficiency. The model provides a valuable basis for future optimization of ladle refining practices using simulation-based approaches.

Hutnické listy – *Metallurgical Journal*
Speciální vydání / Special Issue, roč. / vol. LXXIX
ISSN Online: 3029-8350

**Fig. 2** illustrates the velocity vector field within the steel and slag phases. It can be observed that the injected argon bubbles drive circulation in the steel phase due to momentum exchange. In addition, high turbulent viscosity at the steel–slag interface enhances momentum, heat, and mass transport within the fluid, thereby increasing the turbulent diffusion of species. As a result, species near the steel–slag interface are transported at a higher rate compared to those near the bottom of the ladle.

In the simulation shown in **Fig. 3**, the intensity of steel desulfurization was analysed as a function of argon stirring applied from the bottom of the ladle. Argon flow rates ranged from 0 to 500 L/min. Bottom gas injection significantly accelerated the rate of desulfurization, as confirmed by the curve representing the simulation without gas injection.

The relationship between desulfurization rate and gas flow changes over time, as seen in **Fig. 3**, where the efficiency of sulfur removal decreases around 600 seconds. On the other hand, for argon flow rates ranging from 100 to 500 L/min, there is little to no improvement in desulfurization efficiency, indicating a saturation effect beyond a certain flow rate.

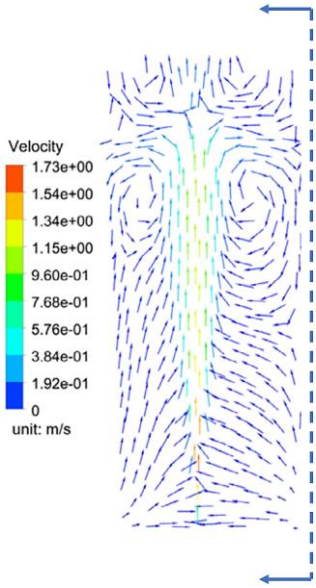


**Fig. 2** Visualization of velocity vector directions within the ladle volume

**Obr. 2** Vizualizace orientací vektorů rychlosti v objemu pánve

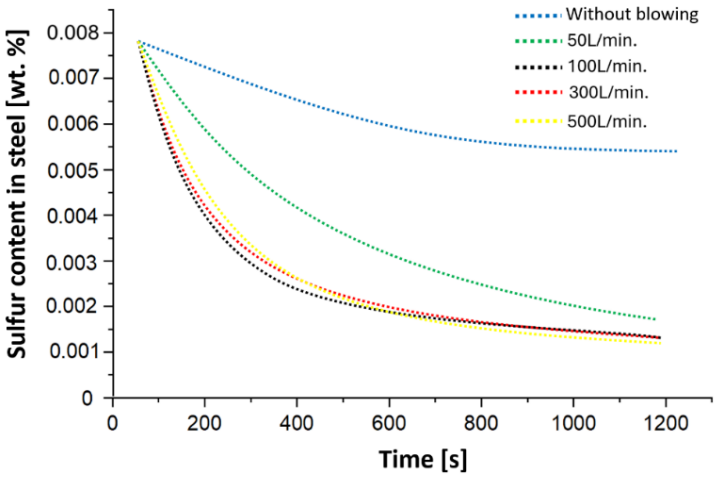


**Fig. 3** Predicted sulfur content in steel at different argon flow rates over time

**Obr. 3** Predikovaný obsah síry v oceli při různých průtocích argonu v průběhu experimentu

As shown in **Fig. 4**, the sulfur content in molten steel decreased over time, with the rate of desulfurization increasing significantly at higher argon flow rates (150 L/min. at this simulation). Enhanced stirring promoted better contact between the steel and slag phases, increasing the interfacial area and accelerating mass transfer.

The simulation results confirmed that argon injection is a key parameter for improving desulfurization kinetics.

Hutnické listy – *Metallurgical Journal*
Speciální vydání / Special Issue, roč. / vol. LXXIX
ISSN Online: 3029-8350

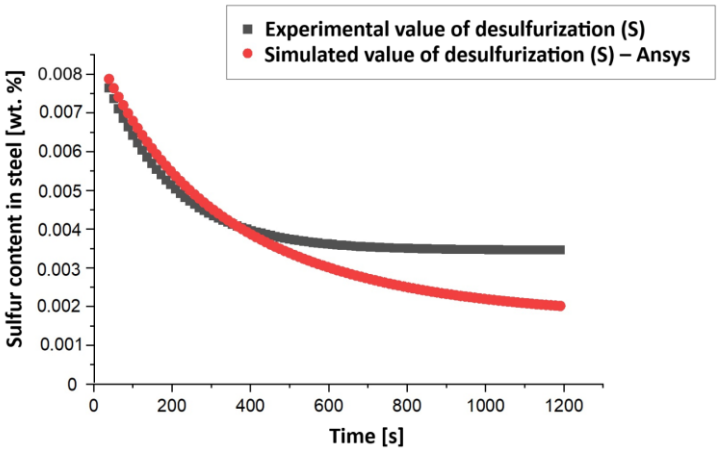


**Fig. 4** Desulfurization progress of steel: computational model vs. predicted experimental values

**Obr. 4** Průběh odsíření oceli: výpočetní model versus predikované experimentální hodnoty

## 4. Conclusion

This study demonstrated the applicability of CFD modelling for analysing sulfur removal mechanisms at the steel–slag interface during ladle refining. The simulations provided valuable insight into the effects of argon stirring and slag properties on the overall desulfurization efficiency. The results showed that bottom gas injection significantly enhances interfacial mass transfer by increasing mixing intensity and expanding the active reaction area. However, the effectiveness of desulfurization does not increase proportionally with gas flow beyond a certain threshold, indicating diminishing returns. High turbulent viscosity at the interface was found to be a key factor in promoting momentum and species transport.

The developed model, based on industrially relevant input data and validated physical assumptions, successfully captured the dominant transport and reaction phenomena in the ladle. It serves as a useful tool for evaluating process conditions and optimizing refining strategies in secondary metallurgy. Future work may include the transition to fully three-dimensional simulations and the integration of more complex thermodynamic and kinetic sub models to further improve the predictive accuracy of the computational approach.

### Acknowledgements

***Research was realised and funded from project „Smart-Steel: AI-Driven control models for future steel production“ No.: 09I05-03-V02-00016 under 09I05-03-V02 – Call for support of research projects focused on the digitalization of the economy at TRL levels 1–3.***

### References

[1] MAO, Congshan, et al. CFD modelling of steel desulfurisation in a gas-stirred ladle. Ironmaking & Steelmaking, 2023, 50.11: 1539-1550.
[2] Tomáš Goč, Bc., Košice 2015, Optimalizácia odsírenia pomocou CaSi a CaO na MPO: diplomová práca, Košice. TUKE. 59 p.
[3] LOU, Wentao; ZHU, Miaoyong. Numerical simulation of slag-metal reactions and desulfurization efficiency in gas-stirred ladles with different thermodynamics and kinetics. ISIJ International, 2015, 55.5: 961-969.
[4] LIU, Yu, et al. A review of physical and numerical approaches for the study of gas stirring in ladle metallurgy. Metallurgical and Materials Transactions B, 2019, 50.1: 555-577.
[5] ANDERSSON, Margareta, et al. Slag-metal reactions during ladle treatment with focus on desulphurisation. Ironmaking & steelmaking, 2002, 29.3: 224-232.

Hutnické listy – *Metallurgical Journal*
Speciální vydání / Special Issue, roč. / vol. LXXIX
ISSN Online: 3029-8350

# Physicochemical Modelling of ESR Ingot Composition Changes

# Fyzikálně-chemické modelování změn složení elektro-struskově přetavených ingotů

**Ganna Stovpchenko[1,2], Liudmyla Lisova[3], Lev Medovar[2]**

[1] Tianjin Heavy Industries Research and Development Co, Ltd, Tianjin, China, 300457;
*Corresponding author: anna_stovpchenko@ukr.net
[2] The Ukrainian State University of Science and Technologies, Dnipro, Ukraine, 49010
[3] Z.I. Nekrasov Iron & Steel Institute NASU, Dnipro, Ukraine, 49107

## Abstract

*Electroslag remelting (ESR) is an essential technological step for producing the highest-quality steel and alloys. Today, ESR is seen as a tool to enhance ingot structure, homogeneity, and yield, rather than just refining metal from sulphur and non-metallic inclusions, since the electrode has already passed through refining and deep degassing during primary melting and ladle treatment. Nevertheless, fluoride-oxide slag is a crucial part of the process, and its interaction with metal occurs throughout the whole remelting duration. Though ESR slag contains stable oxides mainly, it can still oxidize key elements in steel and alloys, especially oxygen-active elements (aluminium, titanium, and silicon). Our perspective on the additive nature of the ESR process in a protective atmosphere led to a better understanding of the drastic growth of slag-to-metal mass ratios during remelting, giving the ability to make a prognosis of changes in slag and metal composition. Dividing the entire process into subsystems enables forecasting the composition at a specific point in the process, at a relevant height of the ESR ingot. The results of thermodynamic modelling are valuable for improving ESR technology and selecting the most suitable slag composition from the existing palette or customizing the slag for a specific alloy.*

***Keywords**: electroslag remelting, thermodynamic modelling, dynamics, gas-slag-metal interaction*

## Abstrakt

*Elektrostruskové přetavování (ESR) představuje klíčový technologický krok při výrobě ocelí a slitin nejvyšší kvality. V současnosti je ESR vnímáno spíše jako nástroj ke zlepšení struktury, homogenity a výtěžnosti ingotů než pouze jako proces rafinace kovu od síry a nekovových vměstků, jelikož elektroda již prošla rafinací a hloubkovým odplyněním během primárního tavení a pánvového zpracování. Fluoridovo-oxidová struska je nicméně klíčovou součástí procesu a její interakce s kovem probíhá po celou dobu přetavování. Ačkoli struska ESR obsahuje převážně stabilní oxidy, může stále docházet k oxidaci klíčových prvků v oceli a slitinách, zejména prvků s vysokou afinitou ke kyslíku (hliník, titan a křemík). Pohled na aditivní povahu procesu ESR v ochranné atmosféře vedl k lepšímu pochopení výrazného nárůstu poměru hmotnosti strusky ke kovu během přetavování, což umožňuje predikci změn ve složení strusky i kovu. Rozdělení celého procesu na subsystémy umožňuje předpovídat složení v konkrétním bodě procesu, odpovídajícím určité výšce ESR ingotu. Výsledky termodynamického modelování představují cenný nástroj pro zlepšení technologie ESR a pro výběr nejvhodnějšího složení strusky z dostupné palety, případně pro její optimalizaci pro konkrétní slitinu.*

***Klíčová slova:** elektrostruskové přetavování, termodynamické modelování, dynamika, interakce plyn-struska-kov*

Hutnické listy – *Metallurgical Journal*
Speciální vydání / Special Issue, roč. / vol. LXXIX
ISSN Online: 3029-8350

## 1. Introduction

Electroslag remelting (**Fig. 1**) is an arc-less, drop-mode melting process of a consumable electrode that is immersed in a layer of electrically conductive slag with sufficiently high resistance (much greater than that of other circuit components - the electrode, molten slag, liquid metal pool, solidified ingot, bottom plate, high current loop and transformer).

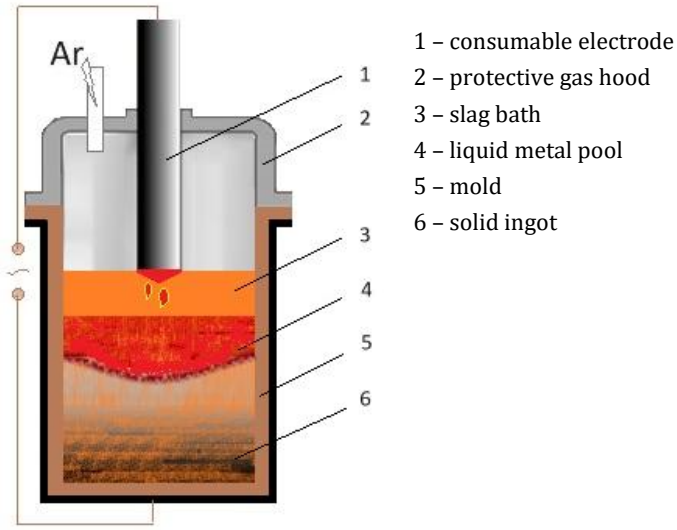


**Fig. 1** Simplified diagram of the ESR in argon protective atmosphere

**Obr. 1** Zjednodušené schéma ESR v ochranné atmosféře argonu

The passage of electric current through the slag generates heat, which powers the melting process. Drops fall through a refining slag layer, forming a molten metal bath, solidifying within a copper water-cooled mould into a dense, low-defect ingot. Slag properties are crucial for both generating heat (ESR process thermal efficacy), maintaining the metal bath's composition maximally close to the initial composition of the consumable electrode (except for absorbing non-metallic inclusions), solidification conditions (temperature regimes), and smooth ingot surface formation.

The slow rate of metal supply from the consumable electrode through the slag layer, which acts as both an electric heater and thermal buffer, leads to a shallow liquid metal pool. Permanently renewal of liquid metal pool by drops coming from consumable electrode helps sufficiently reduce segregation, the slow melting rate and high-gradient solidification in the copper water-cooled mould provide a minimal (in comparison to cast forging ingots or continuously cast billets of the same diameter) volume of the simultaneously solidifying liquid metal bath and mushy zone. This is a reason for worldwide recognition of "ESR quality of ingot" featuring a dense dendritic structure, no shrinkage, and a smooth side surface, ensuring high product yield. Thus, effective ESR technology necessitates a slag engineering that balances chemical inertness and optimal physical properties (melting temperature interval, electrical conductivity, viscosity, etc.).

This article aims to explain the changes in the physicochemical conditions that occur during the remelting of consumable electrodes in a protective gas atmosphere using a single slag introduced at the beginning of the process because of the drastic reduction of slag-to-metal ratio.

Hutnické listy – *Metallurgical Journal*
Speciální vydání / Special Issue, roč. / vol. LXXIX
ISSN Online: 3029-8350

## 2. Physicochemical Features of the Electroslag Remelting Process

From a physicochemical point of view, the electroslag remelting process has several characteristic features in comparison to batch-type melting processes of traditional steelmaking (in electric arc and basic oxygen furnaces (EAF and BOF) and ladle treatment (ladle furnace and vacuum degassing) as well as to usual forging ingot or continuous casting.

The primary distinction is that ESR is a melting, refining, and casting process simultaneously. Two opposite processes in their nature and favourable conditions—melting and solidification—occur at the same time in a copper water-cooled mold. The positive for melting/refining is that no metal contamination by refractories, and a well-developed surface of interaction between slag and metal. Unfavourable conditions for melting—resistive-type heating and intensive cooling—cause ESR's low energy efficiency. The positive is that metal comes slowly, and the liquid metal pool is permanently renewed. Intensive heat inflows from the melting zone compromise the solidification rate and cause uneven temperature distribution on the vertical axis. However, heat outflows to intensively cooled mold surface is the sourse of high temperature gradient at solidification, providing a dense dendrite structure of the EAR ingot. The most heat is generated at the contact surface between the resistive slag bath and the consumable electrode side surface and tip, forming a liquid metal film that drips due to gravity; temperature gradually decrease from hot area of a slag bath (variation along vertical axis in slag bath can reach 200 K to a metal pool surface and further away to its bottom end, where the ESR ingot forms under the cooling action of the copper water-cooled mould.

There are three contact surfaces between slag and metal (liquid film on the tip of the consumable electrode, metal drops sinking through the slag bath, and the contact surface between the liquid slag bath and liquid metal pool). The formation and movement of metal droplets constantly refresh all interfaces. Different estimations of their geometrical and residence time parameters and relative shares in the refining exist, but all authors agree that the total metal-slag interaction surface is highly developed. The high temperatures of the melts (1900-2100K) and the extensive surface of slag-metal interactions bring the reactions closer to equilibrium that allows the use of thermodynamics.

Several other features of the electroslag remelting of a consumable electrode are essential to understanding the core of ESR ingot formation, which were put as the base in the physicochemical modelling of changes in gas-slag-metal system composition during ingot Electroslag Remelting. The liquid metal has no direct contact with an atmosphere, as the slag bath separates them. Gaseous phase emissions from slag-metal reactions and evaporative processes from the slag are expelled into the furnace atmosphere, which undergoes gradual replenishment. The gaseous environment above the slag bath does not engage directly with the molten metal, but the electrode surface oxidizes in the presence of oxygen.

An oxygen-free atmosphere—mainly argon or nitrogen (depending on the steel grade)—effectively mitigates this issue by blocking oxygen activity in the slag and its transmission to the metal. For this reason, modern ESR facilities typically employ a closed hood that encloses the entire electrode to sustain a protective gaseous atmosphere. The solid metal of a consumable electrode doesn't participate in the slag-metal interaction before it melts. Liquid metal pool incrementally solidifies at its bottom, and an ingot exits the reaction zone after interacting with the slag, and the forming products of reactions of metal components interacting with slag are permanently removed. In contrast, molten slag continues refining processes, assimilating slag-metal interaction products and non-metallic inclusions from the electrode.

Hutnické listy – *Metallurgical Journal*
Speciální vydání / Special Issue, roč. / vol. LXXIX
ISSN Online: 3029-8350

Often, ESR involves charging the entire slag mass at the start of the remelting process, without adding premelted slag or its components. The solidified ingot metal composition changes along its height because slag-to-metal ratio permanently reduces from very high values at the beginning of the remelting to a so-called "slag consumption" value (20-50 kg per ton). In this case, the slag bath composition changes due to the accumulation of reaction products between slag and metal and losses on evaporation in the gas phase. From this perspective, the technology involving the continuous addition of slag for its refreshment and compensation losses for slag skin formation partially mitigates changes in slag composition. Nevertheless, even at fresh slag additions, the slag-to-metal ratio drastically varies throughout the electroslag remelting process. Unsurprisingly, a lasting change and substantial shift in the slag-metal mass ratio (**Fig. 2**) lead to vastly different conditions for slag-metal interaction during electroslag remelting.

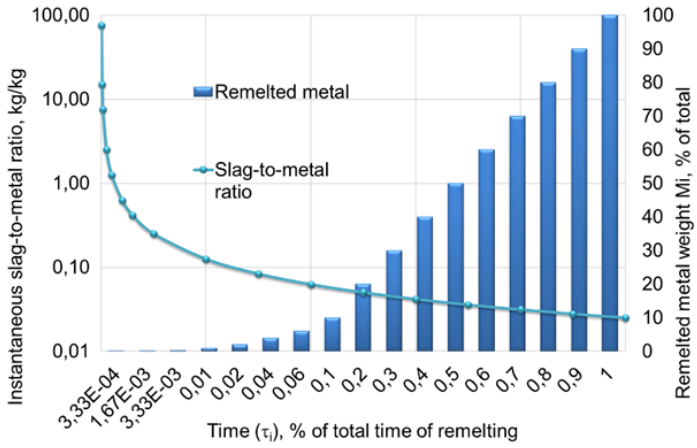


**Fig. 2** Timeline of slag-to-metal ratio at appropriate mass of remelted metal at ESR ingot remelting when a whole slag consumption makes 25 kg/ton of metal

**Obr. 2** Změna poměru struka-kov v čase při odpovídající hmotnosti přetaveného kovu pomocí ESR, kdy celková spotřeba strusky činí 25 kg/t kovu

The diagram provides a summary and demonstration of the characteristics inherent in the physical and chemical processes that transpire during electroslag remelting. The variations in the slag-to-metal ratio are illustrated for a designated slag consumption of 25 kg/t of metal. This uncovered trend is general, regardless of the specific value of slag consumption. Specific slag consumption typically ranges from 20 to 40 kg per ton, with the higher **Fig. 2** often used for thermodynamic calculations of the ESR, providing just a very average result. However, due to the considerable slag-to-metal ratio in the initial minutes of remelting, the oxygen-bearing slag oxidizes the metal most significantly at the start of the process. This effect cannot be overlooked as the oxidative influence of slag remains significant for quite a long time and can cause ingot inhomogeneity along its height.

Changes in a slag's physical properties, such as viscosity, electrical conductivity, and surface tension, are just as significant. They need to be tested to see if they meet the requirements for an efficient ESR process. It's also crucial to uncover deeper connections between experimentally measured values and chemical composition using atomistic approaches. This allows for predicting the physical properties of molten slag, making it easier to select the right slag. The Directed Chemical Bonds Concept, created by Prof. E. Prikhodko and further developed by his team at the Z. I. Nekrasov Institute of Ferrous Metallurgy of the NASU [10], demonstrates promising results for these purposes.

Hutnické listy – *Metallurgical Journal*
Speciální vydání / Special Issue, roč. / vol. LXXIX
ISSN Online: 3029-8350

## 3. Methodology for Modelling Changes in ESR Ingot and Slag Compositions over Time

Analysing the additive nature of the ESR process in a protective atmosphere, the authors provided insights enables developing a procedure for slag-metal interaction modelling during the ESR (**Fig. 3**).

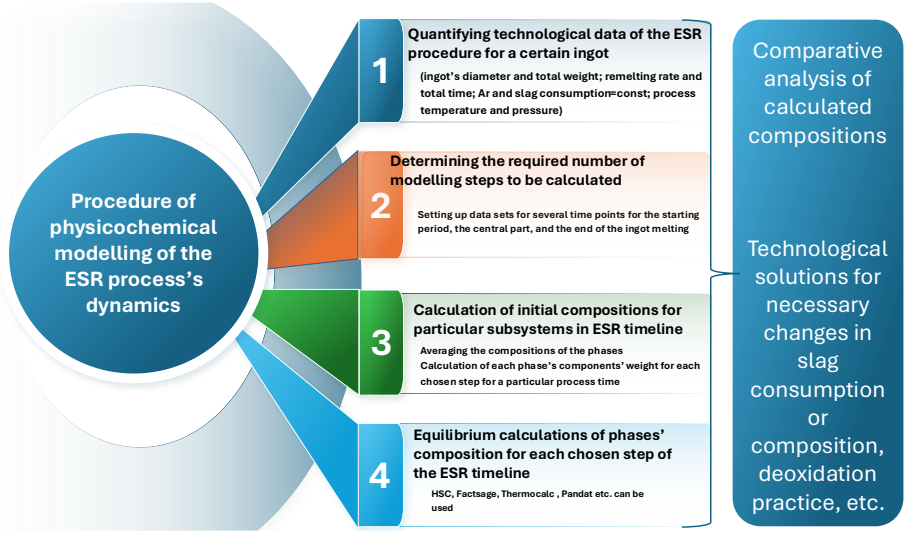


**Fig. 3** Procedure of the gas-slag-metal interaction modelling during electroslag remelting

**Obr. 3** Postup modelování interakce plyn–struska–kov při elektrostruskovém přetavování

At first, the technological data of certain ESR ingot manufacturing should be collected. For example, the dynamic ESR model demonstration system comprised 300 kg of slag, 6,47 kg of argon atmosphere, and a part of the total ingot mass (19,000 kg) of 1000 mm in diameter, corresponding to a particular time interval. The metal mass and slag-to-metal ratio during remelting were derived from a melting rate of 14.2 kg/min, obtained from ESR practices for similar ingots.

The second stage evaluates the number of modelling steps required to address this task. Based on the chosen purposes, appropriate time intervals (i) should be established. The most reasonable approach is to combine the calculated subsystems with an actual probe of the ingot. The beginning of remelting is interesting due to the highest slag-to-metal ratio. However, this ingot portion will be discarded, prompting calculations of higher ingot horizons.

After averaging the compositions of the gas-slag-metal phases, the calculation of the weight of each phase's components for each chosen moment in a specific process should be performed, forming the line of proper subsystems. The input data is the mass of metal remelted at a specific time (i), considering the melting rate, total mass of slag, and argon volume in the ESR plant's closed chamber. For each designated time, develop a subsystem with the total masses of slag, gas, and the instantaneous mass of molten metal that will be used as initial data in software for equilibrium composition calculation. In all subsystems, the remelted metal mass is a variable (mi), while the primary masses of slag and gas phases remain constant.

Thermodynamic calculations of the equilibrium state of the "gas-slag-metal" system, using CALPHAD methodology can be done using HSC Chemistry, Pandat, ThermoCalc, and similar software. In the presented examples, thermodynamic calculations for the "gas-slag-metal" system were performed using HSC Chemistry software [2].

Hutnické listy – *Metallurgical Journal*
Speciální vydání / Special Issue, roč. / vol. LXXIX
ISSN Online: 3029-8350

The comparative analysis of primary mass data from subsystems and equilibrium calculations enables recognizing changes in the masses and compositions of phases. The primary advantage of the proposed approach to modelling probable changes in ingot composition along its height is that it enables the prediction of changes in gas-slag-metal interaction conditions.

The main limitation is its time-consuming nature, making it impractical when changes in ingot composition are not critical. Nevertheless, this approach assists in identifying suitable technological solutions for necessary changes in slag consumption or composition, deoxidation practices, and so on.

## 4. Outcomes of Slag-Metal Interaction Prediction in the Course of Electroslag Remelting

Changes in metal composition were calculated according to the proposed procedure of physicochemical modelling of the ESR for slag $34CaF_2/30Al_2O_3/27CaO/0.5SiO_2/2.5MgO/6TiO_2$ and superalloy Inconel 718 at 1873 K (**Tab. 1**).

**Tab. 1** The chemical composition of the Inconel 718 used in the calculation
**Tab. 1** Chemické složení slitiny Inconel 718 použití v rámci výpočtu

| Elements content, %wt. | | | | | | | | |
|---|---|---|---|---|---|---|---|---|
| Ni | Cr | Fe | Nb | Mo | Ti | Al | C | B |
| 53.7 | 18.2 | 18.2 | 5.4 | 3 | 1 | 0.5 | 0.03 | 0.004 |

The equilibrium contents of the most oxidisable elements in the metal and the matching slag-to-metal ratio for a specific time for seven subsystems are shown as points on the curves of **Fig. 4**.

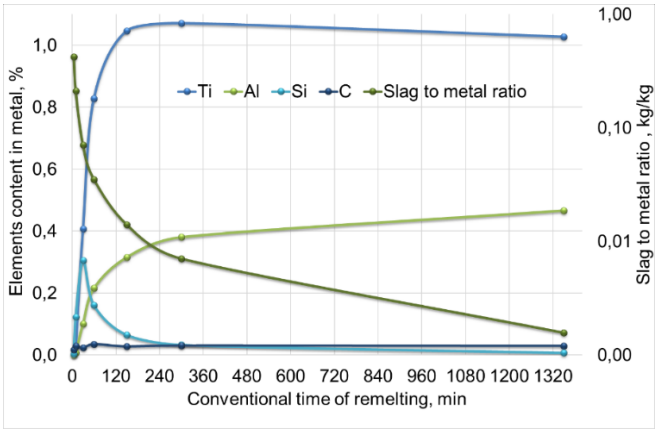


**Fig. 4** Equilibrium content of active-to-oxygen elements in the metal phase and slag to metal ratio at Inconel 718 remelting with slag $34CaF_2$-$30Al_2O_3$-27CaO-$0.5SiO_2$-$2.5MgO$-$6TiO_2$

**Obr. 4** Rovnovážný obsah prvků aktivních vůči kyslíku v kovové fázi a poměr strusky ke kovu při přetavování slitiny Inconel 718 se struskou $34CaF_2$–$30Al_2O_3$–27CaO–$0{,}5SiO_2$–$2{,}5MgO$–$6TiO_2$

The slag-metal mass ratio at the fifth minute of remelting is approximately 42 kg/kg and decreases to 0.016 kg/kg by the end of the melt. It is clearly visible that the system is most reactive when the slag-to-metal ratio is very high at the beginning of the remelting process. Consequently, the oxidation action of the slag significantly impacts the content of elements that react with oxygen at this period. The content of active elements critical for alloy properties (Ti, Al) in the initial stages of the process (first 60 minutes) is nearly zero. The weighty changes of the elements content occur within two hours, while the mass losses of metal and the gains in slag primarily occur (**Fig. 5**).

Hutnické listy – *Metallurgical Journal*
Speciální vydání / Special Issue, roč. / vol. LXXIX
ISSN Online: 3029-8350

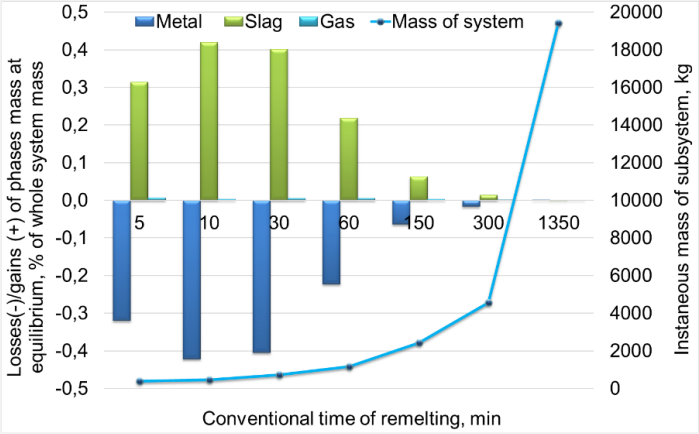


**Fig. 5** Phase losses/gains in the reactive subsystems during the ESR in argon atmosphere

**Obr. 5** Úbytky a přírůstky jednotlivých fází v reaktivních subsystémech během ESR v argonové atmosféře

The slag-metal mass ratio at the fifth minute of remelting is approximately 42 kg/kg and decreases to 0.016 kg/kg by the melt end. It is clearly visible that the system is most reactive when the slag-to-metal ratio is very high at the beginning of the remelting process. Consequently, the oxidation action of the slag significantly impacts the content of elements that react with oxygen at this period. The content of active elements critical for alloy properties (Ti, Al) in the initial stages of the process (first 60 minutes) is nearly zero. The weighty changes of the elements content occur within two hours, while the mass losses of metal and the gains in slag primarily occur (**Fig. 5**).

After that period, relative losses of equilibrium metal phase mass diminish as the metal phase begins to be bigger (and the slag-to-metal ratio decreases) beyond critical values. This moment marks the depletion of the slag's oxidative capacity. However, exchange reactions between slag and metal phases continue. As shown in **Fig. 4**, titanium content increases for up to four hours. Although it slightly decreases over time, it remains higher than the initial value.

The aluminium content rises until the end of the remelting process, but does not reach the initial level because of a reduction in silicon from the slag, which occurs most actively during the first few minutes. At the beginning of the process, the silicon content peaks and then decreases over more than two hours of remelting, remaining in the metal until the end of the melt. The carbon content in the metal shifts by 0.01-0.02% from the initial value during the period of metal losses. Therefore, calculations based on the developed dynamic model of gas-slag-metal interaction during the ESR process in a protective atmosphere indicate that even in an inert gas environment, changes in the content of oxygen-active elements in the metal phase occur, resulting in inhomogeneity of their distribution along the height of the ingot.

## 5. Exploring the Opportunities and Limitations of Electroslag Remelted Ingot Composition Modelling in Dynamics

Our view on how ESR ingot composition forms diverge from traditional physicochemical calculations commonly used to estimate ESR ingot composition. By modelling this process as a series of subsystems, we can gain a clearer understanding of the ESR ingot formation pattern and predict changes in slag-metal interaction during the process.

Hutnické listy – *Metallurgical Journal*
Speciální vydání / Special Issue, roč. / vol. LXXIX
ISSN Online: 3029-8350

The simpler single-system approach of thermodynamic calculations for the stable stage of electroslag remelting in argon is also useful for comparing different slags under the same process conditions (same ingot, melting rate, and temperature) or as a preliminary estimate. Calculations conducted using both the physicochemical modelling of the ESR process dynamics with various subsystems and a single-system approach indicate that even with neutral gas and oxide-fluoride slags, gas-slag-metal interaction leads to alterations in the content of active-to-oxygen elements such as titanium, aluminum, silicon, and others. The intensity of changes in chemical composition is highest at higher slag-to-metal ratios. occurring at the beginning of the process and continually decreases throughout the process to the level of specific slag consumption typically used for thermodynamic estimation of the ESR.

The chemical composition of phases changes due to oxidation-reduction reactions. Additionally, slag's ability to desulphurise metal and assimilate non-metallic inclusions gradually decreases during the ESR process. A slag bath accumulates products of chemical interactions between metal and slag, altering its chemical and physical properties, which are vital for process stability and ingot quality. The slag is inert to metal when no or very minor oxidation occurs, and it is usually the goal for ingot quality and technological operations. For such slags (with low content of stable oxides or fluorides only), the thermodynamic calculations show no changes outside the permissible range in the chemical composition of phases. Any additions (deoxidizing or alloying materials) can be made only into a slag bath that reduces the precision of resulting changes in the liquid metal pool compositions due to difficulties in control and adjustment, as the final composition can be verified only in a solidified ingot. Thus, an ingot primarily inherits the composition of the consumable electrode. When changes are significant, the composition of a consumable electrode should be adjusted, or slag should be changed for a less reactive one, or, in relatively rare cases, metal alloying through the slag should be envisaged, requiring additional calculations.

One significant benefit of ESR dynamics modelling is its ability to predict and account for factors that influence the metal composition along the height of the ESR ingot or respond to them accordingly. This analysis can be applied in various contexts, depending on the research's purpose (e.g., shifts in the content of active components in the system).

Summarising, the predictive physicochemical model of ESR ingot formation in dynamics can be used to achieve several goals:

- tailoring existing compositions or searching for new slag for specific alloys. For example, a new slag composition could replace the high $CaF_2$ content in the ESR of alloyed and high-alloyed steels in both stationary and short-collar molds. The industrial tests conducted on the developed slag have shown the following benefits: oxide inclusion content was reduced by 0.5 points, and power consumption decreased by 17%. A more environmentally friendly option was developed, featuring less than half the calcium fluoride content at a lower cost of 23-25%. [3, 9];
- maintaining the active components content (Ti, Al, etc.) at high-alloyed steels and alloys while remelting [11] and a low level of oxygen in steel during ESR [4, 7];
- development of slags with specific properties, like self-disintegrating slag [8];
- development of slags for new steels and alloys (AHSS, superalloys, etc.) remelting [1, 5, 6].

Overall, the proposed physicochemical modelling for the ESR process in the new paradigm could serve as an effective tool for predicting how slag composition impacts the homogeneity of an ingot's height and the yield of a suitable metal.

Hutnické listy – *Metallurgical Journal*
Speciální vydání / Special Issue, roč. / vol. LXXIX
ISSN Online: 3029-8350

Such predictions are crucial in the manufacturing of high-alloy steels and alloys through electroslag remelting. Uncontrolled changes in slag composition during remelting can lead to the scrapping of ESR ingots, which can weigh up to 250 tons. Moreover, the situation worsens when minor changes are overlooked, placing critical parts at risk of damage when the product is put into use.

## 6. Conclusion

A significant diminishing of the slag-to-metal mass ratios from the beginning to the end of an ingot formation is typical for electroslag remelting with a constant slag mass charged at the start of the process, and a gradually increasing remelted metal mass. Adding fresh slag during remelting can partially compensate for slag skin formation losses and keep the slag-to-metal mass ratio more stable, but the overall slag capacity for altering metal composition increases.

The proposed procedure of ESR ingot formation in dynamics shows promise for studying the changes in composition along the ingot's height caused by slag action during the process.

For the ESR process in an inert atmosphere, knowing the slag metal ratio at a particular moment of the electroslag remelting allows building the line of gas-metal-slag subsystems to calculate equilibrium compositions and predict changes in slag and ingot metal compositions. It was shown that fluoride-oxide ESR slags are not entirely neutral to metal and can oxidise steel and alloys (primarily active alloying elements like aluminium, titanium, and silicon) due to chemical reactions between slag and metal. The highest intensity of chemical composition changes occurs at the higher slag-to-metal ratio, which is at the start of the process and permanently reduces to the value of a specific slag consumption at its end.

This makes it possible to predict the composition along the height of the ESR ingot and increases the yield of suitable metal. Predicting slag and metal composition changes at a particular moment has practical value and can be used for technology improvement. This also paves the way for creating tailored slags for specific alloy compositions, where homogeneity is essential for quality.

## References

[1] Davidchenko, S. et al. (2017) 'Potentials of the Acid Slag for ESR', The Proceedings of the Liquid Metal Processing & Casting Conference 2017, Ed. by: Krane, M. et al. 10-13 Sept.2017, Philadelphia (PA, USA), TMS, pp. 145–148.
[2] HSC Chemistry 10 (2023), https://www.metso.com/portfolio/hsc-chemistry/
[3] Lisova, L. et al. (2020) 'Thermodynamics of interactions and physical properties of slags of $30CaF_2/30CaO/30Al_2O_3$ ($SiO_2$, MgO) system at electroslag remelting,' *Sovremennaja Èlektrometallurgija*, 2020(1), pp. 8–13. https://doi.org/10.37434/sem2020.01.01.
[4] Medovar, L.B., et al. (2023a) 'Electroslag hollow ingots for nuclear and petrochemical pressure vessels and pipes,' *Metals*, 13(7), p. 1290. https://doi.org/10.3390/met13071290.
[5] Medovar, L.B. et al. (2023b) 'Features and Restrictions of Electroslag Remelting with Silica-Bearing Slags for Lightweight High Manganese Steel,' *Steel Research International,* 94(11). https://doi.org/10.1002/srin.20230016.
[6] Stovpchenko, G., Gusiev, I. and Medovar, L. (2014) 'Features of Slag-Metal interaction at electroslag remelting of superalloys,' 8th International Symposium on Superalloy 718 and Derivatives, pp. 47–56. https://doi.org/10.1002/9781119016854.ch4.
[7] Stovpchenko, G. et al. (2018a) 'Physico-chemical properties of the ESR slags system CaF2-Al2O3-(MgO, TiO2),' *Journal of Achievements in Materials and Manufacturing Engineering*, 2(89), pp. 64–72. https://doi.org/10.5604/01.3001.0012.7110.
[8] Stovpchenko, G., Medovar, L.B., et al. (2018b) 'Self-disintegrating slag for electroslag remelting of hollow ingot,' *Ironmaking & Steelmaking*, 46(8), pp. 782–788. https://doi.org/10.1080/03019233.2018.1428418.
[9] Stovpchenko, G., Davidchenko, S.V., et al. (2020) 'Investigation of manufacturability and effectiveness of the new slag for electroslag remelting,' *Sovremennaâ Èlektrometallurgiâ*, 2020(3), pp. 11–17. https://doi.org/10.37434/sem2020.03.01.
[10] Stovpchenko, G. et al. (2022) 'Predictive models for molten slags viscosity and electrical conductivity based on directed chemical bonds concept,' *Ironmaking & Steelmaking*, 49(6), pp. 572–580. https://doi.org/10.1080/03019233.2022.2026043.
[11] Stovpchenko, G. et al. (2023) 'Thermodynamic and physical properties of $CaF_2$–($AL_2O_3$–$TiO_2$–MgO) system slags for electroslag remelting of Inconel 718 alloy,' *Materials Science*, 58(4), pp. 494–504. https://doi.org/10.1007/s11003-023-00690-6.

Hutnické listy – *Metallurgical Journal*
Speciální vydání / Special Issue, roč. / vol. LXXIX
ISSN Online: 3029-8350

# Flow Under Control: Modelling of Electromagnetic Effects in Continuous Casting

# Řízené proudění: Modelování elektromagnetických účinků při kontinuálním odlévání oceli

**Yahea Ayoub[1], Pavel E. Ramirez Lopez[1,2], Sailesh Kesavan[1], Magnus Gustafsson[3], Christer Nilsson[4]**

[1] Process Metallurgy Department, SWERIM AB, Aronstorpsvagen 1, SE 97 437, Luleå, Sweden. *Contact e-mail: yahea.ayoub@swerim.se
[2] KTH, Royal Institute of Technology, Brinellvägen 23, SE-100 44 Stockholm, Sweden; pavel.ramirez.lopez@swerim.se; pe2@kth.se
[3] Luleå university of technology, Laboratorievägen 14, SE-971 87, Luleå, Sweden; magnus.gustafsson@ltu.se
[4] SSAB EMEA AB, Svartöbrinken 20, SE-974 37, Luleå, Sweden; christer.nilsson@ssab.com

## Abstract

*This work presents a numerical study on the influence of localized electromagnetic braking (EMBr) in thin-slab continuous casting. A coupled model of molten steel flow and electromagnetic fields was developed using ANSYS Fluent with its magnetohydrodynamics (MHD) module. Magnetic field distributions were generated through a MATLAB user-defined function and mapped onto the casting mould. A Box-Behnken experimental design was used to systematically vary five parameters: field intensity, diameter, x- and z-placement, and casting speed, resulting in 41 simulations. Key flow characteristics were monitored, including meniscus velocity, jet behavior, and wall forces. Results show that near-inlet EMBr placement leads to reduced jet velocity, downward deflection, and damping of flow variables. In contrast, fields placed below the jet increase upward flow momentum, meniscus velocity, and steel level. Larger coil diameters and higher magnetic field intensities generally reduce all flow parameters and promote upward jet deflection. Regression models reveal strong nonlinear and interaction effects, particularly between vertical placement, intensity, and diameter. The study demonstrates that EMBr positioning and configuration have significant but complex effects on flow behavior in continuous casting, providing valuable insights for process control and quality improvement in steel production.*

***Keywords**: continuous casting, electromagnetic braking, slab casting, computational model*

## Abstrakt

*Tato práce představuje numerickou studii vlivu lokálního elektromagnetického brzdění (EMBr) při kontinuálním odlévání tenkých pásů. Pomocí programu ANSYS Fluent a jeho modulu magnetohydrodynamiky (MHD) byl vyvinut propojený model proudění roztavené oceli a elektromagnetických polí. Rozložení magnetického pole bylo generováno prostřednictvím uživatelsky definované funkce v MATLABu a promítnuto na odlévací formu. Pro systematickou změnu pěti parametrů – intenzity pole, průměru cívky, polohy v osách x a z a rychlosti odlévání – byl použit experimentální design Box-Behnken, což vedlo k realizaci 41 simulací. Sledovány byly klíčové charakteristiky proudění, včetně rychlosti menisku, chování proudu a sil působících na stěny formy. Výsledky ukazují, že umístění EMBr v blízkosti vstupu snižuje rychlost proudu, způsobuje jeho odklon směrem dolů a tlumí jeho proměnné. Naopak pole umístěná pod proudem zvyšují hybnost proudu směrem nahoru, rychlost menisku a hladinu oceli. Větší průměry cívek a vyšší intenzity magnetické pole obecně snižují všechny parametry proudění a podporují odklon proudu směrem nahoru. Regresní modely odhalují silné nelineární a interakční účinky, zejména mezi vertikálním umístěním, intenzitou a průměrem cívky. Studie ukazuje, že umístění a konfigurace EMBr mají významné a komplexní dopady na chování proudění při plynulém odlévání, což poskytuje cenné poznatky pro řízení procesu a zlepšení kvality výroby oceli.*

***Klíčová slova:** plynulé lití, elektromagnetická brzda, odlévání bram, výpočetní model*

Hutnické listy – *Metallurgical Journal*
Speciální vydání / Special Issue, roč. / vol. LXXIX
ISSN Online: 3029-8350

## 1. Introduction

Steel is primarily produced via two methods: the blast furnace route and the electric arc furnace process. Regardless of the chosen production route, both methods typically culminate in a shared final step, continuous casting. In this stage, molten steel is continuously poured into a water-cooled mould where it solidifies into semi-finished forms, such as slabs. [3] Since the invention of continuous casting in the 19th century, a variety of control techniques have been developed, aimed at optimizing process parameters to prevent severe defects like breakouts.

One such control strategy is local electromagnetic braking (EMBr), which aims to stabilize the flow field within the mould, thereby indirectly enhancing thermal uniformity and solidification quality. As described by [5], the local EMBr system typically features circular electromagnetic coils arranged perpendicular to the mould surface. When connected to a direct current (DC) source, these coils generate a static magnetic field that penetrates the molten steel within the mould as shown in **Fig. 1**. The primary function of the local EMBr is to reduce the velocity of the impinging jet from the submerged entry nozzle (SEN), promoting a more stable and controlled flow within the mould.

The paper pursues two main objectives:

- To develop a numerical model capable of coupling molten steel flow with electromagnetic fields within a thin-slab continuous casting mould.
- To utilize this model in conducting a systematic parametric study aimed at characterizing the influence of local electromagnetic braking on mould flow behaviour.

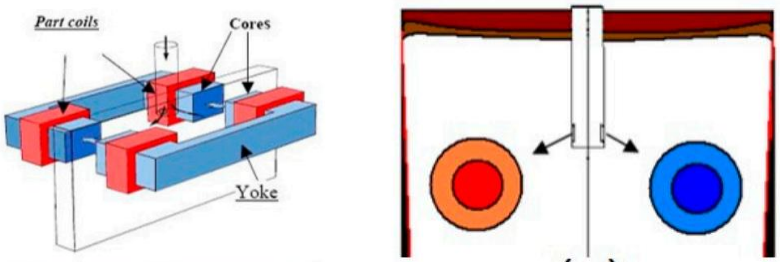


**Fig. 1** An illustration of Local EMBr, according to [5]

**Obr. 1** Ilustrace lokálního EMBr dle [5]

## 2. Method

To meet the objectives of this study, a numerical model of a thin-slab continuous casting mould was developed using ANSYS software. The geometry, depicted in **Fig. 2(a)**, was created in *ANSYS SpaceClaim* based on typical industrial dimensions for thin-slab caster. To enable a large number of simulations runs, the model was intentionally simplified to reduce computational cost.

The computational mesh, shown in **Fig. 2(b)**, was generated using *ANSYS Meshing*, while the flow and thermal simulations were configured in *ANSYS Fluent*. The model was further coupled with electromagnetic fields using Fluent's Magnetohydrodynamics (MHD) module, specifically through the induction equation method for simulating field-flow interaction.

Hutnické listy – *Metallurgical Journal*
Speciální vydání / Special Issue, roč. / vol. LXXIX
ISSN Online: 3029-8350

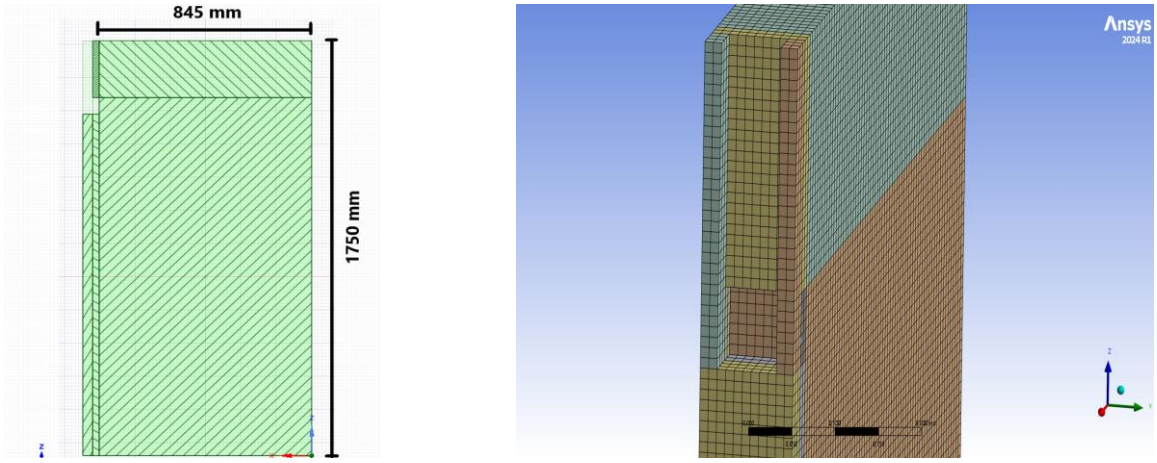


(a) (b)

**Fig. 2** Model geometry and mesh-grid. A longitudinal cross section at y = 0.055 m [left]. A 3D view of the mesh-grid [right]

**Obr. 2** Geometrie modelu a síť. Podélný řez v bodě y = 0,055 m [vlevo]. 3D pohled na síť [vpravo]

Three reference flow cases were simulated with three different casting speeds: 2,4 and 6 m/min, as illustrated in **Fig. 3**. The resulting jet trajectories were extracted and imported into *MATLAB*, as shown in **Fig. 4**, to guide the accurate placement of the magnetic field relative to the jet path. The magnetic field distributions were generated in *MATLAB* using a user-defined function (UDF) that allowed control over the field's intensity, shape, and location. The resulting data was exported as a .mag file, compatible with *ANSYS Fluent*, following the procedure outlined in the *ANSYS MHD Manual* [2].

A range of magnetic field configurations were applied to the fully developed flow fields, and the resulting jet behavior was monitored to systematically assess the influence of electromagnetic braking. The simulations were conducted using a transient model with a time step of 0.1 seconds. To account for the complex flow characteristics within the mould, turbulence was modeled using the standard $k$–$\varepsilon$ model with standard wall functions, while multiphase flow was captured using the Volume of Fluid (VOF) method. The model included two phases, air and molten steel, with a surface tension coefficient of 1.2 N/m.

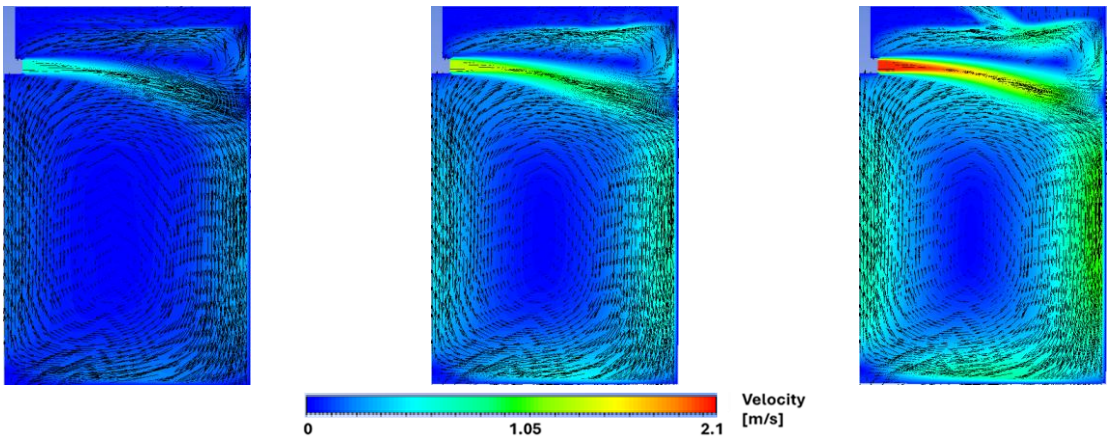


**Fig. 3** Reference flow cases of three different casting speeds. 2 [m/min] [left], 4 [m/min] [middle] and 6 [m/min] [right]

**Obr. 3** Referenční případy průtoku pro tři různé rychlosti lití: 2 [m/min] [vlevo], 4 [m/min] [uprostřed] a 6 [m/min] [vpravo]

Hutnické listy – *Metallurgical Journal*
Speciální vydání / Special Issue, roč. / vol. LXXIX
ISSN Online: 3029-8350

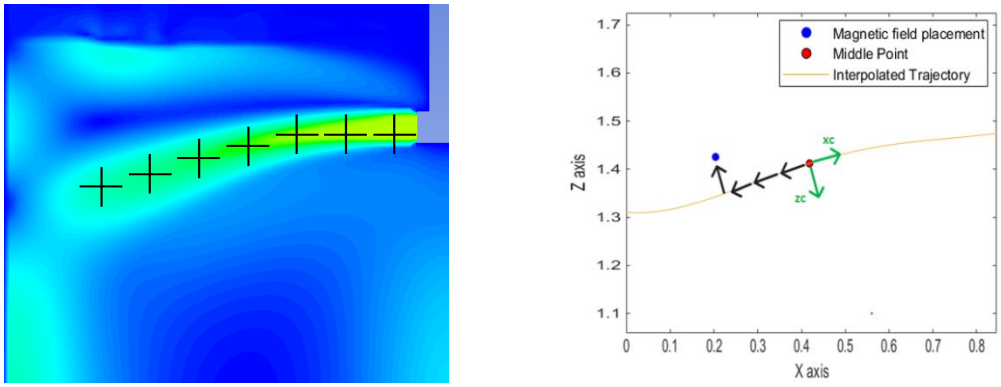


**Fig. 4** Jet trajectory interpolation. The jet in Ansys Fluent [Left]. The jet interpolation in MATLAB [Right]

**Obr. 4** Interpolace dráhy proudu. Proud v programu Ansys Fluent [vlevo]. Interpolace proudu v programu MATLAB [vpravo]

To systematically investigate the influence of key parameters on flow behavior, a Box-Behnken factorial design of experiments (DOE) was employed. Five independent variables were considered: magnetic field intensity, field diameter, horizontal (x) placement, vertical (z) placement, and casting speed. This resulted in a total of 41 simulation cases, spanning the parameter ranges summarized in **Tab. 1**.

**Tab. 1** Overview of Field Intensity, Diameter, Distribution, Placement, and Casting Speed Ranges. $U_{max}$ is the jet maximum velocity across a vertical line, this line is shown in red in Fig. 5

**Tab. 1** Přehled rozsahů intenzity pole, průměru, rozložení, umístění a rychlosti lití. $U_{max}$ je maximální rychlost proudu v průřezu svislou přímkou; tato přímka je na obr. 5 vyznačena červeně

| DOE setup | | | | |
|---|---|---|---|---|
| **Xc placement [m]** | **Zc placement [m]** | **Diameter [m]** | **Peak intensity [tesla]** | **Casting speed [m/s]** |
| -0.2 | Where $\|u\| = -U_{max}/2$ | 0.1 | 0.1 | 2 |
| 0 | 0 | 0.3 | 0.3 | 4 |
| +0.2 | Where $\|u\| = +U_{max}/2$ | 0.5 | 0.5 | 6 |

Due to the absence of experimental measurement data for the local magnetic field distribution, the magnetic field was approximated using a two-dimensional Gaussian function. This analytical function was chosen for its smooth, symmetric profile, which is well-suited for representing localized magnetic fields. To match the desired field diameter and peak intensity, the Gaussian function was appropriately stretched and scaled. The general form of the function, along with the scaling operations applied, is presented in the following set of equations:

$$\sigma = \left(\frac{Diameter/2}{3}\right), \tag{1}$$

$$B_y(x, y, z) = \frac{A}{2\pi\sigma^2} e^{\left\{-\frac{(x-xcenter)^2+(z-zcenter)^2}{2\sigma^2}\right\}}, \tag{2}$$

With A such that:

$$B_y(x_{center}, y, z_{center}) = peak\_magnitude, \tag{3}$$

Hutnické listy – *Metallurgical Journal*
Speciální vydání / Special Issue, roč. / vol. LXXIX
ISSN Online: 3029-8350

Where $x_{center}$ and $z_{center}$ define the spatial location of the local EMBr field center, and $B_y(x_{center}, y, z_{center})$ represents the magnetic field component with maximum intensity.

Several key flow variables were monitored throughout the simulation runs to evaluate the effects of different magnetic field configurations. These variables are summarized below:

- Total force exerted on the narrow face of the mould
- Maximum velocity of the lower recirculation vortex
- Maximum molten steel meniscus level
- Maximum velocity magnitude at the meniscus
- Average velocity magnitude at the meniscus
- Average turbulent kinetic energy in the domain
- Maximum jet velocity along a specified line

**Fig. 5** provides a detailed view of the locations where these variables were recorded. The molten steel level, along with both the maximum and average velocities at the meniscus, were evaluated across the *blue surface*, which corresponds to the region where the steel volume fraction equals 0.5, indicating the interface between air and steel. The total force on the narrow face was measured along the *green vertical surface*, representing the mould wall. Finally, the jet velocity and its deflection were recorded at the *yellow marker*, which also corresponds to the location of the maximum velocity magnitude along the *red reference line*.

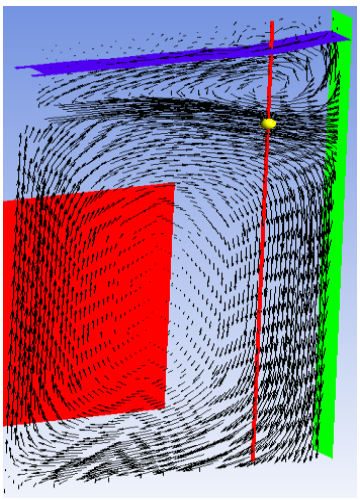

**Fig. 5** Locations for measuring variables / **Obr. 5** Místa měření proměnných

## 3. Result

**Fig.** 6 displays the values of the monitored variables during two key time windows: 15 seconds before (plotted in green, blue and red for the casting speeds 2,4 and 6 m/min respectively) and 15 seconds after (plotted in black) the application of the magnetic fields at *t = 65 s*. A general trend observed immediately after EMBr activation is a sharp decrease in all monitored variables. However, this transient response is followed by a stabilization phase, with most variables reaching a new steady state around *t = 75 s*.

Hutnické listy – *Metallurgical Journal*
Speciální vydání / Special Issue, roč. / vol. LXXIX
ISSN Online: 3029-8350

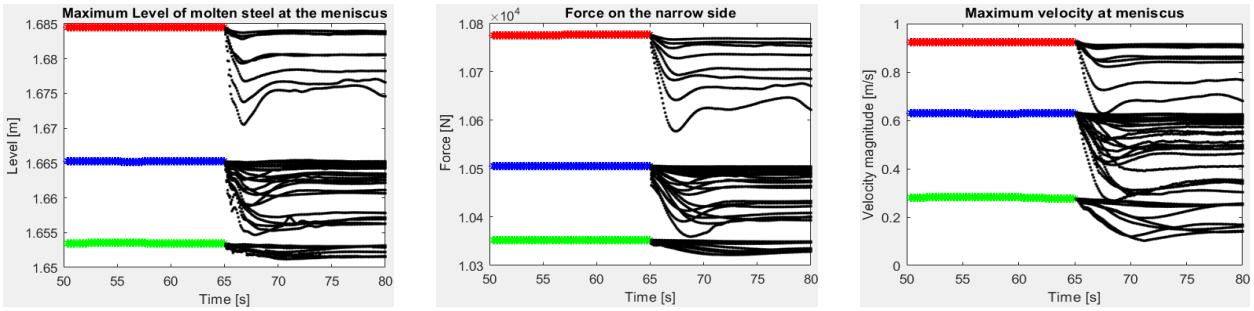


(a) (b) (c)

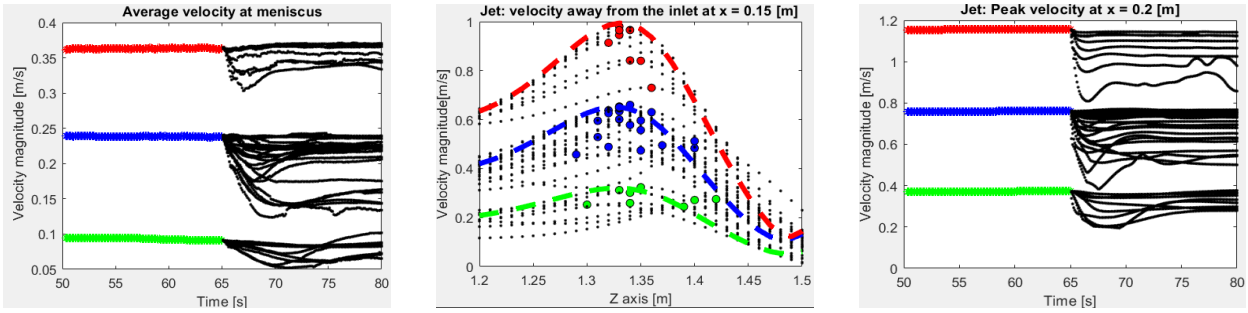


(a) (b) (c)

**Fig. 6** Time variation of monitored variables: Green, blue, and red show casting speeds of 2, 4, and 6 m/min before the field is applied; black shows data during 41 magnetic field applications

**Obr. 6** Časový průběh sledovaných veličin: zelená, modrá a červená barva znázorňují rychlosti lití 2, 4 a 6 m/min před zapnutím magnetického pole; černá barva znázorňuje data během 41 aplikací magnetického pole

**Fig. 7** illustrates the maximum and minimum values achievable through the application of a local magnetic field, as predicted by the regression model fitted to the data shown in **Fig. 6**.

The results indicate that all monitored variables can be either increased or decreased relative to their reference values. The jet deflection ranges approximately ±0.10 m upward and 0.04 m downward. Additionally, the jet velocity can be reduced by approximately 75%, 45%, and 30% for casting speeds of 2, 4, and 6 m/min, respectively.

The molten steel level (standing wave height) decreases by more than 0.02 m at a casting speed of 6 m/min, while the force on the narrow side of the mould is reduced by about 100 N and 200 N at casting speeds of 2 and 6 m/min, respectively. Finally, the velocity of the upper recirculation vortex at the meniscus can be reversed at 2 m/min casting speed and reduced by approximately 50% at 6 m/min.

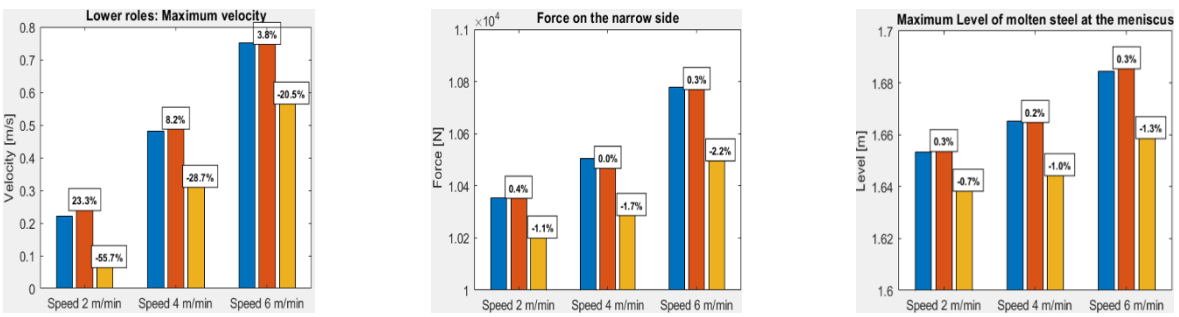


(a) (b) (c)

Hutnické listy – *Metallurgical Journal*
Speciální vydání / Special Issue, roč. / vol. LXXIX
ISSN Online: 3029-8350

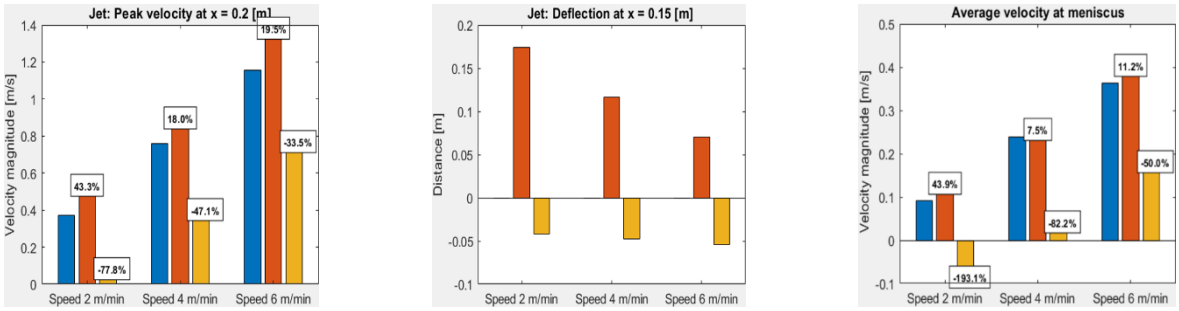


(d) (e) (f)

**Fig. 7** This **Fig.** shows the maximum (red) and minimum (yellow) values of the regression model along with the percentage increase/decrease of the monitored variables reference value (blue)

**Obr. 7** Tento obrázek znázorňuje maximální (červená) a minimální (žlutá) hodnoty regresního modelu spolu s procentuálním nárůstem/poklesem referenční hodnoty sledovaných veličin (modrá)

**Fig. 8** presents a visual comparison between the reference flow field at a casting speed of 4 m/min and the flow field subjected to a local magnetic field. The application of local EMBr results in a substantial reduction in flow velocity within the upper recirculation vortex, accompanied by a noticeable decrease in the lower vortex velocity. Additionally, in panel (b), where a lower-intensity magnetic field is positioned closer to the submerged entry nozzle compared to panel (c), the jet demonstrates increased spreading, reduced deflection, and a more pronounced velocity reduction.

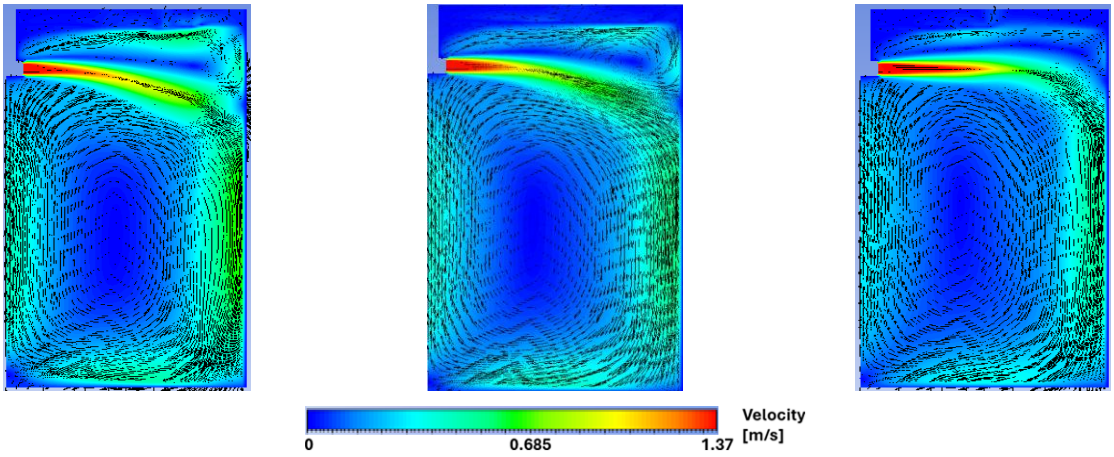


**Fig. 8** [Left] Reference casting speed 4 [m/min]. [middle] The field was placed near the inlet and jet center, was 0.3 [tesla] in peak magnitude and 0.5 [m] in diameter. [Right] The field was placed at the jet middle and center, was 0.5 [tesla] in peak magnitude and 0.5 [m] in diameter

**Obr. 8** [Vlevo] Referenční rychlost lití 4 [m/min]. [Uprostřed] Magnetické pole bylo umístěno v blízkosti vstupu a středu proudu, mělo hodnotu 0,3 [tesla] v píku a průměr 0,5 [m]. [Vpravo] Magnetické pole bylo umístěno uprostřed proudu, mělo š hodnotu 0,5 [tesla] v píku a průměr 0,5 [m]

**Tab. 2** presents the coefficients of a quadratic regression model (as defined in Equation 4), which predicts the behavior of the monitored variables as functions of all five input variables. All input variables are normalized within the range [-1, 1]. Examining the linear terms, naturally casting speed ($x_u$) is the most dominant factor as it strongly increases nearly all monitored variables, particularly total force and jet velocity, while slightly reducing jet deflection. This is reflected in the large, positive values of k_u. The magnetic field's ($x_{xc}$) position and intensity ($x_{B0}$) both reduce the meniscus average velocity and jet velocity, with similar magnitudes ($k_{xc}$ = -0.013, $k_{B0}$ = -0.019).

Hutnické listy – *Metallurgical Journal*
Speciální vydání / Special Issue, roč. / vol. LXXIX
ISSN Online: 3029-8350

Field placement near the inlet (higher $x_{xc}$) also deflects the jet downward. In contrast, positioning the field below the jet (higher $x_{zc}$) increases both the meniscus average velocity and jet velocity, while deflecting the jet upward. Increasing either the field intensity or coil diameter reduces all output variables and deflects the jet downward, with closly similar impacts. However, these trends based solely on linear terms do not capture the full system behavior. Interaction and nonlinear (quadratic) effects are substantial, particularly for $x_{zc}$, $x_D$, and $x_{B_0}$. For instance, the impact of vertical field placement ($x_{zc}$) is amplified when combined with changes in field intensity or coil diameter, as seen in the large interaction coefficients $k_{zc}$: B0 and $k_{zc}$: D.

$$y_r = k_{xc}x_{xc} + k_{zc}x_{zc} + k_D x_D + k_{B0}x_{B_0} + k_u x_u + k_{xc:zc}x_{xc}x_{zc} + k_{xc:D}x_{xc}x_D$$
$$+k_{xc:B0}x_{xc}x_{B0} + k_{xc:u}x_{xc}x_u + k_{zc:D}x_{zc}x_D + k_{zc:B0}x_{zc}x_{B0} + k_{D:u}x_D x_{B0} \quad (4)$$
$$+k_{B0:u}x_{B0}x_u + k_{xc^2}x_{xc^2} + k_{zc^2}x_{zc^2} + k_{D^2}x_{D^2} + k_{B0^2}x_{B0^2} + k_{u^2}x_{u^2} + k_0$$

**Tab. 2** Local EMBr regression model coefficients / **Tab. 2** Koeficienty lokálního regresního modelu EMBr

| Half-mould | Max. steel Level [m] | Tot. Force (on narrow side) [N] | Meniscus Max. Velocity [m/s] | Meniscus Avg. Velocity [m/s] | Jet def. [m] | Jet Velocity [m/s] | Lower role Velocity [m/s] |
|---|---|---|---|---|---|---|---|
| $k_0$ | 1.662 | 10461.041 | 0.482 | 0.216 | 0.02 | 0.652 | 0.452 |
| $k_{xc}$ | -0.001 | -2.122 | -0.025 | -0.013 | -0.014 | -0.009 | -0.006 |
| $k_{zc}$ | 0.002 | 13.851 | 0.048 | 0.017 | 0.012 | 0.033 | -0.009 |
| $k_D$ | -0.002 | -28.141 | -0.075 | -0.02 | 0.009 | -0.052 | -0.027 |
| $k_{B0}$ | -0.002 | -36.47 | -0.085 | -0.019 | 0.018 | -0.073 | -0.032 |
| $k_u$ | 0.014 | 189.175 | 0.322 | 0.139 | -0.011 | 0.369 | 0.261 |
| $k_{xc:zc}$ | 0 | 3.279 | -0.012 | 0.004 | -0.003 | 0.004 | 0.005 |
| $k_{xc:D}$ | -0.001 | -2.207 | -0.011 | -0.015 | -0.015 | -0.012 | -0.002 |
| $k_{xc:B0}$ | -0.002 | -6.575 | -0.049 | -0.019 | -0.012 | -0.025 | -0.006 |
| $k_{xc:u}$ | 0 | 5.36 | 0.017 | 0.001 | 0.007 | 0.019 | 0.004 |
| $k_{zc:D}$ | 0.001 | 15.832 | 0.037 | 0.012 | 0.008 | 0.031 | 0.001 |
| $k_{zc:B0}$ | 0.002 | 21.375 | 0.046 | 0.018 | 0.018 | 0.055 | -0.014 |
| $k_{zc:u}$ | 0 | 1.348 | -0.015 | -0.002 | -0.01 | -0.014 | -0.006 |
| $k_{D:B0}$ | -0.001 | -17.544 | -0.041 | -0.019 | 0.015 | -0.032 | -0.027 |
| $k_{D:u}$ | -0.001 | -17.177 | -0.007 | -0.001 | -0.01 | -0.013 | -0.001 |
| $k_{B0:u}$ | -0.002 | -27.79 | -0.034 | -0.007 | -0.015 | -0.046 | -0.01 |
| $k_{x^2}$ | 0 | -1.752 | 0.02 | -0.005 | -0.005 | 0.016 | 0.002 |
| $k_{zc^2}$ | 0.001 | 15.915 | 0.035 | -0.001 | -0.022 | 0.044 | 0.011 |
| $k_{D^2}$ | 0 | 2.251 | 0.015 | -0.007 | -0.004 | 0.01 | -0.001 |
| $k_{B0^2}$ | 0 | -1.595 | 0.014 | -0.004 | 0.004 | 0.005 | -0.003 |
| $k_{u^2}$ | 0.004 | 61.513 | 0.018 | 0.006 | 0.005 | 0.024 | 0.005 |

Hutnické listy – *Metallurgical Journal*
Speciální vydání / Special Issue, roč. / vol. LXXIX
ISSN Online: 3029-8350

## 4. Conclusion

A numerical model was developed to couple electromagnetic effects with molten steel flow within a thin-slab casting mould. The impact of the localized electromagnetic brake (EMBr) is summarized in the **Tab. 3** below.

1. Near Inlet Placement:
   - Results in a slight reduction in molten steel level and overall flow damping, as seen by reductions in force on the narrow face, lower role velocity, meniscus velocity, and jet velocity.
   - The jet is deflected downward, likely due to flow suppression near the inlet.
2. Below Jet Placement:
   - Tends to increase molten steel level, meniscus velocity and force on the narrow side, while decreasing lower role velocity.
   - Meniscus and jet velocities increase, with an upward jet deflection, indicating enhanced upward flow momentum near the meniscus due to deeper magnetic interaction.
3. Larger Diameter (EMBr coils):
   - Causes slight reductions across most parameters, suggesting a more distributed but weaker magnetic braking effect.
   - Jet deflects upward, possibly due to a broader but less intense magnetic influence.
4. Higher Intensity (Magnetic field):
   - Similarly to larger diameter, it shows reductions in flow-related parameters, with upward jet deflection.
   - Indicates stronger suppression of turbulent jet dynamics due to increased magnetic force.

**Tab. 3** A summary of local EMBr application effects / **Tab. 3** Souhrn účinků lokální aplikace EMBr

| Field parameter | Molten steel level | Force on the narrow side | Lower role velocity | Meniscus average velocity | Jet deflection | Jet velocity |
|---|---|---|---|---|---|---|
| **Near inlet placement** | Sightly Reduced | Reduced | Reduced | Reduced | Downward | Reduced |
| **Below jet placement** | Slightly Increased | Increased | Decreased | Increased | Upward | Increased |
| **Larger diameter** | Slightly Reduced | Reduced | Reduced | Reduced | Upward | Reduced |
| **Higher intensity** | Slightly Reduced | Reduced | Reduced | Reduced | Upward | Reduced |

## References

[1] A.R. A. Aziz and S. A. Aziz, 2018. IOP Conf. Ser.: Mater. Sci. Eng. 454 012001
[1] ANSYS, Inc, 2013. ANSYS Fluent Manetohydrodynamics (MHD) Module Manual. Available at: ANSYS FLUENT 12.0 Magnetohydrodynamics Module Manual [Accessed 10 June 2025]
[2] Brian G. Thomas. Introduction to Continuous Casting. Available at: Intro to Continuous Casting - CCC - U of I [Accessed 15 June 2025]
[3] Johan E. Carlson, 2022. Measurement systems Engineering. 2nd ed. Sweden: JEC Engineering and Media Production AB.
[4] Seong-Mook Cho, 2019. "Electromagnetic Forces in Continuous Casting of Steel Slabs". metals.

Hutnické listy – *Metallurgical Journal*
Speciální vydání / Special Issue, roč. / vol. LXXIX
ISSN Online: 3029-8350

# Determination of Cooling Practices for Cold Charging Crack-Sensitive Slabs at ArcelorMittal Plants

# Stanovení postupů chlazení pro studené vsazování bram citlivých na trhliny v provozech ArcelorMittal

**Chongzhi Abel Chang[1], Hongbin Yin[2]**

[1] ArcelorMittal Global R&D Hamilton, Canada, 1390 Burlington Street East, Hamilton, Ontario, L8N 3J5, Canada, *Contact e-mail: abel.chang@arcelormittal.com
[2] ArcelorMittal Global R&D East Chicago, United States, 3001 East Columbus Dr., East Chicago IN 46312, United States, Contact e-mail: hongbin.yin@arcelormittal.com

## Abstract

*At conventional steel plants, some crack-sensitive slabs, such as high-alloyed AHSS (Advanced High-Strength Steel) and UHSS (Ultra-High-Strength Steel) grades, have to be cold charged due to restrictions associated with plant conditions. In order to minimize the risk of crack formation caused by thermal stresses during cooling, slow cooling must be applied to some of these slabs. To calculate the cooling stresses and temperature evolution, thermo-mechanical finite element (FE) models were developed. The results were analysed to estimate the risk of crack formation with the aim of determining the cooling practices for crack-sensitive slabs.*

***Keywords:*** *FE model, cold charging, crack formation, slow cooling, slab*

## Abstrakt

*V běžných ocelárnách musí být některé desky citlivé na praskání, například vysoce legované oceli AHSS (Advanced High-Strength Steel) a UHSS (Ultra-High-Strength Steel), podávány studeně kvůli omezením provozních podmínek. Aby se minimalizovalo riziko vzniku trhlin způsobených tepelným namáháním během ochlazování, je u některých z těchto desek nutné aplikovat pomalé ochlazování. Pro výpočet ochlazovacích napětí a vývoje teploty byly vyvinuty termomechanické modely konečných prvků (FE). Výsledky byly analyzovány za účelem odhadu rizika tvorby trhlin s cílem optimalizovat postupy ochlazování bram citlivých na trhliny.*

***Klíčová slova:*** *model konečných prvků (FE), studené sázení, bramy, pomalé ochlazování, tvorba trhlin*

## 1. Introduction

At conventional steel plants, steel slabs are delivered from the caster to the slab yard and stacked in a pile for cooling. This process is referred to as "normal stack cooling" (**Fig. 1a**). These slabs are either allowed to cool to ambient temperature and be subsequently charged into the reheating furnace (RHF), known as "cold charged" slabs, or they are moved directly to the RHF to be charged as hot as possible, termed "warm" or "hot" charging. In addition to significant energy and productivity benefits, warm charging is also able to reduce the risk of crack formation for crack-sensitive slabs that have high alloying elements.

At some ArcelorMittal plants, some crack-sensitive slabs (e.g., AHSS and UHSS grades) that are normal stack cooled and then cold charged can develop cracks caused by thermal stress. However, warm charging is not always available in these plants. Therefore, to reduce thermal stresses during cooling, these slabs must be cooled in an insulated cover (**Fig. 1b**) to ensure a very low cooling rate compared with normal stack cooling.

Hutnické listy – *Metallurgical Journal*
Speciální vydání / Special Issue, roč. / vol. LXXIX
ISSN Online: 3029-8350

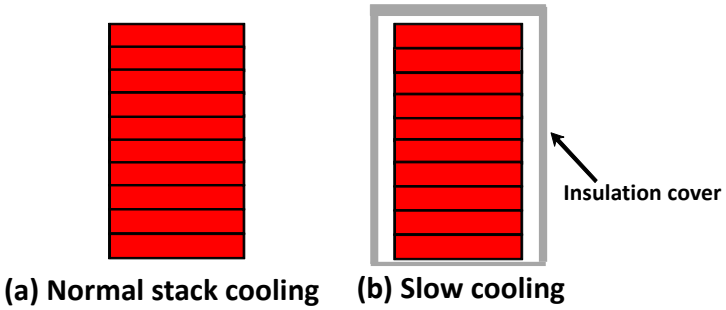


**Fig. 1** Illustration of (a) normal stack cooling and (b) slow cooling

**Obr. 1** Ilustrace (a) normálního chlazení a (b) pomalého chlazení

The slabs are then cold charged to the RHF of the hot mill. This cooling process is known as "slow cooling". Due to limitations in logistics, the number of insulated boxes, and productivity, it is difficult and uneconomical to slow cool all crack-sensitive grades.

In order to define the cooling practices for the crack-sensitive grades - in other words, to determine whether it is necessary to slow cool these slabs - finite element (FE) models were developed to simulate both slow and normal stack cooling processes, and the models were validated based on actual temperature measurements. The simulation results were used to characterize the risk of crack formation during cooling with the goal of defining the slab cooling practices at ArcelorMittal plants.

## 2. Methodology

The slab cooling models were developed using ABAQUS and consisted of two parts: thermal models and a stress model.

### Thermal models (Normal stack cooling and Slow cooling)

Simulations were run to obtain the slab temperature evolutions for normal stack cooling and slow cooling. The slow cooling model was developed based on the previously developed normal stack cooling model. As shown in **Fig. 2**, the results reveal that the slow cooling slab takes a much longer time to reach the same temperature as the normal stack cooled slab. To allow for a valid comparison, these two simulations used the same initial conditions, slab dimensions, and grades.

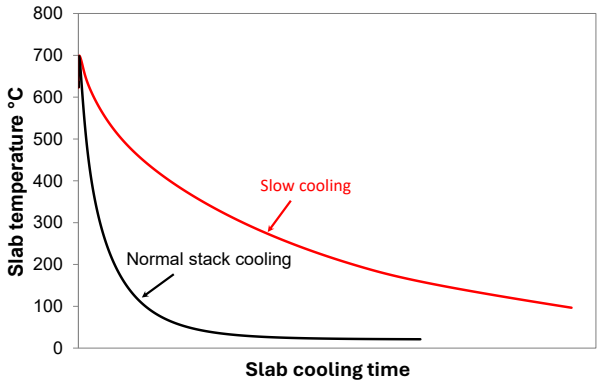


**Fig. 2** Temperature evolutions during normal stack cooling and slow cooling processes

**Obr. 2** Vývoj teploty během běžného a pomalého ochlazování

Hutnické listy – *Metallurgical Journal*
Speciální vydání / Special Issue, roč. / vol. LXXIX
ISSN Online: 3029-8350

## Stress model

Temperature field data from the 3D thermal models is mapped to model the stress distribution developed during cooling as shown in **Fig. 3**. Simulation results of the stress models are applied to analyse stress evolution during normal stack cooling and slow cooling practices. Stresses induced by phase transformation inside slab is also considered in the simulation.

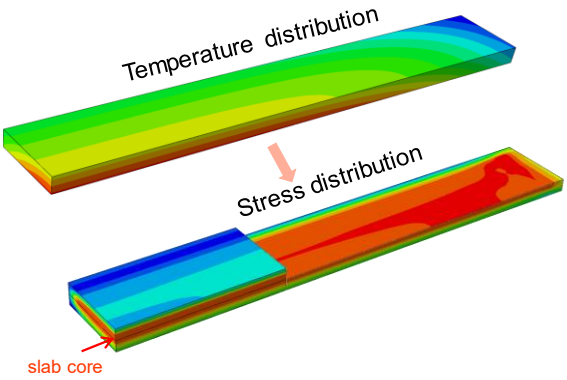


**Fig. 3** Stress distribution of a slab during late-stage of cooling (Quarter-slab model)

**Obr. 3** Distribuce napětí bramy v pozdní fázi ochlazování (Quarter-slab model)

**Fig. 4** shows the stress evolutions of a crack-sensitive grade slab during normal stack cooling and slow cooling. The results indicate that the stresses in normal stack cooling are significantly higher than those in slow cooling after the early stage of cooling (slab temperature below approximately 500°C). In order to eliminate unnecessary variation, this study focuses on the stress analyses after this early stage of cooling.

In addition, it should be noted that stress alone is not sufficient to characterize the risk of crack formation if the effects of slab properties and temperature are not considered. Therefore, a crack formation index, which accounts for the effects of these factors and is calculated using an ABAQUS subroutine, is introduced and used to assess the risk of crack formation during cooling.

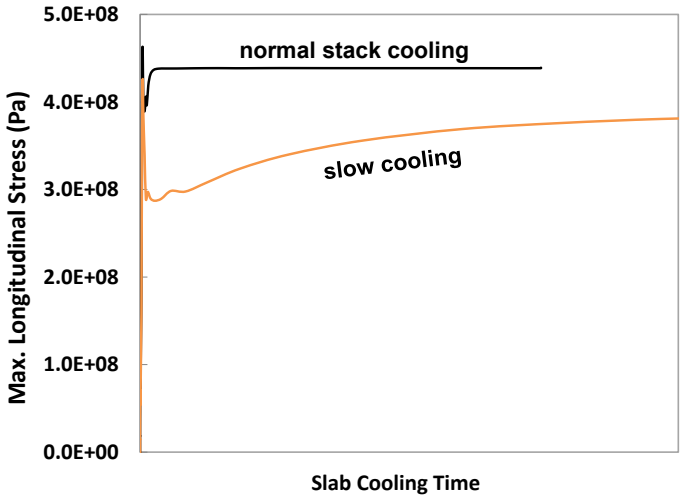


**Fig. 4** Slab stress evolutions of a studied grade at various cooling conditions

**Obr. 4** Vývoj napětí bramy u zkoumaného druhu oceli za různých podmínek ochlazování

Hutnické listy – *Metallurgical Journal*
Speciální vydání / Special Issue, roč. / vol. LXXIX
ISSN Online: 3029-8350

### Input and output of the models

The inputs and outputs of the FE models are shown in **Fig. 5**. The thermal properties and phase transformation temperatures for different steel grades were measured in the lab, calculated with commercial software or obtained from literature data [1]. The mechanical properties of the studied cracking sensitive grades were measured on as-cast slabs.

Since mechanical property test samples were taken from different positions along the cross-section of the slabs, the variation in mechanical properties was also considered in this study. The models were applied to both slab cooling and reheating processes [1]. However, this study focuses on the analysis of slab cooling processes.

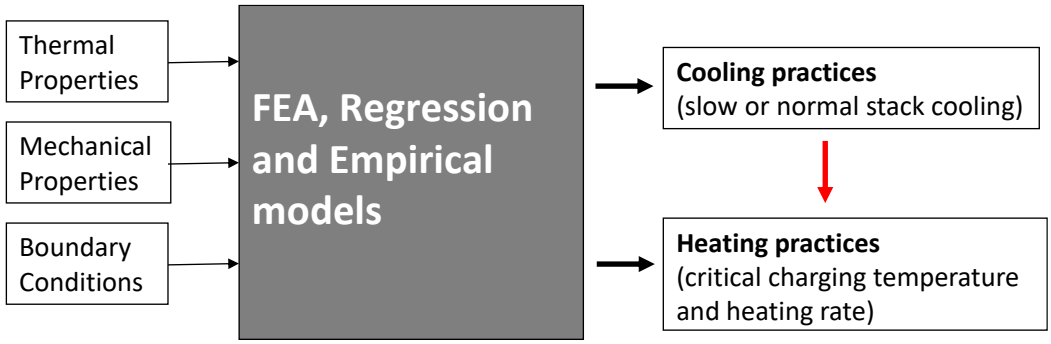


**Fig. 5** Inputs and outputs of the models

**Obr. 5** Vstupy a výstupy modelů

## 3. Results Analysis

Slab stress and temperature are calculated using the FE models. Based on the analysis of simulation results and historical data on slab cracking and breakage incidents, cooling practices are proposed.

### Crack formation index - Characterizing the risk of crack formation

Simulations were run to analyse the stress evolution of various crack-sensitive grades during slow cooling. As shown in **Fig. 6**, after the early stage of slab cooling, the stress of slab Grade A is the lowest and Grade D slab is the highest among the studied grades during slow cooling.

As mentioned earlier, to better characterizing the risks of crack initiation and propagation caused by thermal stress, crack formation index can be obtained based on stress evolution after early stage of cooling.

The results plotted in **Fig. 7** show that, for all crack-sensitive grades subjected to slow cooling until reaching ambient temperature, Grade B has the highest crack formation index, and Grade A has the lowest, representing the highest and lowest risk of cracking, respectively, among the studied grades.

As shown in **Fig. 6**, the sequence of slow cooling stress for the studied grades, from highest to lowest, is D, B, C, A. This differs from the sequence of crack formation index: B, C, D, A. These results demonstrate that crack formation index should be employed to analyse the risk of crack formation.

Hutnické listy – *Metallurgical Journal*
Speciální vydání / Special Issue, roč. / vol. LXXIX
ISSN Online: 3029-8350

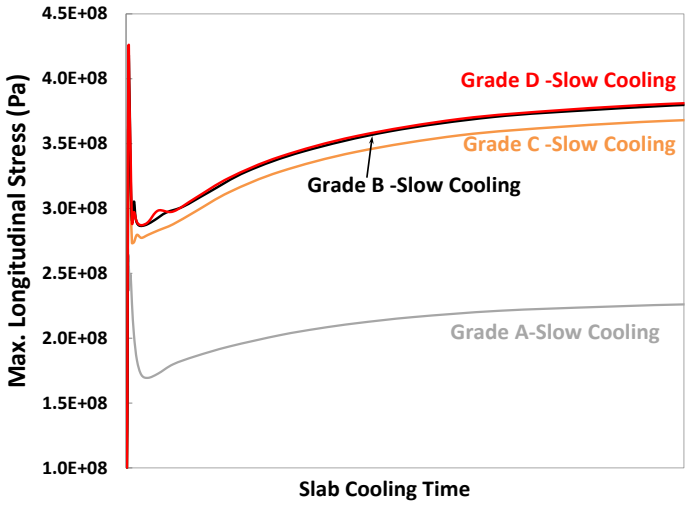


**Fig. 6** Slow cooling stress evolution of various studied grades

**Obr. 6** Vývoj napětí při pomalém ochlazování u různých zkoumaných jakostí

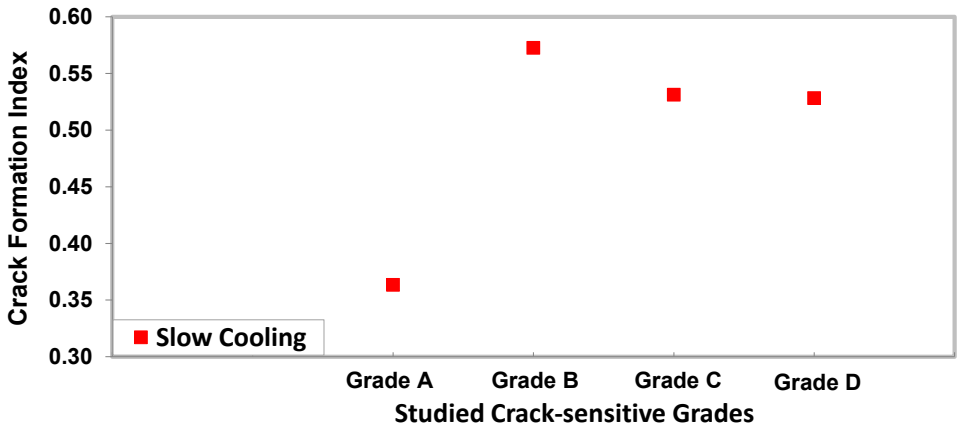


**Fig. 7** Crack formation index of different crack-sensitive grades during slow cooling

**Obr. 7** Index tvorby trhlin u různých druhů oceli náchylných k tvorbě trhlin při pomalém ochlazování

### Determine the cooling practice based on crack formation index and historical data

To estimate the risk of crack formation, in addition to the crack formation index of slow cooled slabs, the analysis also considered the crack formation index of normal stack cooled slabs, historical production data of crack-sensitive grades, and reference grades.

**Fig. 8** displays the crack formation index of each studied grade during both normal stack cooling and slow cooling. Grade E, which has relatively high alloying elements, is included as a reference because it has undergone normal stack cooling and cold charging for many years at some ArcelorMittal plants without any defects caused by thermal stresses. As shown in **Fig. 8**, the crack formation index of normal stack cooled Grade A slabs is lower than that of Grade E slabs.

Therefore, slow cooling Grade A is not necessary. The crack formation index of Grade E during normal stack cooling is significantly lower than those of Grade B, C and D during slow cooling. This indicates that slow cooling Grade B, C and D slabs have higher risk of crack formation than normal stack cooling of Grade E, so further analyses is required to define their cooling practices.

Hutnické listy – *Metallurgical Journal*
Speciální vydání / Special Issue, roč. / vol. LXXIX
ISSN Online: 3029-8350

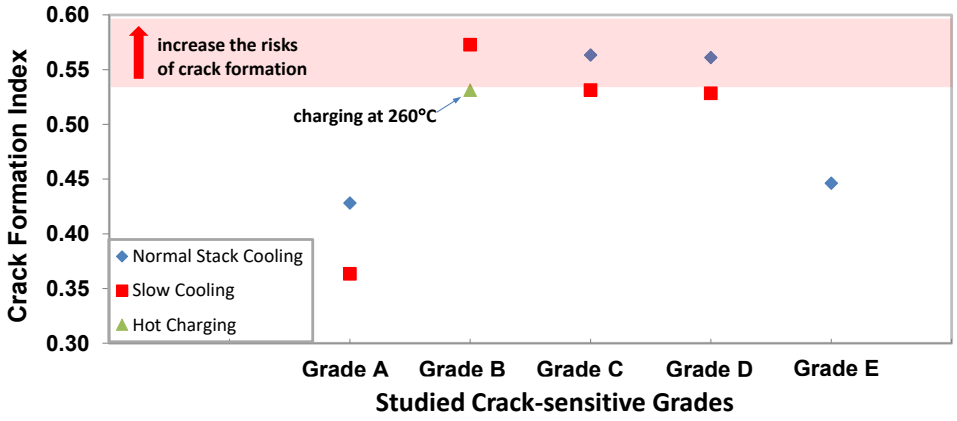


**Fig. 8** Crack formation index of different crack-sensitive grades during normal stack cooling and slow cooling

**Obr. 8** Index tvorby trhlin u různých druhů oceli náchylných k tvorbě trhlin při běžném ochlazování a při pomalém ochlazování

In trials at ArcelorMittal plants, cracks were found on the normal stack cooled Grade D slabs and the slow cooled Grade B slabs, demonstrating that slow cooling is insufficient to lower the risk of crack formation for Grade B slabs. As shown in **Fig. 8**, the crack formation index of normal stack cooled Grade C and D is similar to that of slow cooled Grade B slabs, aligning with trial results. This, indicates that the Grade C and D slabs must be slow cooled.

Notably, cracks were not found on slow cooled and cold charged Grade C and D in the following trials. Thus, in terms of the simulation results and actual industrial trials, slow cooled and cold charged Grade C and D slabs can be considered as low risk of crack formation from the perspective of cooling stress analysis.

In addition, assuming that crack formation index of slow cooled Grade C is used as the critical index, simulation results suggest that slow cooling Grade B slabs should be charged with a temperature at least 260 °C to minimize cracking risk. However, this also means Grade B cannot be produced at plants where warm charging is unavailable.

The proposed cooling practices of the studied grades are summarized in **Tab. 1**. They have been successfully implemented at several ArcelorMittal plants for over five years. This method is also applied to determine cooling practices for newly developed crack-sensitive grades, as well as to optimize reheating practices for both newly developed and historical crack-sensitive grades.

**Tab. 1** Summary of cooling practices of the studied crack sensitive slabs
**Tab. 1** Přehled způsobů chlazení zkoumaných desek náchylných ke vzniku trhlin

| Studied grades | Slow cooling | Cold charging |
|---|---|---|
| Grade A | No | Yes |
| Grade B | Yes | No (require warm charging) |
| Grade C | Yes | Yes |
| Grade D | Yes | Yes |
| Grade E | No | Yes |

Hutnické listy – *Metallurgical Journal*
Speciální vydání / Special Issue, roč. / vol. LXXIX
ISSN Online: 3029-8350

It should be noted that this study focuses on cooling stress analysis. In addition to the cooling stress and temperature, slab microstructure, heating rate, martensite formation, hydrogen embrittlement and abnormal process parameters also play important roles in crack formation.

## 4. Summary and Conclusions

Thermo-mechanical FE models were successfully developed to simulate normal stack cooling and slow cooling processes of slabs under plant-specific conditions. In order to characterize the risk of crack formation, the concept of crack formation index was introduced.

Based on the crack formation index and historical data from production trials of the studied crack-sensitive grades, cooling and charging practices can be determined for various grades. These proposed cooling practices can significantly reduce the risk of crack formation for these grades.

These practices have been successfully implemented for more than five years at several ArcelorMittal plants which produce highly crack-sensitive grades. The methodology is also used to determine cooling practices for newly developed crack-sensitive grades, as well as reheating practices at hot mills.

This report focuses on cooling stress analysis. Other factors, such as slab microstructure, heating rate, martensite formation, hydrogen embrittlement and abnormal process parameters, can also significantly affect the risk of crack formation.

### Acknowledgements

***The authors would like to thank their colleagues at ArcelorMittal for their support and technical inputs: Mike Tesone, Bernie Jeffrey, Fred Dvorak, Dan Kruse, Mark Nicholls, David White.***

### Reference

[1] Chang, C., Fitzpatrick, J.J., Ianos, A., Cheung, A., Colbert, D., Gebara, G. Redefining Warm Charging Rules at ArcelorMittal Dofasco. In: Proceedings of the 8th International Conference on Modelling and Simulation of Metallurgical Processes in Steelmaking (STEELSIM 2019), Toronto, Canada, 13–15 August 2019. Association for Iron and Steel Technology (AIST), 2019.

Hutnické listy – *Metallurgical Journal*
Speciální vydání / Special Issue, roč. / vol. LXXIX
ISSN Online: 3029-8350

# Optimising Strength in Structural Steel Tubes Via Modelling of the Controlled Cooling Process

# Optimalizace pevnosti konstrukčních ocelových trubek pomocí modelování procesu řízeného ochlazování

**Nathan Dixon[1], Denzi Li[1], Jinlong Du[2], Carl Slater[1], Claire Davis[1]**

[1] WMG, University of Warwick, United Kingdom. *Contact e-mail: N.Dixon.1@warwick.ac.uk
[2] Tata Steel Research and Innovation Ltd, United Kingdom

## Abstract

*Grain size strengthening predominantly determines the strength of low-carbon low-alloy steel tube grades consisting of a ferrite-pearlite microstructure. While recent changes to standards now permit the use of controlled cooling to refine grain size and enhance mechanical properties, the industrial application of multi-stage controlled cooling lacks robust predictive models. This study developed a finite element (FE) COMSOL-based modelling framework that integrates thermodynamic simulations, phase transformation data, and empirical grain-size relationships to simulate industrial water and air-cooling stages.*

*The model achieves high predictive accuracy by focusing on the critical undercooling threshold where the first 40% of ferrite forms. Validation against industrial production data yielded a root mean square error (RMSE) of 6.5 MPa for ultimate tensile strength. Furthermore, a parametric study of 22 cooling configurations demonstrates that optimised processing can achieve a 5% strength uplift for specific geometries while successfully avoiding undesirable bainite formation. This framework provides a robust tool for manufacturers to improve process control, product design, and mechanical performance.*

***Keywords**: controlled cooling, steel tube manufacturing, ferrite grain size control, FE modelling, phase transformation, process optimisation*

## Abstrakt

*Pevnost trubek z nízkouhlíkových nízkolegovaných ocelí s ferit-perlitovou mikrostrukturou je převážně určena velikostí zrna. Ačkoli nedávné změny norem nyní umožňují využití řízeného ochlazování ke zjemnění zrna a zlepšení mechanických vlastností, pro průmyslové uplatnění vícestupňového řízeného ochlazování dosud neexistují spolehlivé prediktivní modely. V této studii byl vyvinut modelovací rámec založený na metodě konečných prvků (FE) v prostředí COMSOL, který integruje termodynamické simulace, data o fázových přeměnách a empirické vztahy velikosti zrn pro simulaci průmyslových fází chlazení vodou a vzduchem. Model dosahuje vysoké prediktivní přesnosti díky zaměření na kritickou prahovou hodnotu podchlazení, při níž se tvoří prvních 40% feritu. Ověření na základě průmyslových výrobních dat vykázalo chybu střední kvadratické odchylky (RMSE) 6,5 MPa pro mez pevnosti v tahu. Parametrická studie 22 konfigurací chlazení dále ukazuje, že optimalizovaným zpracováním lze u specifických geometrií dosáhnout zvýšení pevnosti o 5% a současně úspěšně zabránit nežádoucí tvorbě bainitu. Tento rámec poskytuje výrobcům robustní nástroj pro zlepšení řízení procesů, návrhu produktů a mechanických vlastností.*

***Klíčová slova:** řízené ochlazování, výroba ocelových trubek, řízení velikosti zrn feritu, modelování metodou konečných prvků, fázová transformace, optimalizace procesu*

Hutnické listy – *Metallurgical Journal*
Speciální vydání / Special Issue, roč. / vol. LXXIX
ISSN Online: 3029-8350

## 1. Introduction

Structural steel tubes in the EN S355-S460 range are widely used in structural applications that demand reliable combinations of strength and ductility. These grades are designed to achieve yield strengths between 355 MPa and 460 MPa, with corresponding ultimate tensile strengths ranging from 470 MPa to 720 MPa [1]. The typical chemical composition of steel grade S355 is shown below in **Tab. 1**. These tubes consist of ferrite-pearlite microstructures and primarily derive strength from the ferrite grain size formed during cooling after tube shaping. A ferrite-pearlite microstructure is targeted for these products, as the presence of bainite or martensite can lead to undesirable variability in mechanical performance. With recent changes to standards now permitting controlled cooling rather than continuous cooling [1], opportunities have emerged to refine ferrite grain size and enhance mechanical properties further. Ensuring that tubes remain within the correct transformation regime during cooling is therefore essential for achieving the required and consistent strength levels.The present study develops and validates a modelling framework that integrates thermophysical simulation, CCT-based phase transformation prediction and empirical grain-size relationships to support optimisation of cooling strategies [8] in industrial tube production.

**Tab. 1** Typical chemical composition of steel grade S355 [1]
**Tab. 1** Typické chemické složení ocelové třídy S355 [1]

| Grade | C max. (Wt%.) | Si max. (Wt%.) | Mn (Wt%.) | Nb max. (Wt%.) |
|---|---|---|---|---|
| S355 | 0.2 | 0.5 | 0.9 – 1.65 | 0.05 |

Previous modelling efforts have mainly focused on the thermodynamic modelling of hot rolling [2], forming [3], continuous cooling of tubes [4] and rapid quenching [5]. To date, no existing models investigate the multi-stage controlled cooling of tubes to predict both thermal history and product properties. To achieve a model of this production process, consideration of thermal history, phase transformation and microstructure are required.

### 1.1 Tube Manufacturing

The final mechanical properties of structural steel tubes are established during a two-stage controlled cooling process applied immediately after tube forming and annealing. Initially, tubes are annealed at temperatures ranging from 850 °C to 1000 °C for durations ranging from 18 to 30 minutes [6-8]. This stage ensures the development of a uniform austenite microstructure prior to transformation. After annealing, water cooling is used to rapidly lower the tube temperature; these cooling rates can span 0.3 °C/s to 50 °C/s [9, 10], depending on product geometry. During this water-cooling stage, the aim is to form ferrite under high undercooling conditions. Water cooling brings the tube down to temperatures above the bainite formation region, generally between 550 °C and 600 °C. Once the appropriate temperature range has been reached, tubes are slowly air cooled down to room temperature (at rates ranging from 0.06 °C/s-0.9 °C/s) [4, 11]. Due to variations in geometry, wall thickness, line speed, and cooling configuration, the industrial cooling profile varies significantly across the tube's perimeter and through its thickness [12]. The typical thermal profile range experienced industrially can be seen in **Fig. 1**. Understanding the thermal profiles generated industrially and the potential variations are essential for understanding and predicting the resulting microstructure and mechanical properties.

Hutnické listy – *Metallurgical Journal*
Speciální vydání / Special Issue, roč. / vol. LXXIX
ISSN Online: 3029-8350

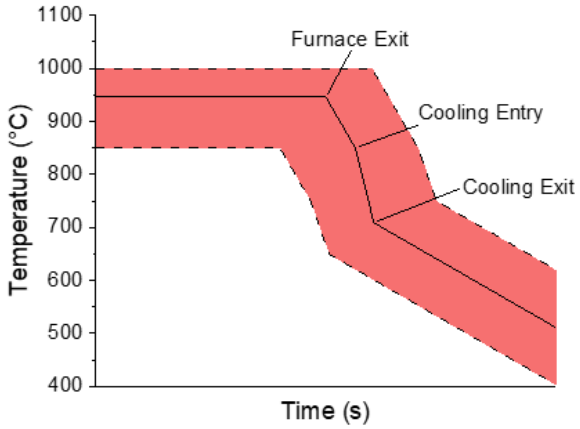


**Fig. 1** Typical thermal profile experienced during tube manufacturing

**Obr. 1** Typický teplotní profil při výrobě trubek

### 1.2 Grain Size Control During Controlled Cooling

Ferrite grain size plays a critical role in determining the mechanical properties of S-grade structural steels, contributing as much as 60% of the final yield strength [13]. Grain refinement is typically promoted by high cooling rates to achieve increased undercooling, which influences the balance of ferrite nucleation and growth [14]. A previous experimental study has established that during controlled cooling, a strong correlation exists between the ferrite grain size and the undercooling at which the initial 40% ferrite forms [15]. This empirical relationship can be seen in Eq. (1), where $\Delta T_{40\%}$ is the undercooling at which 40% ferrite forms. This equation is known to apply for an austenite grain size, dγ, of 10 μm.

$$d_\alpha = 0.71 \cdot d_\gamma \cdot e^{-0.0038 \cdot \Delta T_{40\%}} \quad (1)$$

Within the initial 40% of ferrite formation, the consumption or saturation of nucleation sites within the initial 40% of ferrite formation prevents further nucleation, thereby determining the final grain size. To maximise the degree of achievable ferrite refinement, the undercooling within this initial 40% of ferrite formation should be maximised. Achieving sufficient undercooling to refine the grain size, whilst simultaneously avoiding entry into the bainitic transformation range, is therefore essential for achieving the required strength levels.

However, to gain an understanding of the ferrite grain sizes produced during industrial controlled cooling, the 40% undercooling needs to be known. A solution to identifying these values is a finite element model of the tube manufacturing to predict thermal history and phase fraction.

## 2. Aims

The primary objective of this work is to develop a finite element (FE) COMSOL based model capable of simulating the controlled cooling process used during the manufacture of structural steel tubes. The model aims to predict the thermal history of tubes subjected to a wide range of industrial cooling conditions and to use these predictions to estimate ferrite grain size and resultant mechanical properties.

Hutnické listy – *Metallurgical Journal*
Speciální vydání / Special Issue, roč. / vol. LXXIX
ISSN Online: 3029-8350

By integrating thermodynamic and phase transformation models alongside empirical grain size and mechanical property relationships, the model should provide a framework for evaluating and optimising cooling strategies. Ultimately, the goal is to identify cooling conditions that can deliver improved strength levels across different tube geometries and thicknesses, supporting the development of improved efficiency, higher-performance cooling strategies.

## 3. Modelling Methodology

### 3.1 Tube production process

The tube production process (see **Fig. 2**) begins with annealing, where the tube is heated to achieve the desired austenite microstructure. Post annealing, tubes are subsequently descaled and formed into their final rectangular geometry. Prior to forming, tubes are circular with a radius of 20 inches (508 mm), the shaping from circular to rectangular induces negligible strain, which is not expected to noticeably influence phase transformation. Tubes are then cooled using eight cooling banks to achieve a targeted exit temperature (above the bainite formation region). Each cooling bank utilises multiple nozzles to achieve a uniform reduction in temperature around the tube perimeter, as illustrated by the nozzle arrangement in the inset diagram. After water cooling, tubes are left on the run-out table.

Temperature is measured at key points using pyrometers located at the furnace exit, cooling entry, and cooling exit. The temperature-time plot from those pyrometer readings was shown earlier in **Fig. 1**, which demonstrates the range of thermal profiles that can be generated via processing parameter variation.

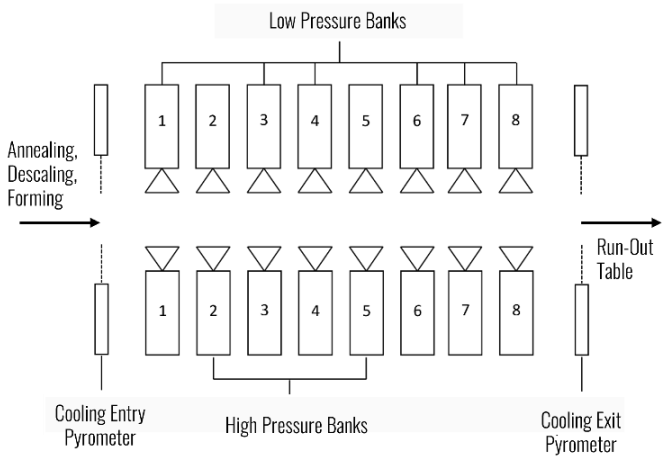


**Fig. 2** Schematic showing the tube manufacturing process with cooling banks emphasised

**Obr. 2** Schéma znázorňující proces výroby trubek s vyznačenými chladicími sekcemi

### 3.2 Model Setup

For the investigation of this topic, an FE model was developed using COMSOL (version 6.3) to capture the thermal and microstructural behaviour of tubes during production. The model integrates a comprehensive set of geometric and process inputs. These are supplemented by material-specific data, as well as physical properties sourced from JMatPro (version 15.1) which include temperature dependent material properties. Another export from JMatPro includes CCT / TTT data for the S355 alloy.

Hutnické listy – *Metallurgical Journal*
Speciální vydání / Special Issue, roč. / vol. LXXIX
ISSN Online: 3029-8350

These inputs are used to produce a thermal profile and phase fraction, from which the ferrite grain size can be determined. Once grain size is determined, mechanical properties such as yield and ultimate tensile strength can be derived. A flow chart illustrating the inputs and outputs of the FE model is shown below in **Fig. 3.**

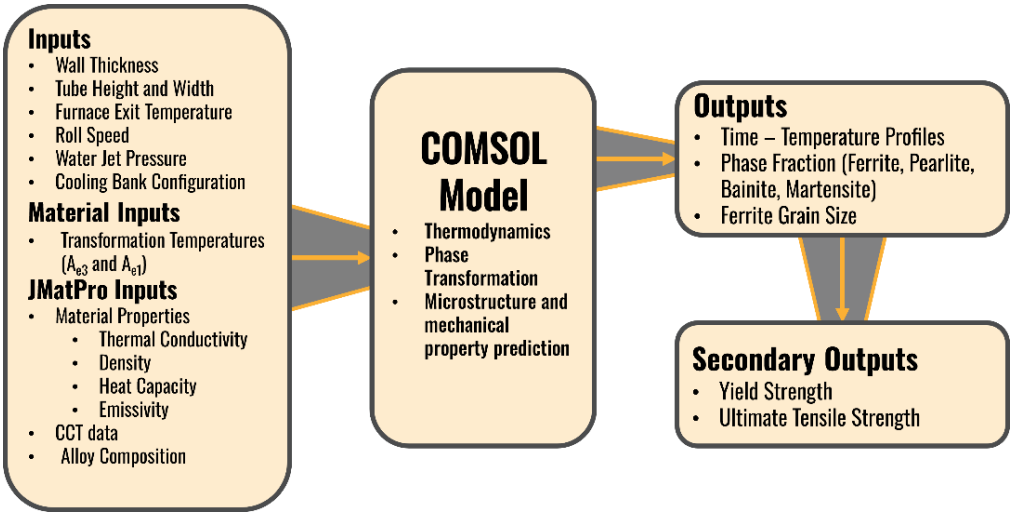


**Fig. 3** Flow chart demonstrating the inputs and outputs of the FE model

**Obr. 3** Schéma znázorňující vstupy a výstupy modelu konečných prvků

Building on the defined model setup, the simulation focuses on a 2D quarter cross-section of a rectangular tube, capturing its behaviour from the furnace exit through to the run-out table. The cooling process is represented using a combined approach that accounts for water-jet cooling as well as heat losses through radiation and convection, as illustrated by the boundary-condition layout (see **Fig. 4**). Latent heat is also included as a heat source within the material bulk. Within **Fig. 4**, the model meshing can be seen where a finer mesh is utilised in the regions where industrial tensile tests would be taken from. Where no industrial data is available, a coarser meshing is utilised.

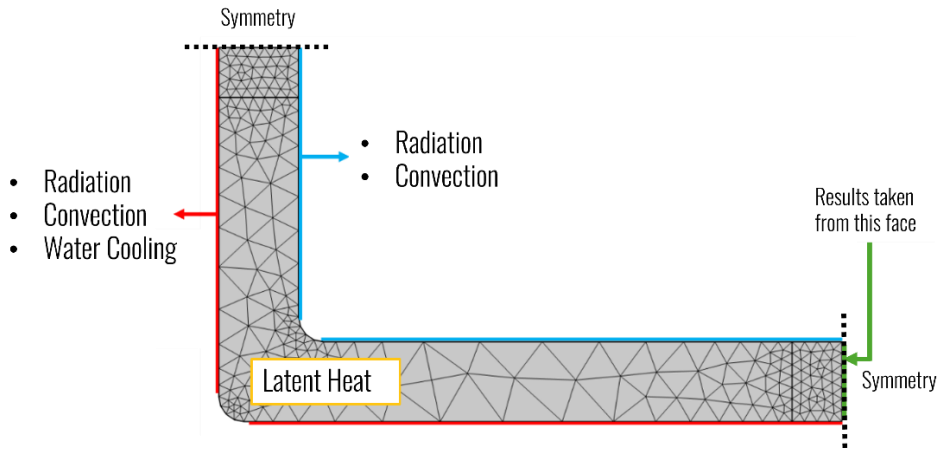


**Fig. 4** Boundary-condition and meshing setup for the numerical model of tube cooling. Future results are taken from average along the face indicated

**Obr. 4** Okrajové podmínky a nastavení sítě pro numerický model chlazení trubek. Budoucí výsledky jsou převzaty z průměru podél vyznačené plochy

Hutnické listy – *Metallurgical Journal*
Speciální vydání / Special Issue, roč. / vol. LXXIX
ISSN Online: 3029-8350

### 3.3 Heat Transfer Coefficients

The modelling of heat extraction within the cooling section relies on a detailed description of the heat transfer coefficients (HTCs) associated with both water cooling and radiative-convective losses. For water cooling, eight cooling banks are modelled, with each capable of operating in four distinct modes ranging from 'off' to high-pressure conditions or additional nozzles being activated. Water pressure is linked to nozzle flow rate via an industrially derived empirical relationship, which then determines the variable heat transfer coefficient, $H_{water}$, used to simulate water cooling.

**Fig. 5A** illustrates an example of the water-cooling heat transfer coefficient applied over time. The water cooling coefficients were derived from fitting to industrial pyrometer readings, where the range of values are consistent with those reported in the literature, which can range from 400 W/m²°C to 3500 W/m²°C in similar systems [16-18]. For the flow rates and temperature ranges anticipated in this production process, Viscorova et al indicated that the heat transfer coefficient should be within the 1000 W/m²°C to 2000 W/m²°C range [17].

Radiative and convective heat losses are treated separately, with the heat transfer coefficient used for radiation, $H_{rad}$, expressed through an emissivity-based surface to ambient radiation formula (Eq. (2)), where emissivity, ε, is 0.6. Convection, $H_{conv}$, (Eq. (3)) is described using an empirical relationship dependent on roll speed, R, and surface temperature [19]. Dry surfaces are modelled using the sum of both radiative and convective heat transfer coefficients.

$$H_{rad} = \varepsilon \cdot k \cdot (T^2 + T_{atm}^2) \cdot (T + T_{atm}) \tag{2}$$

$$H_{conv} = 5.5 \cdot R^{0.926} + \frac{(-3038 + 0.954 \cdot T + 2.14 \cdot 10^{-8} \cdot T^4)}{T - 20} \tag{3}$$

$$H_{dry} = H_{rad} + H_{conv} \tag{4}$$

**Fig. 5B** shows the temperature dependent $H_{dry}$ coefficients for both the inner and outer walls. For the outer wall $H_{dry}$ value, a fitting parameter is added to the radiative and convective components, resulting in higher cooling intensities than the inner wall. Published values for these mechanisms span from 50 W/m²K to 150 W/m²K [3], aligning well with the model's parameters.

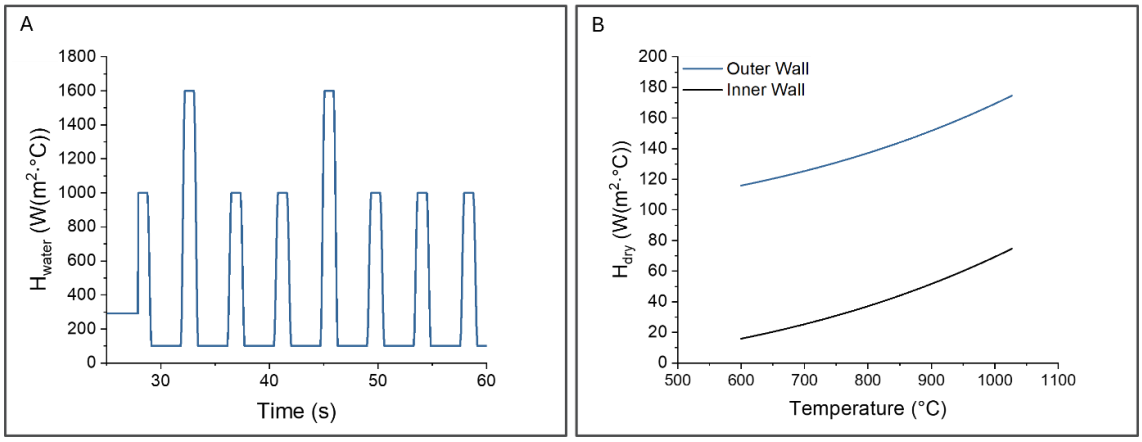


**Fig. 1** Heat-transfer coefficients for (A) water cooling and (B) radiative-convective heat exchange applied in the cooling model

**Obr. 5** Koeficienty přenosu tepla pro (A) vodní chlazení a (B) radiačně-konvekční výměnu tepla použité v chladicím modelu

Hutnické listy – *Metallurgical Journal*
Speciální vydání / Special Issue, roč. / vol. LXXIX
ISSN Online: 3029-8350

**Fig. 6A** illustrates an example through-thickness thermal gradient that develop during cooling. It can be seen that significantly faster cooling is experienced at the surface and progressively slower cooling are seen towards the tube centre (inner wall). Near-surface regions typically cool more rapidly, promoting finer ferrite grains and higher strength, however the surfaces are more prone to the risk of bainite formation. The centre experiences slower cooling and correspondingly coarser ferrite-pearlite microstructures. This through-thickness heterogeneity must be considered when designing cooling strategies and whilst predicting mechanical performance. In **Fig. 6A,** Industrial pyrometer readings are superimposed over the model predictions to illustrate the agreement between the model and measured values.

**Fig. 6B** shows the agreement between the predicted and average measured cooling rig exit temperature for twelve industrial cooling strategies. The error bars indicate a 5% error that may occur in the pyrometer measurement industrially from steam interference, where 5% is estimated from the results of Trofimov et al [20]. It is well known that pyrometer readings can be strongly influenced by steam and surface condition, and the error in measurement can be as extreme as ± 100 °C [21, 22].

The model predicts with a root mean square error (RMSE) accuracy of 23.6 °C, with most data points agreeing with the industrial pyrometer readings. The low accuracy of the pyrometer readings makes it a less reliable metric for model fitting. As a result, the HTC values have been fitted to mechanical property predictions. A greater quality thermal prediction could be made with a more complex cooling model that accounts for more factors. However, the current model attempts to simplify the cooling due to a lack of available knowledge regarding the water-steel interface, water behaviour, water temperature and surface/oxide condition.

To avoid the difficulties of achieving an accurate thermal profile, the heat transfer coefficients used were fitted to mechanical property data as opposed to pyrometer readings. The quality of these mechanical property predictions will be discussed later. In the next sections, the phase transformation and mechanical property predictions will be discussed.

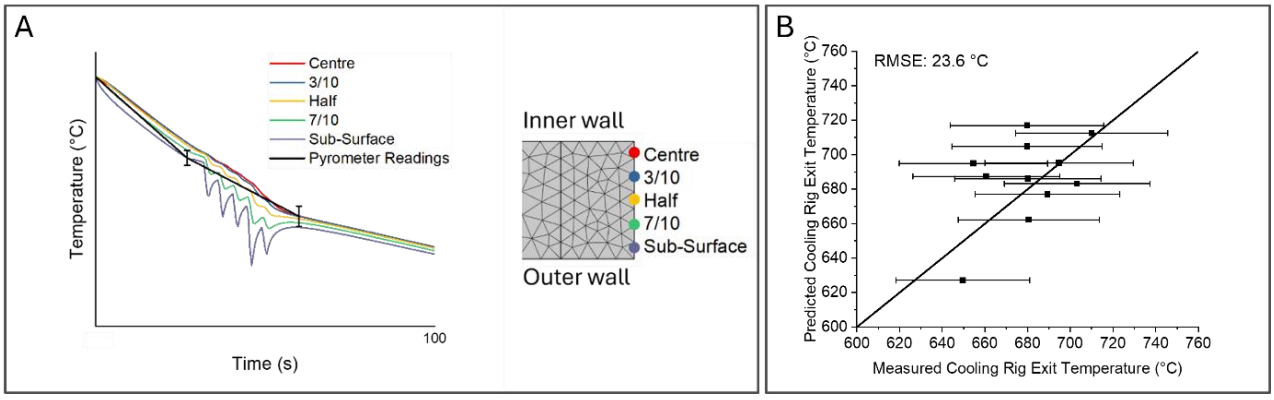


**Fig. 2** (A) Example through thickness temperature profiles during cooling. (B) Predicted against measured cooling rig exit temperature

**Obr. 6** (A) Příklad teplotních profilů v tloušťce materiálu během ochlazování. (B) Porovnání predikované a naměřené teploty na výstupu z chladicího zařízení

Hutnické listy – *Metallurgical Journal*
Speciální vydání / Special Issue, roč. / vol. LXXIX
ISSN Online: 3029-8350

### 3.4 Phase Transformation Model

Once a thermal model is established, to make predictions of grain size and mechanical properties, a phase transformation model is necessary to establish a prediction of the formation of 40% ferrite. The phase transformation model used in this study integrates thermodynamic and kinetic data of ferrite formation to establish the phase fractions formed throughout transformation.

**Fig. 7A** shows schematic of the austenite decomposition via a continuous cooling transformation (CCT) diagram produced by JMatPro that illustrates the onset of ferrite, pearlite and bainite formation under various cooling rates. The imposed cooling profile, plotted in red, intersects the ferrite transformation region at the point where 40% ferrite is formed, denoted as $T_{40\%}$. This temperature is central to predicting the subsequent grain size and strength predictions.

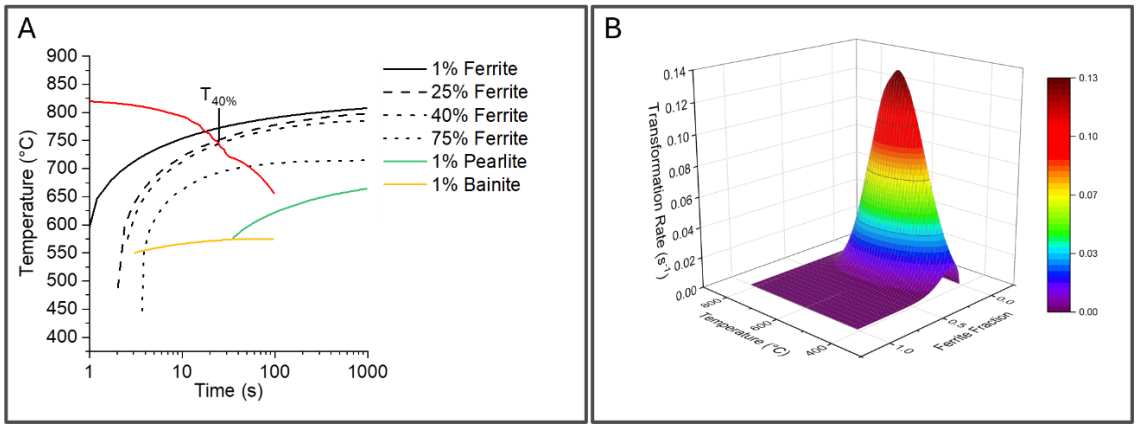


**Fig. 3** (A) A continuous cooling transformation (CCT) diagram with superimposed example cooling profile. (B) Temperature and phase fraction dependent transformation rates predicted by JMatPro

**Obr. 7** (A) CCT diagram kontinuálního ochlazování s příkladem chladicího profilu. (B) Rychlosti fázových transformací v závislosti na teplotě a fázovém podílu predikované programem JMatPro

The thermal behaviour is translated into a phase transformation prediction using JMatPro transformation rate data, shown in **Fig. 7B.** The current timestep ferrite phase fraction, $F_{\alpha\ new}$, is calculated based on the transformation rate, $\Delta F_\alpha$, which is based on the temperature and the previous time steps fraction transformed, $F_\alpha$. The equation used to calculate the ferrite fraction at each time step is shown in Eq. (5).

$$F_{\alpha\,new} = F_\alpha + dt \cdot \Delta F_\alpha \tag{5}$$

Once the phase fraction is established, the subsequent step is to translate the 40% ferrite formation temperature into a grain size prediction and hence a mechanical property prediction. This is done via the following steps.

To quantify the driving force for ferrite transformation, the model calculates the undercooling ($\Delta T_{40\%}$) relative to the ferrite-austenite equilibrium temperature, $A_{e3}$, which is 822 °C for this alloy.

$$\Delta T_{40\%} = A_{e3} - T_{40\%} \tag{6}$$

To predict final mechanical properties, the final ferrite grain size, $d_\alpha$, needs to be known. $d_\alpha$ is calculated using Eq. (1).

Hutnické listy – *Metallurgical Journal*
Speciální vydání / Special Issue, roč. / vol. LXXIX
ISSN Online: 3029-8350

The solid solution strengthening contribution is calculated using the following equation [23] (where alloying additions are given in weight percentage):

$$\sigma_{SS} = 84 \cdot Si + 32 \cdot Mn + 680 \cdot P + 43 \cdot Ni + 38 \cdot Cu \quad (7)$$

The predicted ferrite grain size and solid-solution term are then combined with a Hall-Petch formula to estimate the yield strength, $\sigma_{YS}$, where $\sigma_0$ is the friction stress of iron [24, 25]. The ultimate tensile strength, $\sigma_{UTS}$, is calculated using a yield strength to ultimate tensile strength conversion value, J, based on industrial data.

$$\sigma_{YS} = \sigma_{SS} + \sigma_0 + 18.1 \cdot d_\alpha^{-0.5} \quad (8)$$

$$\sigma_{UTS} = J \cdot \sigma_{YS} \quad (9)$$

These relations establish a direct link between thermal profile, microstructure and final mechanical properties.

The incorporated JMatPro-based phase transformation model provides a comprehensive description of ferrite formation during multi-stage controlled cooling. As shown in **Fig. 8**, transformation behaviour is sensitive to the thermal history, with ferrite nucleation and growth occurring across a range of temperatures depending on the cooling strategy chosen. This variability directly influences the final ferrite grain size and consequently, the mechanical properties discussed in the preceding subsection.

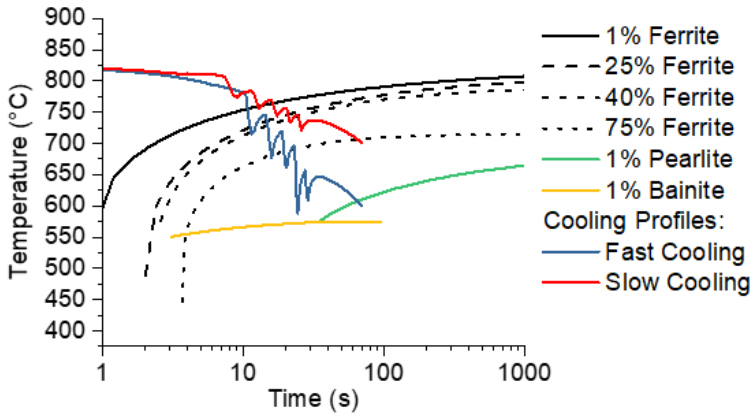


**Fig. 4** JMatPro produced CCT with superimposed 'fast' and 'slow' thermal profiles

**Obr. 8** JMatPro modul pro znázornění CCT diagram s možností překrytí "rychlých" a "pomalých" teplotních profilů

The CCT diagram in **Fig. 8** includes several ferrite start curves (0-75% transformation) together with pearlite and bainite start curves. Two representative cooling profiles, one 'fast' and one 'slow' simulated thermal profiles are superimposed to illustrate maxima and minima cooling strategies. Under 'fast' cooling, the thermal profile is predicted to cross the 40% ferrite formation temperature at approximately 715 °C, resulting in an undercooling of around 107 °C, leading to the formation of fine ferrite grains of around 4.7 μm.

Conversely, 'slow' cooling intersects the ferrite region at higher temperatures (≈ 740 °C), promoting coarser ferrite (≈ 5.2 μm) due to lower undercoolings (≈ 82 °C) and hence lower nucleation rates.

Hutnické listy – *Metallurgical Journal*
Speciální vydání / Special Issue, roč. / vol. LXXIX
ISSN Online: 3029-8350

In addition to differences imposed by the overall cooling rate, local variations in transformation behaviour are expected through the thickness of industrially processed product, which will lead to a through thickness distribution of grain sizes and hence strengths.

By integrating experimentally derived CCT data with the transformation model, the methodology enables prediction of microstructural evolution for cooling strategies. The combination of transformation kinetics, grain-size estimation, and composition-based strengthening models forms a consistent foundation for the strength predictions discussed in the next sections of the article.

## 4. Results and Discussion

### 4.1 Model Validation

The model was validated against twelve industrial data points representatives of commercially produced structural steel tube, covering a wide range of cooling profiles, geometries, wall thicknesses and annealing conditions. The comparison between predicted and measured average ultimate tensile strength is shown in **Fig. 9**. The predicted strength is taken from the measurement point is indicated in **Fig. 4,** where the inner and outer 1 mm are excluded from measurement. The Y-axis error bars are indicative of the error present in Eq. (1) [15]. The X-axis error bars indicate the ranges of industrial measurements. Model predictions for UTS align closely with industrial measurements, yielding an RMSE of 6.5 MPa. These results demonstrate that the integrated transformation and grain-size modelling approach provides accurate predictions for the S355 grade studied. The close clustering of data points around the one-to-one line highlights the ability of the model to reliably capture the influence of cooling strategy on ferrite transformation and resulting strength. The validation also confirms that JMatPro-based phase transformation predictions provide adequate fidelity for grain-size estimation across the tested conditions. With this level of accuracy, the model can be confidently used as a tool to support the selection and optimisation of processing parameters in industrial tube production.

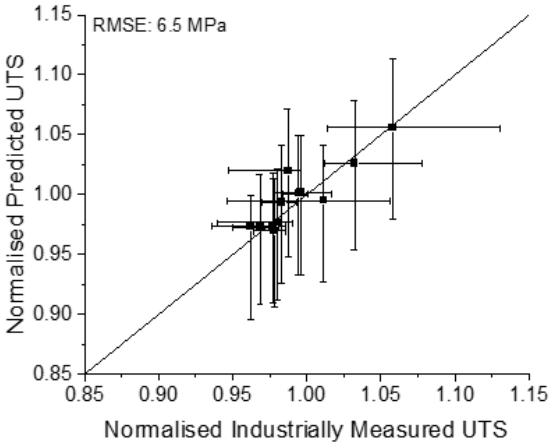


**Fig. 5** Model validation plot comparing normalised predicted UTS with normalised industrially measured UTS (RMSE = 6.5 MPa)

**Obr. 9** Graf ověření modelu porovnávající normalizovanou predikovanou mez pevnosti v tahu s normalizovanou průmyslově naměřenou mezí pevnosti v tahu (RMSE = 6,5 MPa)

The measured normalised yield and ultimate tensile strengths are plotted, in **Fig. 10**, against the predicted values, with bainite formation predictions shown.

Hutnické listy – *Metallurgical Journal*
Speciální vydání / Special Issue, roč. / vol. LXXIX
ISSN Online: 3029-8350

The predicted values include twenty-two cooling strategies, with three annealing temperatures, two tube geometries and three strip thicknesses. These cooling strategies are deemed to be representative of the full range of industrial processing conditions. Industrial data includes multiple measurements per tube.

It can be seen that the model predicts the mechanical properties reasonably well for a wide range of products, encompassing the UTS values for most tubes produced commercially. The UTS predictions span from 0.94 to 1.05, encompassing almost the full range of UTS values produced by ferrite-pearlite microstructures. For yield strengths, the industrial data is more scattered than the UTS data. Due to the model using a linear yield strength to UTS ratio, Eq. (9), a lower range of yield strengths are predicted by the model. However, the model still encompasses around 60% of the yield strength range. Given a set of processing parameters, the model is capable of providing a reasonable prediction of the final mechanical properties in a wide range of S355 tube products.

The model also predicts the onset of bainite formation well. The onset of bainite formation marks the upper limit for the predictive range of the model, since no bainite strengthening contribution is calculated. The model conditions where bainite forms align with the point at which the linear yield to UTS ratio breaks down industrially, which is representative of the transition from ferrite-pearlite to ferrite-bainite microstructures, this is marked by the box in **Fig. 10**. The accurate prediction of bainite formation supports the assumptions made for the thermal and phase transformation models and demonstrates that they are sufficient for the current needs. The ability to predict bainite formation allows for appropriate processing conditions to be selected to form high strength ferrite-pearlite microstructures, which will be discussed in the subsequent section.

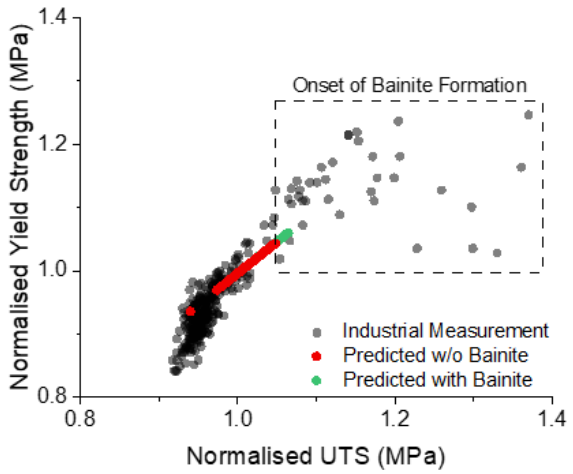


**Fig. 10** Normalised yield strength against normalised ultimate tensile strength with both industrial data and model predictions plotted. The onset of bainite formation is indicated

**Obr. 10** Normalizovaná mez kluzu v závislosti na normalizované mezní pevnosti v tahu; v grafu jsou znázorněna jak průmyslová data, tak modelové predikce. Je vyznačen počátek tvorby bainitu

### 4.2 Optimisation of Cooling Parameters

Using the validated framework, a parametric study was conducted to assess the levels of strength improvement possible using current industrial equipment. Twenty two cooling strategies with varying cooling bank configurations, nozzle configurations and pressures were tested for a single product geometry annealed at 900 °C.

Hutnické listy – *Metallurgical Journal*
Speciální vydání / Special Issue, roč. / vol. LXXIX
ISSN Online: 3029-8350

Three example cooling strategies are shown in **Fig. 11A** alongside the normalised UTS strengths predicted from each cooling strategy in **Fig. 11B**. The parametric study demonstrates that a 5% increase in strength is achievable for this specific geometry through optimised parameter selection.

| | Low | Medium | High |
|---|---|---|---|
| Bank 1 | Off | Off | Off |
| Bank 2 | Off | On | On |
| Bank 3 | Off | On | On |
| Bank 4 | Off | On | On |
| Bank 5 | Off | On | On |
| Bank 6 | Off | On | On |
| Bank 7 | Off | On | On |
| Bank 8 | Off | Off | Off |
| High Pressure Valve 1 | Off | On | On |
| High Pressure Valve 2 | Off | On | On |
| Bank 1 Extra Nozzles | Off | Off | Off |
| Bank2 Extra Nozzles | Off | Off | Off |
| Bank3 Extra Nozzles | Off | On | On |
| Bank4 Extra Nozzles | Off | On | On |
| Bank5 Extra Nozzles | Off | Off | On |
| Bank6 Extra Nozzles | Off | Off | On |
| Bank7 Extra Nozzles | Off | Off | Off |
| Bank8 Extra Nozzles | Off | Off | Off |

| Tube Height (mm) | Tube Width (mm) | Wall Thickness (mm) | Annealing Temperature (°C) |
|---|---|---|---|
| 150 | 250 | 10 | 900 |

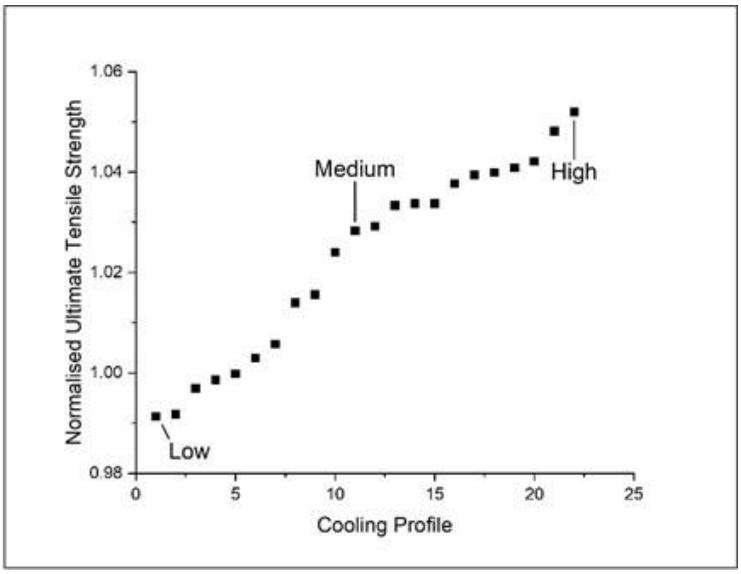


**Fig. 11** Effect of cooling-parameter configurations on the predicted normalised ultimate tensile strength

**Obr. 11** Vliv nastavení parametrů chlazení na predikovanou normalizovanou mez pevnosti v tahu

The present FE model offers the opportunity to map the processing capabilities of the current manufacturing routes whilst providing manufacturers the opportunity for process optimisation and control.

## 5. Conclusions

During this study, a thermal FE model which utilises thermodynamic and phase transformation modelling with integrated empirical relationships to predict microstructural features (ferrite grain size) and mechanical properties has been established.

The model has been developed to replicate a typical structural steel tube production process and simulates from annealing via controlled cooling through to the run-out table. The present study provides greater understanding of the thermal histories generated throughout controlled cooling and the resultant mechanical properties.

The key findings from this study are as follows:

- The model generates thermal profile predictions that align closely with industrial pyrometer measurements. Processing parameter inputs, including processing parameters, product geometry and chemical composition can be varied to produce a range of thermal profile predictions. The cooling bank exit temperature is predicted with an RMSE accuracy of ± 23.6 °C.
- The model uses thermodynamic, phase transformation prediction and empirical relationships to establish an accurate prediction of final mechanical properties, namely ultimate tensile strength. An RMSE accuracy of ± 6.5 MPa.

Hutnické listy – *Metallurgical Journal*
Speciální vydání / Special Issue, roč. / vol. LXXIX
ISSN Online: 3029-8350

- The model predictions for the onset of bainite formation are aligned with industrial data. Allowing for processing parameters to selected to avoid ferrite-bainite microstructures.
- The high accuracy of the UTS predictions, substantiates the methodology used for microstructural and phase transformation modelling.
- A parametric study was conducted to assess the potential for strength improvements via optimised processing parameter selection. A select finding from this work is that by adjusting cooling bank parameters, a potential 5% strength uplift can be achieved, this value will vary between products and will be investigated further.

## Reference

[1] Institution, B.S., Hot finished structural hollow sections of non-alloy and fine grain steels. 2006, BSI.
[2] Langbauer, R., et al., Investigation of the temperature distribution in seamless low-alloy steel pipes during the hot rolling process. Advances in Industrial and Manufacturing Engineering, 2021. **2**: p. 100038.
[3] Chen, D., et al., Online cooling system and improved similar self-adaptive strategy for hot-rolled seamless steel tube. ISIJ International, 2021. **61**(7): p. 2135-2142.
[4] Souza, J.L.F., M. Ziviani, and J.F.A. Vitor, Mathematical modelling of tube cooling in a continuous bed. Applied Thermal Engineering, 2015. **89**: p. 80-89.
[5] Gomes, D.F., R.P. Tavares, and B.M. Braga, Mathematical model for the temperature profiles of steel pipes quenched by water cooling rings. Journal of materials research and technology, 2019. **8**(1): p. 1197-1202.
[6] Landfahrer, M., et al., Characterization of the temperature distribution on steel tubes for different operating conditions in a reheating furnace using CFD and three different measuring methods. Applied Thermal Engineering, 2018. **133**: p. 39-48.
[7] Raič, J., et al., Modelling of the cooling process of steel tubes in a rake type cooling bed. Applied Thermal Engineering, 2020. **169**: p. 114895.
[8] Landfahrer, M., et al., Development of a numerically efficient CFD model to predict transient temperature distribution of mother tubes moving translative and rotative through a gas fired furnace. Applied Thermal Engineering, 2017. **123**: p. 290-300.
[9] Manohar, P.A. and T. Chandra, Continuous cooling transformation behaviour of high strength microalloyed steels for linepipe applications. ISIJ international, 1998. **38**(7): p. 766-774.
[10] Amirjani, N., M. Ketabchi, M. Eskandari, and M. Hizombor, Effect of cooling rate and finish rolling temperature on structure and strength of API 5LX70 linepipe steel plate. Journal of Materials Engineering and Performance, 2020. **29**: p. 4275-4285.
[11] Souza, J.L.F., et al., Experimental Measurementt of Internal Temperature of a Tube in Cooling on a Bed of Passage, Continuous Under Natural Convection. Thermal Engineering, 2019. **18**(2): p. 06-12.
[12] Brunbauer, S., et al., Residual stress and microstructure evolution in steel tubes for different cooling conditions – Simulation and verification. Materials Science & Engineering A, 2019. **747**: p. 73-79.
[13] Tovee, J.P., Microstructural Influence On The Effects Of Forward And Reverse Mechanical Deformation In Hsla X65 And X80 Linepipe Steels, in Department of Metallurgy and Materials. 2014, University of Birmingham.
[14] Militzer, M., R. Pandi, and E.B. Hawbolt, Ferrite nucleation and growth during continuous cooling. 1996. **27**: p. 1547-1556.
[15] Dixon, N., C. Slater, J. Du, and C. Davis, Determination of Final Ferrite Grain Size During Multiple-Stage Controlled Cooling of Low-Carbon, Low-Alloy Steels. Metals, 2025. **15**(9): p. 956.
[16] Wendelstorf, J., K.-H. Spitzer, and R. Wendelstorf, Spray water cooling heat transfer at high temperatures and liquid mass fluxes. International Journal of heat and mass transfer, 2008. **51**(19-20): p. 4902-4910.
[17] Viscorova, R., R. Scholz, K. Spitzer, and J. Wendelstorf, Spray water cooling heat transfer under oxide scale formation conditions. Advanced Computational Methods in Heat Transfer IX, 2006. **53**: p. 163-172.
[18] Wang, H., W. Yu, and Q. Cai, Experimental study of heat transfer coefficient on hot steel plate during water jet impingement cooling. Journal of Materials Processing Technology, 2012. **212**(9): p. 1825-1831.
[19] Edalatpour, S., A. Saboonchi, and S. Hassanpour, Effect of phase transformation latent heat on prediction accuracy of strip laminar cooling. Journal of Materials Processing Technology, 2011. **211**(11): p. 1776-1782.
[20] Trofimov, A.A., et al., Infrared thermometry in high temperature materials processing: influence of liquid water and steam. Quantitative InfraRed Thermography Journal, 2023. **20**(3): p. 123-141.
[21] Huang, Y., et al., Experimental investigation on the effects of particulate interference on radiation thermometry. International Journal of Heat and Mass Transfer, 2024. **224**: p. 125350.
[22] Sugiura, M., et al., Two-color method for steel temperature measurement unaffected by water-induced obstructions. ISIJ International, 2023. **63**(2): p. 346-353.
[23] Gladman, T., Physical metallurgy of microalloyed steels. (No Title), 1997.
[24] Petch, N., The upper yield stress of polycrystalline iron. Acta Metallurgica, 1964. **12**(1): p. 59-65.
[25] Baker, T.N., Microalloyed Steels. Ironmaking and Steelmaking, 2016. **43**(4): p. 267 - 307.

STEELSIM 2025
2-4 SEPTEMBER · TŘINEC · CZ

Hutnické listy – *Metallurgical Journal*
Speciální vydání / Special Issue, roč. / vol. LXXIX
ISSN Online: 3029-8350

# High Carbon Wire Cracking during Cold Forming Process

# Vznik trhlin vysokouhlíkového drátu při tváření za studena

**Marcel Janošec[1], Richard Fabík[1], Markéta Smetanová[1], Marek Machetanz[1], Zoltán Pozbai[2]**

[1] ŽDB DRÁTOVNA a.s., Jeremenkova 66, 735 51, Bohumín, Czech Republic. *Corresponding author: marcel.janošec@zdb.cz
[2] D&D Drótáru Zrt., Sajószigeti u.4., H-3527, Miskolc, Hungary

## Abstract

*The article focuses on the issue of crack formation in high-carbon steel wires during the cold upsetting process. This operation ensures the fixation of wire ends in prestressing systems, particularly in systems for concrete tower structures of wind turbines. FEM simulations, physical experiments, and metallographic analyses were used to analyse the causes of these defects. Computer simulations confirmed the presence of unfavourable tensile stresses occurring in the upset parts of the wires. This finding led to the design of a modified tool. In the new tool, tensile components are minimized and compressive stresses prevail in the deformed zone, which are safer in terms of plasticity and the risk of material failure. Physical simulations were carried out on samples with varying levels of initiation defects. It was confirmed that defect depth and the magnitude of the applied deformation influence the resulting crack opening. Based on these results, an adjustment of the sample height was proposed for the physical simulation. The results of the study contribute to a deeper understanding of the mechanisms of material failure during forming and may serve as a basis for improving tool design and increasing the reliability of the manufacturing process.*

***Keywords**: wire, cracking, cold forming, FEM, metallography*

## Abstrakt

*Článek se zabývá problematikou vzniku trhlin v drátech z uhlíkové oceli během procesu tváření za studena. Tato operace zajišťuje upevnění konců drátů v předpínacích systémech, zejména v systémech pro betonové stožárové konstrukce větrných turbín. K analýze příčin těchto vad byly použity simulace metodou konečných prvků (FEM), fyzikální experimenty a metalografické analýzy. Počítačové simulace potvrdily přítomnost nepříznivých tahových napětí v deformovaných částech drátů. Tento poznatek vedl k návrhu upraveného nástroje, v němž jsou tahové složky minimalizovány a v deformované zóně převládají tlaková napětí, jež jsou bezpečnější z hlediska plasticity a rizika selhání materiálu. Fyzikální simulace byly provedeny na vzorcích s různou hloubkou počátečních vad. Bylo potvrzeno, že hloubka vady a velikost aplikované deformace ovlivňují výsledné otevření trhliny. Na základě těchto zjištění byla navržena úprava výšky vzorku pro fyzikální simulace. Výsledky studie přispívají k hlubšímu pochopení mechanismů selhání materiálu během tváření a mohou sloužit jako podklad pro optimalizaci konstrukce nástrojů a zvýšení spolehlivosti výrobního procesu.*

***Klíčová slova:** drát, vznik trhlin, tváření za studena, metoda konečných prvků (FEM), metalografie*

## 1. Introduction

High-carbon steel wire represents a key material for the production of individual segments or more complex units of prestressed concrete, where it serves as the carrier of tensile stress transferred into the concrete structure. These steel wires are used, for example, in the manufacture of prefabricated floor panels, railway sleepers, and in the construction of bridge structures [1, 2].

Hutnické listy – *Metallurgical Journal*
Speciální vydání / Special Issue, roč. / vol. LXXIX
ISSN Online: 3029-8350

For many years, the range of stabilized steel wires has also been used to reinforce the segmental towers of wind turbines. Historically, their construction was based primarily on steel (tubular) shells. However, concrete towers demonstrate higher resistance to extreme loads, particularly in taller structures [3].

Steel tubular towers higher than 85 m are no longer able to provide adequate behaviour under vibrations induced by the wind turbine. The blade size of the wind turbine and the tower height represent essential parameters related to turbine performance. Since the energy generated from wind is a function of the cube of the wind speed, even a small increase in wind velocity can significantly improve the turbine's output [4].

Non-hybrid tower systems consist of prefabricated concrete segments that, once assembled, are subsequently prestressed through openings using post-tensioning systems [5]. This method, referred to as "post-tensioned," provides high resistance to bending and tensile loads, ensures the connection of all segments into a single static unit, and also allows the tower to be prestressed directly at the installation site.

From the perspective of wire material characteristics, these can be described as steels with a higher (essentially eutectoid) carbon content. The required properties [6] are achieved through a combination of chemical composition and wire manufacturing technology, where the wires are cold-drawn or thermomechanically processed in the final stages. This production method guarantees high strength characteristics along with low relaxation, which is desirable for such applications [7, 8].

With constant deformation of non-stabilized wires over time, their stress in the "concrete" system decreases, which negatively affects the structural properties and may ultimately lead to structural damage or even catastrophic failure [9].

The aim of this article was to analyse the causes of crack formation occurring in the upset areas of high-carbon wires during or after the cold forming process. This type of end modification ensures the fixation of wires in prestressing systems and, alongside the required wire properties, represents—within this context—a key parameter for the overall functionality of the system.

## 2. Evaluation of the Geometry of Upset Wire Sections and Tool Design for FEM Simulation

As part of the evaluation of crack occurrence in upset wire sections, a computer simulation was carried out with the aim of better understanding the deformation and stress conditions occurring during this operation. However, the modelling itself was preceded by the need to define the tool shape, whose geometry was not known. Nevertheless, upset wires without cracks were available (if a defect occurs in the upset part, the shape is naturally modified; from this perspective, it was desirable to use upset wires free of defects).

Using a Keyence device [10], which enables fast and accurate measurement of complex shapes through optical scanning, the geometry of the upset wire section was measured. This measurement, which essentially replaces gauging with conventional measuring instruments, was carried out in six differently oriented planes, with the outputs of all six evaluations taken into account during the tool design. The measured values in a selected plane are shown in **Fig. 1**.

Hutnické listy – *Metallurgical Journal*
Speciální vydání / Special Issue, roč. / vol. LXXIX
ISSN Online: 3029-8350

Based on these measurements, a tool—or rather a pair of tools (upper and lower die)—was designed. The shape of the upper part reflected the fact that the upset material is in contact with the upper tool only up to a certain stage of the upsetting process. This was recognizable through differences in curvature (for the demonstrated cross-section, this is more clearly visible on the right-hand side of **Fig. 1**, see the R3.135 and R6.022 interfaces). This location therefore represents the point where the material-tool contact ends (or begins).

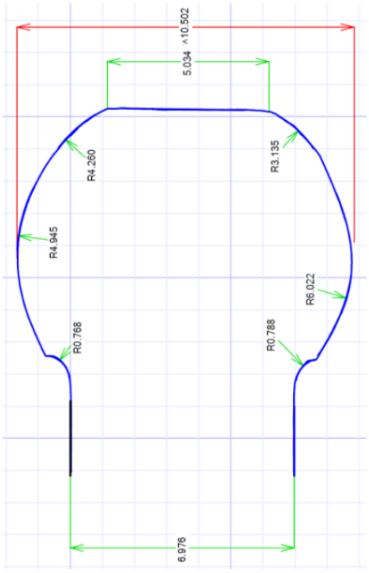


**Fig. 1** Measurement results of the geometry of the upsetted wire section

**Obr. 1** Výsledky měření geometrie zúženého úseku drátu

## 3. Physical Simulation of the Upsetting Process

The industrially applied process of wire-end upsetting is often physically simulated in order to verify the potential occurrence of initiation defects present in the wire. This approach can replace, for example, metallographic examination of cross-sections and is faster compared to microscopic techniques (since the samples do not need to be fixed into mounts, ground, or otherwise laboriously prepared for metallographic evaluation).

This process is usually carried out on multi-purpose hydraulic presses, where samples taken from the wire are upset using “dies” that either correspond to or closely approximate the tools used in production. The same approach was taken in this case.

In total, four series of samples were prepared from the manufactured wires (always three samples per series, i.e., 4x3=12 samples). The selection of input material for individual samples was based on previously performed metallographic evaluations. Thus, wire locations containing initiation defects of varying but pre-determined extent was selected. The last series of samples was prepared from defect-free locations.

All 12 cylindrical samples were prepared by turning so that the cylinder bases were perpendicular to the longitudinal axis of the sample. The intention was to prepare samples with a uniform length of 15 mm. The actual length of individual samples is documented in the graph in **Fig. 2a**. It is evident that one of the samples had a significantly lower height compared to the others. All samples were then cold-deformed by upsetting (see **Fig. 2b**).

Hutnické listy – *Metallurgical Journal*
Speciální vydání / Special Issue, roč. / vol. LXXIX
ISSN Online: 3029-8350

Considering the practically identical height of the samples after upsetting, the actual height reduction of each sample depended on its initial height dimension (**Fig. 2c**). After the upsetting test, the geometry of all samples, including the width of the observed defects, was measured. Defects in the upset areas were found only in samples numbered 1 to 9 (those with present initiation cracks).

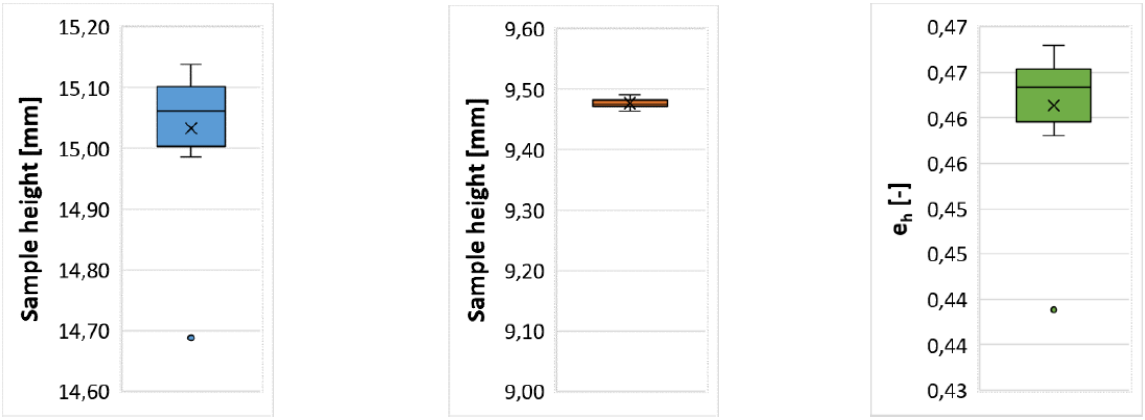


a) before upsetting b) after upsetting c) calculated strain

**Fig. 2** Height and strain of tested samples / **Obr. 2** Výška a deformace testovaných vzorků

## 4. Metallographic Analysis and Results of Defect Width/Depth Measurements

Microstructural evaluation was performed on industrially processed wires in which defects of the upset sections were recorded. Cross-sections were examined in areas beneath the upset part, as well as in other (more distant) locations from the upset area, in order to assess the variability of the initiation crack depth. Sections in these distant locations were also used as "inputs" for preparing samples for physical simulation of the industrial upsetting process. Based on measurements of defect opening width in the upset part and the depth of the initiation defect, relationships were established, as documented in the graph in **Fig. 3**.

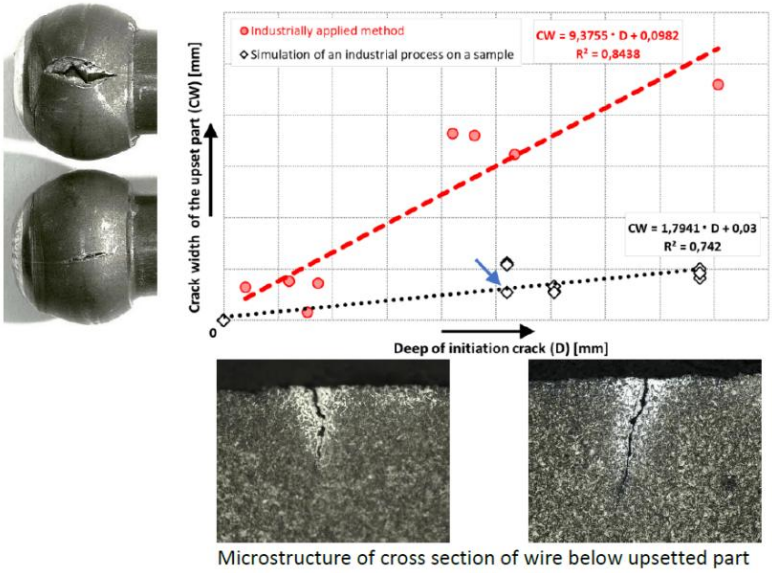


**Fig. 3** Correlation between initial crack depth and crack opening after upsetting

**Obr. 3** Vztah mezi počáteční hloubkou trhliny a jejím rozšířením po tváření

Hutnické listy – *Metallurgical Journal*
Speciální vydání / Special Issue, roč. / vol. LXXIX
ISSN Online: 3029-8350

For both the industrially applied upsetting process and the physically simulated wire upsetting process, the crack opening in the upset section increases with the increasing depth of the initiation defect. In this evaluation, other influences (such as structural heterogeneities, inclusions, grain size, etc. [11, 12]) were not considered. It is evident that the slope of the linear relationship is approximately five times higher for the industrial process compared to the physical simulation. This may partly be related to the different tool shapes or to the lower deformation applied in the simulated process. Measurements of the diameters of upset sections at the point of maximum bulging revealed higher values for the industrially processed wires. The effect of deformation magnitude on crack opening width is also visible in the distribution of a selected data series (indicated by an arrow in the graph in **Fig. 3**). In this case, one of the three samples experienced a lower degree of deformation (in **Fig. 2a** and **Fig. 2c** this is represented by an outlier), which ultimately resulted in a smaller crack opening.

From a practical point of view, it seems more appropriate that the simulation of the industrial upsetting process should, in terms of initiation defect opening, provide results analogous to the industrial process itself. In this sense, a calculation was carried out to determine the actual deformation required during sample upsetting, i.e., what the initial sample dimension should be in order to ensure that the results of the physical simulation approach those achieved in industrial upsetting. This is described by the following equation (1), where "d" represents the maximum diameter (maximum bulging) of the upset sample (a value of 10.5 mm was measured on industrially upset samples), "h0", and "h1" represent the height of the sample before and after deformation, respectively.

$$h_0 = \left[e^{\left(\frac{d-6{,}075}{8{,}691}\right)}\right] \cdot h_1 \ldots . [mm] \tag{1}$$

It is worth noting the character of the microstructure in the vicinity of the initiation cracks. The presence of a ferritic phase in steel of this composition indicates that these defects originated before hot rolling. During the drawing of the rolled wire, the existing surface defects are modified. For a crack that is characterized by a low width-to-depth ratio, i.e., a ratio lower than one, it is recommended to remove the defect from the wire before drawing [13, 14].

Cracks of this type (parallel to the loading direction) are associated with surface defects. In addition to these cracks, there also frequently occur cracks inclined at an angle of 45° to the loading direction (**Fig. 4**). These cracks, referred to as shear cracks, are related to the exhaustion of plasticity or the increase in strength due to strain hardening [15]. Their inclination with respect to the loading direction is associated with the maximum shear stress, which, under uniaxial stress conditions, reaches its highest values precisely on planes inclined at 45° to the direction of loading.

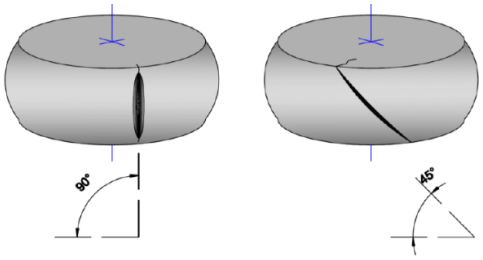


**Fig. 4** Types of cracks occuring during the upsetting process

**Obr. 4** Druhy trhlin vznikajících při procesu tváření

Hutnické listy – *Metallurgical Journal*
Speciální vydání / Special Issue, roč. / vol. LXXIX
ISSN Online: 3029-8350

## 5. FEM Simulation

Mathematical modelling of the upsetting process was carried out using the finite element method, which enables a detailed analysis of the stress–strain state. The FE analysis was performed as a 2D axisymmetric task without considering the generation of deformation heat. To describe the material's deformation behaviour, a rigid–plastic model was used. For the description of the yield strength of the material, a model based on Spittel's equation (2) was developed.

The constants in the equation were determined from a series of tensile tests performed on the specific material at room temperature:

$$\sigma_y = 2163 \cdot e^{0.056} \quad ....[MPa] \tag{2}$$

The Tresca friction model was applied, with the friction factor "m" set to 0.6, which corresponds to cold forging without the use of lubrication [16].

Within the simulations, two variants of cold heading were carried out. The purpose of the first variant, based on previously performed measurements of upset wire shapes, was to evaluate the stress–strain states during the industrial process. Using this knowledge, the forming process was then optimized in order to eliminate the occurrence of unfavourable tensile tangential stresses in the surface layers of the wire.

Tangential stresses act in the polar coordinates used in this 2D model in the direction of angle α. If these stresses are tensile, they cause the opening of longitudinal defects that are already present in the drawn wire, originating from hot rolling or steel casting (see decarburization in the vicinity of defects visible in **Fig. 3**, which indicates that these flaws existed in the material before heating). Conversely, if these stresses are compressive, they can lead to complete or at least partial forging welding of already opened defects (the degree of integrity of such a weld depends on the extent of surface contamination of the defect by original oxides originating from the hot rolling stage). If these stresses exceed the strength of the wire, they cause the formation of cracks (most often shear cracks) after a certain level of deformation is reached, even without the presence of an initial defect.

In the manner described above, a modified shape of the upper and lower tool was gradually developed. The model shape of the wire termination for the current variant, as well as the newly designed shape, including the strain intensity field at the end of forging, are shown in **Fig. 5**. As can be seen from the **Fig. 5**, in order to ensure lateral pressure on the head while maintaining its maximum width of 10.5 mm, the newly designed "head" must be slightly smaller than the original (originally 7.7 mm, now 6.8 mm). This results in a higher value of maximum strain intensity, which is 1.40 for the original tools and 1.67 for the new tools. By using a higher input, the same head height could also be achieved for the new tools. Under these conditions, however, the key forging ratio of initial height to initial diameter h0/d0 would exceed the value of 2.5, which in practice often leads to bending of the forging and its collapse during forging (under the current conditions, h0/d0 = 2.42!).

**Fig. 6** shows the results of tangential stress in the key stages of head forging. As expected, the tangential stress when using the modified tools (**Fig. 6b**) just before contact with the die sidewall is lower (+1,493 MPa) than in the case of the original tools (**Fig. 6a**) at the end of forging (+1,590 MPa), mainly due to the use of a flat upper anvil.

Hutnické listy – *Metallurgical Journal*
Speciální vydání / Special Issue, roč. / vol. LXXIX
ISSN Online: 3029-8350

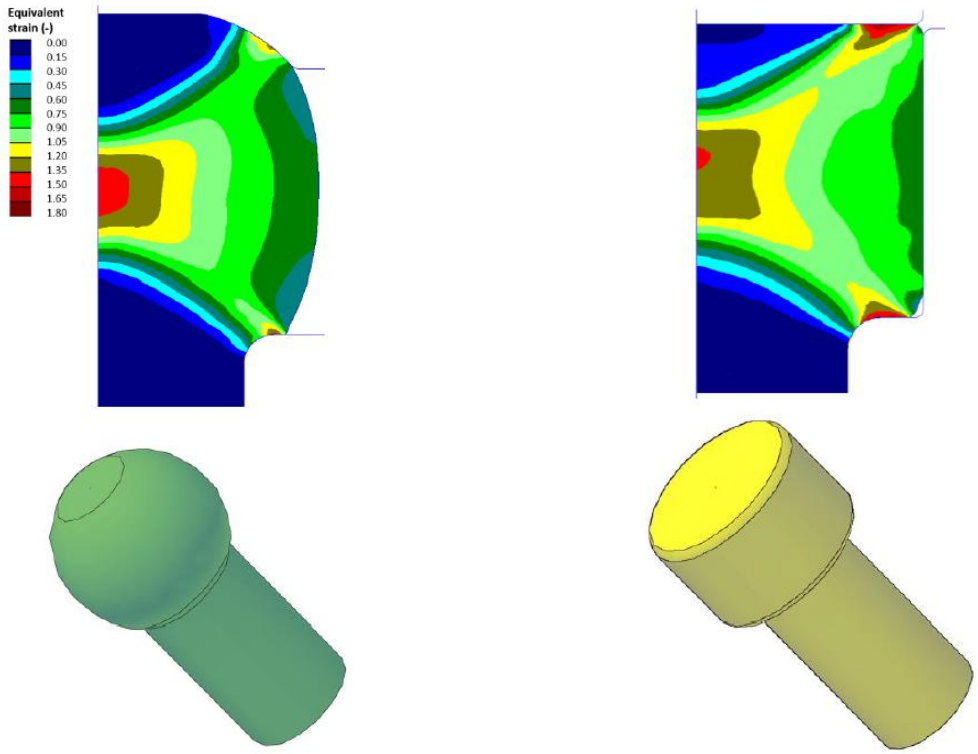


a) current shape b) new shape

**Fig. 5** Distribution of strain intensity and shape of the current vs. newly designed wire termination

**Obr. 5** Rozložení intensity napětí a tvaru stávajícího a nově navrženého zakončení drátu

Once contact with the die sidewall occurs, the region where the highest tensile stress originally appeared is subjected to triaxial compression. The areas of maximum tangential stress shift upward and downward, and the stress values there do not exceed +1,500 MPa for the remainder of the forging process. Contact of the material with the die sidewall in the case of the newly designed tools, however, has a negative impact on the maximum forging force, which increased more than fivefold compared to the original design (from 122 kN to 622 kN).

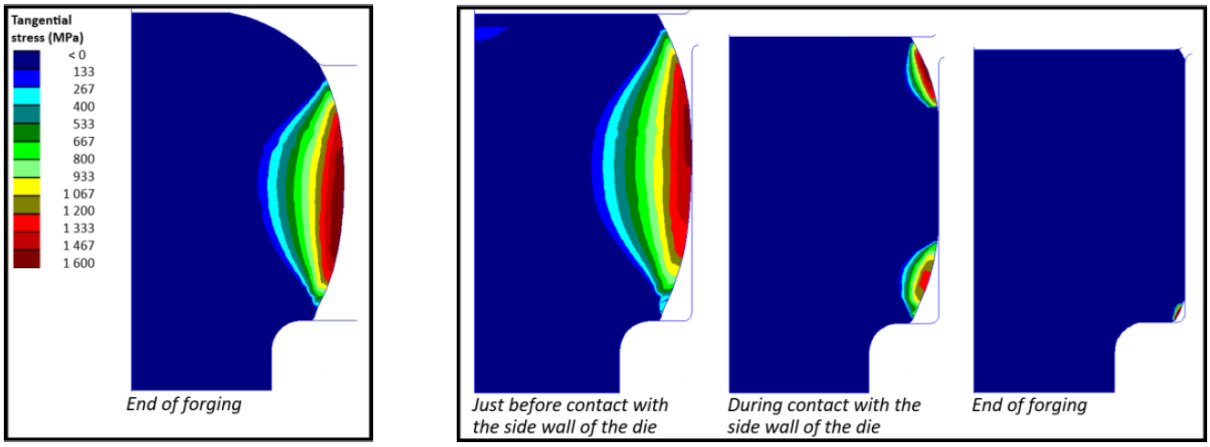


a) current tool design b) new tool design

**Fig. 6** Distribution of tensile tangential stress during forging of the current vs. newly designed wire termination

**Obr. 6** Rozložení tangenciálního tahového napětí při kování stávajícího a nově navrženého zakončení drátu

Hutnické listy – *Metallurgical Journal*
Speciální vydání / Special Issue, roč. / vol. LXXIX
ISSN Online: 3029-8350

## 6. Conclusion

Using FEM simulations, an analysis of stress distribution occurring during the industrial wire upsetting process was carried out. The simulations confirmed the presence of "unfavourable" tensile stresses occurring in selected locations of the upset wire sections.

Based on the conducted evaluations, the tool geometry was subsequently modified so that the newly designed shape would eliminate the occurrence of unfavourable tensile stresses to the greatest possible extent.

Microstructural analysis of industrially processed wires, as well as physical simulations of this process, confirmed that the occurrence of a defect in the upset part of the wire requires the presence of an "initiation" defect. The level of tensile stress reached, in the absence of an "initiation" defect, does not cause material failure manifested by this type of defect (a crack parallel to the loading direction – see Fig. 4 left).

Physical simulations, i.e., the evaluation of the effect of initiation defect depth on defect opening during upsetting, demonstrated that crack opening width is influenced, among other factors, by the depth of the initiation defect and the applied deformation.

The industrial upsetting process leads to a significantly greater opening of initiation cracks. To increase the "sensitivity" of the physical simulation, it is recommended to use higher samples with the current tool design, thereby achieving greater deformation. It can be assumed that the extent of defect opening will then approach the values observed in industrially upset wires. Based on the analysis, a sample height of 16 mm is recommended.

## References

[1] Holý, M., Kolísko, J., Čítek, D., Řeháček, S., Ryjáček, P. Mosty z předpjatého betonu na železnici v ČR. *Beton*. 2023, 3, 52 - 56
[2] Šafář, R. Hodnocení technického stavu železničních mostů z předpjatého betonu. Habilitační práce, Praha, 2017
[3] Quilligan, A., O'Connor, A., Pakrashi. V. Fragility Analysis of Steel and Concrete Wind Turbine Towers. *Engineering Structures*, 2012, 36, 270-282
[4] Schmitz, G. Design and Experimental Validation of 328 ft (100 m) Tall Wind Turbine Towers Utilizing High Strength and Ultra-high Performance Concrete. Graduate Theses and Dissertations, Iowa State University, 2013
[5] [Online] Available: https://dywidag.com/products/external-post-tensioning-systems/unbonded-pt-system-using-wire
[6] EN 10138-2
[7] Magura, D., D., Sözen, M., A., Siess, Ch. P. A Study of Stress Relaxation in Prestressing Reinforcement. *PCI Journal*, Portland Cement Association a University of Illinois, 1964
[8] Podolny, W. Jr., Melville, T. Understanding the Relaxation in Prestressing. *PCI Journal*, Prestressed Concrete Institute, 1969
[9] Burgoyne, Ch., Sutherland, R. Why did Palau Bridge collapse? The Structural Engineer, 2006, 28 - 34.
[10] [Online] Available: https://www.keyence.eu/
[11] Sowerby, R., Chandrasekaran, N. The Cold Upsetting and Free Surface Ductility of Some Commercial Steels. *Journal of Applied Metalworking*. 1984, 3, 257–263
[12] Sarruf, Y. Criteria and Tests for Cold Headability. *Diploma Thesis*. Department of Mining and Metallurgical Engineering, Montreal, Canada, 2000
[13] Hyun Moo Baek, Young Gwan Jin, Sun Kwang Hwang, Yong-Taek Im, Il-Heon Son, Duk-Lak Lee. Numerical study on the evolution of surface defects in wire drawing. *Journal of Materials Processing Technology*, 2012, 776 - 785
[14] Toribio, J., Matos, J.C., González, B. Influence of surface defects on the fatigue crack initiation, Published by EDP Sciences, 2014
[15] Almotham, Saad N. An Evaluation of Microstructural Factors Affecting Cold Headability of Medium Carbon Steels. Colorado School of Mines, 2013
[16] KOBAYASHI, Shiro, OH, Soo-Ik a ALTAN, Taylan. Metal Forming and the Finite-Element Method, Oxford University Press, 1989

Hutnické listy – *Metallurgical Journal*
Speciální vydání / Special Issue, roč. / vol. LXXIX
ISSN Online: 3029-8350

# Accelerating Steel Casting CFD with Machine Learning

# Urychlení CFD simulací odlévání oceli pomocí strojového učení

**Josef Mergl[1], Alija Vila[1], Ali Abbas[1], Adnan Husakovic[1]**

[1] Primetals Technologies Austria GmbH, Turmstraße 44, 4031 Linz, Austria; *Corresponding author: josef.mergl@primetals.com

### Abstract

*Computational Fluid Dynamics (CFD) is a critical tool for understanding flow behaviour in continuous steel casting, but high-fidelity simulations remain computationally intensive and time-consuming. This work presents a machine learning-based framework to accelerate CFD simulations by integrating reduced order modelling (ROM) with data-driven surrogate models. Using high-resolution CFD data, we show a workflow that trains machine learning models to approximate transient flow fields with high accuracy at a fraction of the computational cost. The resulting hybrid models aim to enable near real-time predictions of key process variables while preserving physical fidelity. This approach offers significant potential for in-line process optimization, faster design iterations, and intelligent control in modern steelmaking operations.*

***Keywords**: CFD simulations, reduced order modelling, machine learning, continuous casting*

### Abstrakt

*Výpočetní dynamika tekutin (CFD) je klíčovým nástrojem pro pochopení chování proudění při kontinuálním odlévání oceli, avšak vysoce přesné simulace zůstávají výpočetně i časově náročné. Tato práce představuje rámec založený na strojovém učení, který urychluje CFD simulace integrací modelování sníženého řádu (ROM) s datově řízenými náhradními modely. S využitím CFD dat s vysokým rozlišením je ukázán pracovní postup, jenž umožňuje trénování modelů strojového učení k aproximaci přechodových proudových polí s vysokou přesností při zlomek výpočetních nákladů. Výsledné hybridní modely umožňují téměř reálné predikce klíčových procesních veličin při zachování fyzikální věrnosti. Tento přístup nabízí významný potenciál pro optimalizaci procesů v reálném čase, rychlejší iterační návrhy a inteligentní řízení v moderních ocelářských provozech.*

***Klíčová slova:** CFD simulace, modelování se sníženým řádem, strojové učení, plynulé lití*

## 1. Introduction

Continuous casting processes in steel manufacturing involve complex unsteady flows of molten metal within molds, influenced by nozzle design, casting speed, applied magnetic fields, and mold geometry. CFD is indispensable for optimizing these processes but remains impractical for real-time applications due to high computational costs.

To meet industrial demands for faster design iteration and intelligent control, ROMs aim to compress high-dimensional CFD data into compact representations without compromising critical flow features. In steel plants, such models could be deployed for:

- Real-time control of mold filling and solidification,
- Predictive maintenance based on flow patterns,
- Fast prototyping of casting parameters and designs.

Hutnické listy – *Metallurgical Journal*
Speciální vydání / Special Issue, roč. / vol. LXXIX
ISSN Online: 3029-8350

Recent developments in machine learning (ML) have significantly enhanced the capabilities of ROM for fluid dynamics, particularly in steel casting applications. These advancements aim to improve generalizability, computational efficiency, and the ability to capture complex flow behaviors. Key approaches include:

- **Dynamic Mode Decomposition (DMD):** A data-driven technique that decomposes transient flow fields into coherent structures governed by linear dynamics. DMD is particularly effective for analyzing laminar flows or systems where linear approximations are valid [1]. For parametric DMD, see e.g. [2].
- **Convolutional Residual Networks (ConvResNet):** By leveraging convolutional layers and residual connections, ConvResNets can capture spatial hierarchies and temporal dependencies in fluid flow data, making them suitable for modelling intricate flow patterns [3].
- **Neural Ordinary Differential Equations (Neural ODEs):** These models represent time-continuous latent dynamics through differential equations embedded within neural networks, allowing for flexible modelling of temporal evolution in dynamical systems [4].
- **Fourier Neural Operators (FNOs):** FNOs learn mappings between input functions and solutions to partial differential equations (PDEs) across varying parameter spaces, enabling efficient and accurate predictions of complex, nonlinear flow behaviors [5].
- **PDE-Preserving Neural Networks (PPNN):** PPNNs integrate discretized PDE operators directly into the neural network architecture, resulting that the learned models tend to fulfill the underlying physical laws better, thereby enhancing accuracy and generalizability [3].
- **NeuralDEM:** An end-to-end deep learning approach designed to replace traditional Discrete Element Method (DEM) simulations. NeuralDEM models particulate flows by treating the Lagrangian discretization as a continuous field and incorporating macroscopic behavior, enabling real-time simulations of industrial-scale particulate systems [6].

These ML-based ROM techniques offer promising avenues for accelerating CFD simulations in steel casting, with each method providing unique advantages depending on the specific flow characteristics and modelling requirements. Moreover, in [3] you can find a comparison of several different methods.

In this paper, only results of DMD and ConvResNet are discussed since some of the methods mentioned are more involved to implement/use.

## 2. Methodology

Integrating CFD- simulations with ML provides a powerful approach for predicting complex physical behaviors without the need for repeated high-cost simulations. The workflow begins with CAD model creation and proceeds through mesh generation and CFD simulations, followed by data preprocessing and ML model training. This enables faster design iterations and optimization. The **Fig. 1** illustrates the complete pipeline from CAD modelling to ML model development using CFD-generated data.

Hutnické listy – *Metallurgical Journal*
Speciální vydání / Special Issue, roč. / vol. LXXIX
ISSN Online: 3029-8350

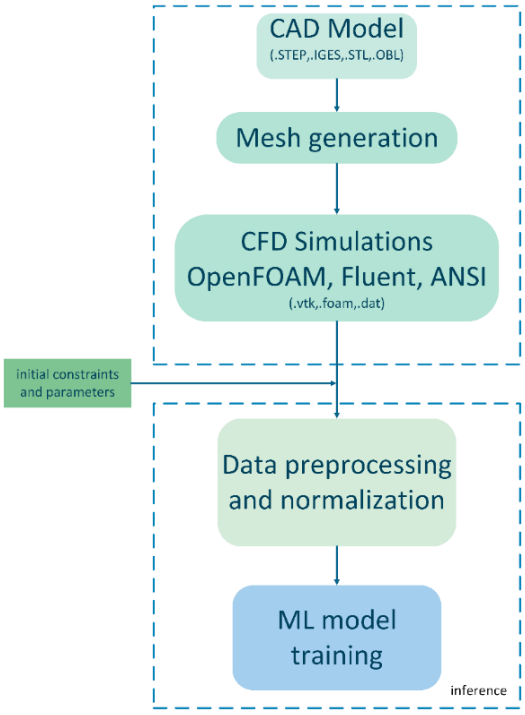


**Fig. 1** End-to-end workflow for ML model development using CFD simulation data

**Obr. 1** Komplexní pracovní postup pro vývoj modelů strojového učení s využitím dat ze simulací CFD

### 2.1 Governing Equations for Mold Flow

The Navier-Stokes equations are highly nonlinear and lack analytical solutions for most practical flows, so CFD employs the finite volume method to solve them numerically with conservation laws applied over discrete control volumes. In this study, Navier-Stokes equations are formulated under the assumptions of an incompressible, single-phase fluid that remains at a constant temperature throughout the flow. The continuity equation (1):

$$\nabla \cdot v = 0 \tag{1}$$

represents the conservation of mass, stating that the divergence of the velocity field $\mathbf{v}$ is zero for incompressible flows. The momentum equation (2) is given as:

$$\partial v/\partial t + (v \cdot \nabla)v = -1/\rho \nabla p + \nu_{eff} \nabla^2 v + f \tag{2}$$

where $\rho$ is the liquid steel density, $p$ is the pressure, $\nu_{eff} = \nu + \nu_t$ is the effective viscosity, with $\nu$and $\nu_t$ being the molecular and turbulent viscosity and $f$ represents the body forces.

In the case of mold flow, due to the high momentum of jets exiting the submerged entry nozzle (SEN), the flow of liquid steel is strongly turbulent. Turbulent flows involve a wide range of interacting scales in time and space. Here, this behavior is captured using the Reynolds-averaged Navier-Stokes equations (RANS). For turbulence closure, the two-equation eddy-viscosity approach, Shear Stress Transport (SST) k - ω model was employed.

Hutnické listy – *Metallurgical Journal*
Speciální vydání / Special Issue, roč. / vol. LXXIX
ISSN Online: 3029-8350

### 2.2 Data Preparation

High-fidelity 3D simulations were conducted under various casting speeds, submergence depths and magnetic fields. 2D slices (e.g., mid-plane horizontal cross-sections) were extracted for training to reduce complexity while preserving dominant dynamics. One snapshot (see **Fig. 2**) every 0.1 s is taken over a total time of 60 s, which leads to a total of 601 snapshots per parameter set. In each 2D slice, the three velocity components are stored anyway and used for training the models.

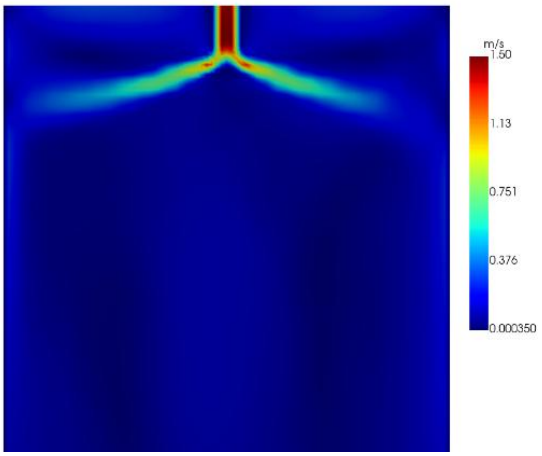


**Fig. 2** Single snapshot of simulation. Shown is the absolute velocity combined from the three velocity components. The red part indicates where the entry nozzle is

**Obr. 2** Samostatný snímek ze simulace. Zobrazena je absolutní rychlost, která je součtem tří složek rychlosti. Červená část označuje polohu vstupní trysky

### 2.3 Dynamic Mode Decomposition (DMD)

DMD approximates flow evolution using a linear operator A (3):

$$x_{k+1} \approx Ax_k \tag{3}$$

where snapshots $x_k$ are flattened flow fields.

DMD excels at identifying laminar structures and oscillatory behavior, providing interpretable, low-rank models. For each simulation, one DMD model is trained and for new parameters, those models are interpolated, see e.g. [2] for more details.

### 2.4 Convolutional Residual Networks (ConvResNet)

ConvResNets integrate convolutional layers with residual (skip) connections, enabling the training of deeper networks by mitigating issues like vanishing gradients. In fluid dynamics, they effectively capture spatial hierarchies and temporal dependencies, making them suitable for modelling complex, nonlinear flow behaviors. By learning residual mappings, ConvResNets enhance generalization and stability in reduced-order modelling of unsteady flows.

Hutnické listy – *Metallurgical Journal*
Speciální vydání / Special Issue, roč. / vol. LXXIX
ISSN Online: 3029-8350

## 3. Application and Results

### 3.1 Experimental Setup

- Training set: 12 high-resolution 3D mold flow simulations.
- Parameters: Inlet speed, nozzle submergence depth, applied magnetic field strength.
- Models: DMD (linear), ConvResNet.
- Model input: parameters (and initial snapshot for ConvResNet).
- Model output: Multi-step flow predictions.

### 3.2 Use of 2D Slices: Benefits and Limitations

Advantages:

- Lower memory and faster training.
- Good approximation for centerline symmetry flows.

Disadvantages:

- - May miss 3D effects (e.g., swirl, asymmetry).
- - Reduces physical completeness.

### 3.3 Results

DMD captured dominant laminar features well but deteriorated in turbulent regimes due to linearity limitations. However, in the tests conducted using parametric DMD, speed up factors of up to 50 were observed compared to traditional simulations.

**Fig. 3** shows an example, where the interpolation seems to capture the dynamics in the mold quiet well. However, if we examine **Fig. 4**, we see that sometimes non-physical behavior can occur, depicted in this case as one jet splitting into two jets (right side of the right picture).

ConvResNet achieved lower relative errors in transient and nonlinear flow settings. It generalized across untrained parameters at least for the first few snapshots. The speedup is considerable with a factor of 1000. But after some time, error accumulation becomes a big issue with ConvResNet. This is a common problem with so called autoregressive neural networks.

In fact, ResNets can be interpreted as the explicit Euler method for an ordinary differential equation [4]. **Fig. 5** shows a result after short time, where it still produced seemingly good results, however, **Fig. 6** shows the result after 10 s and there already, a huge error accumulation took place and the result is not reliable at all.

Hutnické listy – *Metallurgical Journal*
Speciální vydání / Special Issue, roč. / vol. LXXIX
ISSN Online: 3029-8350

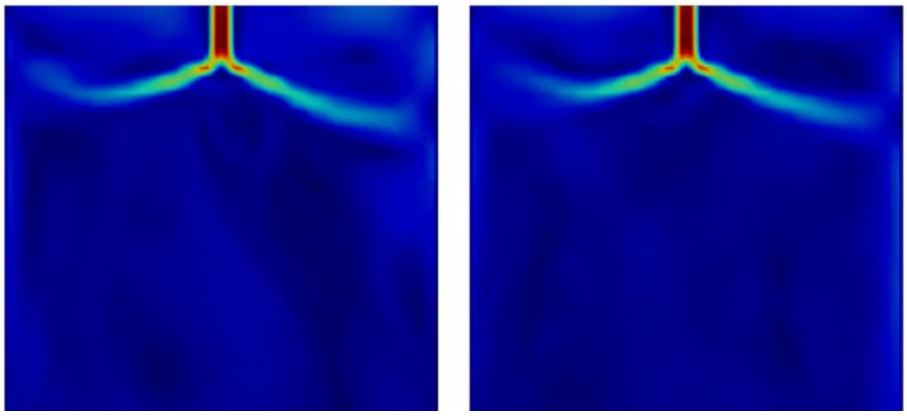

**Fig. 3** Snapshots after 10 s real life runtime (corresponds to 100 snapshots). Left. Simulation using the parameters 1.5 m/s casting speed, 1500 mm casting length, 225 mm width, and 160 mm entry nozzle submergence depth. Right. Interpolation using two simulations

**Obr. 3** Snímky po 10 sekundách reálného výpočtu (odpovídá 100 snímkům). Vlevo: Simulace s parametry: rychlost lití 1,5 m/s, délka lití 1500 mm, šířka 225 mm a hloubka ponoření vstupní trysky 160 mm. Vpravo: Interpolace na základě dvou simulací

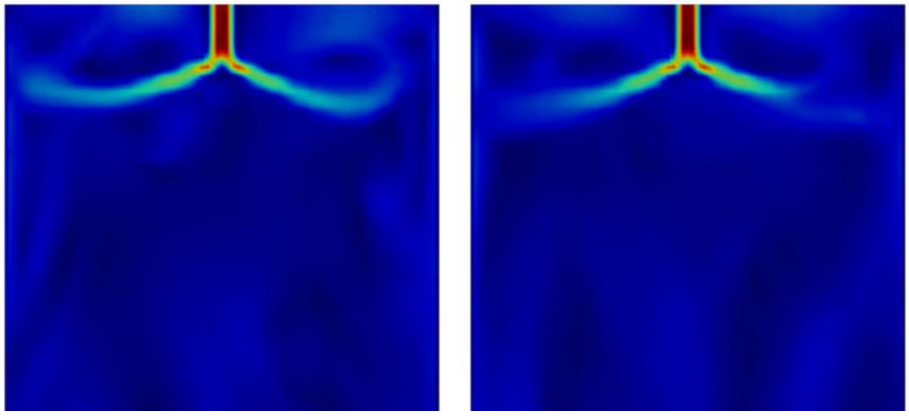

**Fig. 4** Same case as in Fig. 2, but after approximately 3 seconds

**Obr. 4** Stejný případ jako na obr. 2, avšak po přibližně 3 sekundách

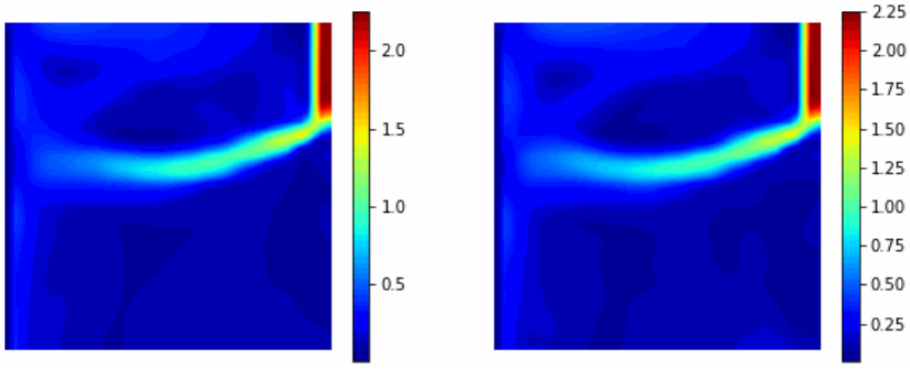


**Fig. 5** Snapshots after 3 s real life runtime (corresponds to 30 snapshots). Left. Simulation using the parameters 1.5 m/s casting speed, 1500 mm casting length, 225 mm width, and 190 mm entry nozzle submergence depth. Right. Interpolation, where ConvResNet was

**Obr. 5** Snímky po 3 sekundách reálného výpočtu (odpovídá 30 snímkům). Vlevo: Simulace s parametry: rychlost lití 1,5 m/s, délka lití 1500 mm, šířka 225 mm a hloubka ponoření vstupní trysky 190 mm. Vpravo: Interpolace, kde byl použit model ConvResNet

Hutnické listy – *Metallurgical Journal*
Speciální vydání / Special Issue, roč. / vol. LXXIX
ISSN Online: 3029-8350

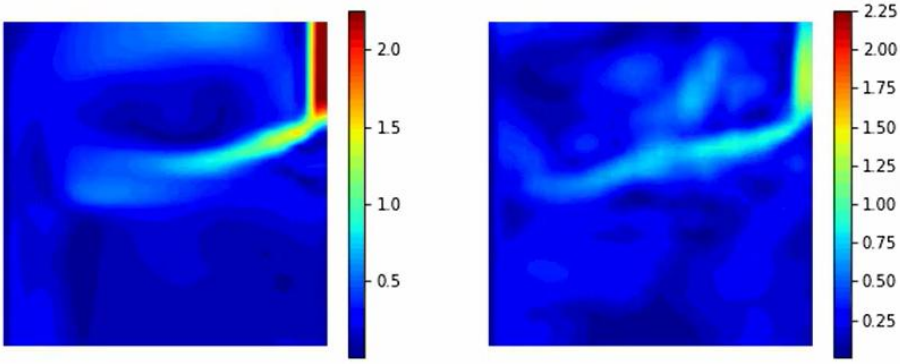


**Fig. 6** Same case as in Fig. 4, but after approximately 6 s

**Obr. 6** Stejný případ jako na obr. 4, avšak po přibližně 6 sekundách

## 4. Conclusion and Outlook

- This work presents a hybrid approach combining ROM with ML to accelerate CFD simulations in steel casting. DMD serves as a fast baseline for laminar flows, capturing average flow behavior but often lacking physical accuracy and turbulent structures.
- ConvResNet effectively model nonlinear and transient dynamics across parameter variations in the early stages of simulation, though they suffer from error accumulation over time due to their stepwise prediction structure. While ML-based ROMs offer significant computational speed-ups, challenges remain in modelling fully turbulent flows, scaling to 3D domains, and preserving physical consistency.
- Future work will focus on integrating physics-aware 3D architectures, developing hybrid models that embed PDE knowledge, and applying these tools for real-time control and defect prediction in casting processes.

## References

[1] Schmid Peter J. Dynamic Mode Decomposition and Its Variants. 2022. Vol. 54. p 225-254. DOI https://doi.org/10.1146/annurev-fluid-030121-015835

[2] Andreuzzi Francesco and Demo Nicola and Rozza Gianluigi. A Dynamic Mode Decomposition Extension for the Forecasting of Parametric Dynamical Systems. 2023. Vol. 22. p 2432-2458. DOI 0.1137/22M1481658

[3] Liu Xin-Yang and Zhu Min and Lu Lu and Sun Hao and Wang Jian-Xun. Multi-resolution partial differential equations preserved learning framework for spatiotemporal dynamics. 2024. Vol. 7. DOI 10.1038/s42005-024-01521-z

[4] Ricky T. Q. Chen and Yulia Rubanova and Jesse Bettencourt and David Duvenaud. Neural Ordinary Differential Equations. 2019. Available from: https://arxiv.org/abs/1806.07366

[5] Zongyi Li and Nikola Kovachki and Kamyar Azizzadenesheli and Burigede Liu and Kaushik Bhattacharya and Andrew Stuart and Anima Anandkumar. Fourier Neural Operator for Parametric Partial Differential Equations. 2021. Available from: https://arxiv.org/abs/2010.08895

[6] Benedikt Alkin and Tobias Kronlachner and Samuele Papa and Stefan Pirker and Thomas Lichtenegger and Johannes Brandstetter. NeuralDEM -- Real-time Simulation of Industrial Particulate Flows. 2025. Available from: https://arxiv.org/abs/2411.09678

Hutnické listy – *Metallurgical Journal*
Speciální vydání / Special Issue, roč. / vol. LXXIX
ISSN Online: 3029-8350

# Advanced Simulation Methods for Bulk Material Processing in Metallurgy and Metalworking

# Pokročilé simulační metody pro zpracování sypkých materiálů v metalurgii a kovozpracujícím průmyslu

**Jiří Dobiáš[1], Jakub Hlosta[1]**

[1] VSB-TUO, HGF, 17. listopadu 2172/15, 708 00 Ostrava-Poruba. *Contact e-mail: jiri.dobias@vsb.cz

**Abstract**

*This article explores the use of advanced digital modelling techniques – Discrete Element Method (DEM), Finite Element Method (FEM), and Computational Fluid Dynamics (CFD) – in optimizing metallurgical processes and equipment design. These methods enable detailed simulation of bulk material behaviour, structural responses, and thermal dynamics, replacing traditional empirical approaches. Their integration allows for multiphysics analyses that improve efficiency, reduce energy consumption, and minimize prototyping costs. Practical applications, such as those at VSB – Technical University of Ostrava, demonstrate the value of these tools in industrial settings. The integration of simulation tools with real-time data and digital twins is driving a shift toward smarter, more adaptive, and environmentally sustainable metallurgical processes.*

***Keywords:*** *Discrete Element Method (DEM); Finite Element Method (FEM); Fluid Dynamics (CFD); bulk material simulation; process optimization*

**Abstrakt**

*Tento článek se zabývá využitím pokročilých technik digitálního modelování – metody diskrétních prvků (DEM), metody konečných prvků (FEM) a výpočetní dynamiky tekutin (CFD) – při optimalizaci metalurgických procesů a konstrukce zařízení. Tyto metody umožňují podrobnou simulaci chování sypkých materiálů, strukturálních reakcí a tepelné dynamiky a nahrazují tradiční empirické přístupy. Jejich integrace umožňuje multifyzikální analýzy, které zvyšují účinnost, snižují spotřebu energie a minimalizují náklady na prototypování. Praktické aplikace, například na Vysoké škole báňské – Technické univerzitě v Ostravě (VŠB-TUO), demonstrují přínos těchto nástrojů v průmyslovém prostředí. Integrace simulačních nástrojů s daty v reálném čase a digitálními dvojčaty podporuje posun směrem k inteligentnějším, adaptivnějším a environmentálně udržitelným metalurgickým procesům.*

***Klíčová slova:*** *metoda diskrétních prvků (DEM); metoda konečných prvků (FEM); dynamika tekutin (CFD); simulace sypkých materiálů; optimalizace procesů*

## 1. Introduction

Digitization and Industry 4.0 principles are becoming an integral part of all industrial sectors, including metallurgy and metalworking. In these areas, efficient processing and handling of bulk materials such as ores, powders, slags, and additives are key to ensuring product quality and economic viability. Traditionally, the design of process and transport equipment has relied on empirical equations and the experience of engineers. However, modern tools such as 3D CAD/CAM systems and numerical simulations have brought fundamental changes to the design process.

Hutnické listy – *Metallurgical Journal*
Speciální vydání / Special Issue, roč. / vol. LXXIX
ISSN Online: 3029-8350

## 2. Simulation of Bulk Material Behaviour Using DEM

One of the most progressive numerical approaches is the Discrete Element Method (DEM). This method is based on the modelling of individual particles and their mutual interactions, allowing for accurate simulations of the dynamic flow of particulate matter in transportation, mixing, storage, and processing systems. DEM has gradually become a common tool in industrial design and research, enabling the prediction of behaviour and optimization of equipment before costly prototypes are manufactured. In metallurgy and materials engineering, DEM is used for designing mixers, feeders, and furnaces for particulate and granular substances. With properly defined input material parameters – such as particle size, shape, moisture, internal and external friction angle, cohesion, and flowability – DEM allows virtual testing of system functionality and optimization of machine geometry and processes [1, 4].

In addition to DEM, the Finite Element Method (FEM) is also widely used, particularly for analysing structural elements of processing machines. FEM enables the calculation of stresses, deformations, natural frequencies, and thermal expansion in critical parts. Combined with DEM, it allows for complex multi-physical simulations – e.g., applying forces from virtual particles in DEM to structural elements modelled in FEM, thus identifying critical stress locations or optimizing wall thickness. In **Fig. 1** DEM simulation of material flow from hopper is depicted. Colours represent different particle velocities. By combining DEM with FEM, the researchers can simulate not only the motion of particles but also the thermal and mechanical effects acting on them. This hybrid approach provides a comprehensive view of the process, enabling optimization of design and operation parameters in real industrial applications.

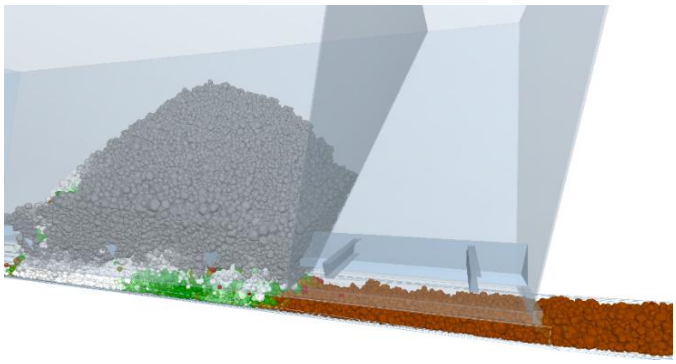

**Fig. 1** Hopper simulation

**Obr. 1** Simulace násypky

## 3. Thermal Process Simulation

Understanding the thermal behaviour of materials is crucial for metallurgical processes. Bulk materials such as ores, agglomerates, and slags are routinely processed under high temperatures. Their thermal properties, including thermal conductivity, heat capacity, and moisture content, influence heat transfer and the efficiency of sintering, casting, or slag cooling operations.

Thermal process simulation in granular and particulate systems increasingly relies on the integration of Discrete Element Method (DEM), Finite Element Method (FEM), and Computational Fluid Dynamics (CFD).

Hutnické listy – *Metallurgical Journal*
Speciální vydání / Special Issue, roč. / vol. LXXIX
ISSN Online: 3029-8350

This multiscale, multiphysics approach enables a detailed investigation of heat transfer mechanisms, including particle-to-particle conduction, convective exchange with the surrounding gas, and thermal radiation, especially under high-temperature conditions. Such coupled models are essential for simulating industrial processes like sintering, calcination, pyrolysis, and thermal reduction, where the behaviour of individual particles interacts dynamically with gas flows and thermal gradients. DEM is used to capture the kinematics and contact mechanics of the particles, FEM provides insight into internal temperature distributions and structural responses, while CFD resolves the fluid flow, turbulence, and thermal fields in the gas phase.

Such models are particularly useful for optimizing furnace designs, reducing energy consumption, and improving thermal stability [3]. Studies have demonstrated how CFD-DEM coupling can accurately predict temperature evolution, residence times, and particle trajectories in rotary kilns, fluidized beds, or packed reactors [2]. These simulations also help identify hot spots, assess energy efficiency, and optimize reactor designs. In **Fig. 2** screw cooler DEM simulation can be seen, where colours represent different temperatures of particles.

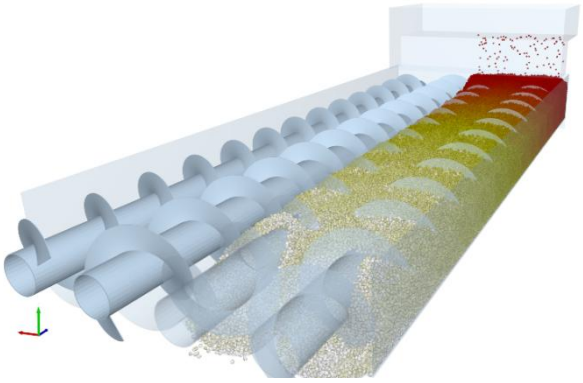

**Fig. 2** Screw cooler simulation

**Obr. 2** Simulace šnekového chladiče

In the future, integration of real-time data and adaptive digital twins could enable dynamic control of thermal processes. By linking live sensor inputs with simulation models, these systems can respond to changing conditions, detect anomalies early, and optimize operations in real time improving energy efficiency, product quality, and overall process stability.

## 4. Applications in Metallurgy and Process Engineering

In metalworking and steel production, bulk materials are used in processes such as sintering, smelting, and casting. These processes are demanding in terms of mechanical and thermal load on the materials and devices. DEM can be used to evaluate mechanical stress on linings, screens, and feeding systems, while also identifying potential operational issues such as clogging, uneven mixing, or excessive wear. Such modelling supports the design of systems with longer service life and reduced operational costs.

The Centre of Bulk Solids at VSB – Technical University of Ostrava plays a leading role in this area in the Czech Republic. It focuses on the study of bulk material behaviour and transport systems, conducts measurements of mechanical-physical properties of bulk materials and supplies input parameters for DEM and other simulation tools.

Hutnické listy – *Metallurgical Journal*
Speciální vydání / Special Issue, roč. / vol. LXXIX
ISSN Online: 3029-8350

It collaborates closely with industrial partners to improve process efficiency, reduce energy consumption, and enhance product quality. The centre uses high-performance computing to simulate granular flow, contact forces, thermal behaviour, and wear mechanisms in equipment such as rotary kilns, screw conveyors, and ball mills. It also develops patented innovations in handling technologies and provides comprehensive consulting and design services for industrial partners.

## 5. Conclusion

The combination of DEM and FEM methods represents a powerful tool for the design, optimization, and diagnostics of equipment and processes in metallurgy and metalworking. When coupled with thermal simulations and CFD analysis, these digital methods provide a detailed understanding of heat transfer, fluid flow, and material behaviour under complex conditions – especially in high-temperature environments. This holistic modelling approach enables engineers to predict critical parameters such as temperature gradients, stress distributions, and flow instabilities, leading to more accurate and efficient process control.

Thanks to numerical modelling, it is possible to minimize prototyping costs, shorten development cycles, and enhance the competitiveness of industrial products. Moreover, the integration of real-time data and adaptive digital twins brings new opportunities for dynamic optimization, predictive maintenance, and sustainability improvements. The convergence of DEM, FEM, CFD, and thermal analysis is thus transforming traditional process design into a data-driven, intelligent system. The adoption of these digital methods into engineering practice is not just a trend but a key pillar for innovation, efficiency, and environmental responsibility in modern metallurgy and manufacturing.

### Acknowledgements

***This paper was created as part of the project No. CZ.02.01.01/00/22_008/0004631 Materials and technologies for sustainable development within the Jan Amos Komensky Operational Program financed by the European Union and from the state budget of the Czech Republic, and project The European Just Transition Fund supported this work within the Operational Programme Just Transition under the aegis of the Ministry of the Environment of the Czech Republic, project CirkArena, number CZ.10.03.01/00/22_003/0000045.***

***Work was also supported by Grant of SGS No. SP2025/005 Development of measuring apparatus for determination of thermodynamic properties of mineral raw materials for design of process and treatment plants, Faculty of Mining and Geology, VSB - Technical University Ostrava, Czech Republic.***

### References

[1] CLEARY, Paul, 2004. Large scale industrial DEM modelling. Engineering Computations, 21(2), pp.169–204. DOI: 10.1108/02644400410519730.

[2] HLOSTA, Jakub, ČERMÁK, Martin, ROZBROJ, Jiří and ŽUROVEC, David, 2019. CFD-DEM numerical model of laboratory scale fluidized bed coffee roaster. AIP Conference Proceedings, 2116(1), 320004. DOI: 10.1063/1.5114326.

[3] HOU, Qinfu et al., 2015. Particle scale study of heat transfer in packed and fluidized beds. In: G. B. MARIN and J. LI, eds. Advances in Chemical Engineering. Volume 46. Academic Press, pp. 193–243. ISSN 0065-2377. ISBN 9780128012475. DOI: 10.1016/bs.ache.2015.10.006.

[4] ZHU, H. P., ZHOU, Z. Y., YANG, R. Y. and YU, A. B., 2007. Discrete particle simulation of particulate systems: theoretical developments. Chemical Engineering Science, 62(13), pp.3378–3396. ISSN 0009-2509. DOI: 10.1016/j.ces.2006.12.089.

# invent arena

Mezinárodní výstava technických novinek, patentů a vynálezů

## 17. - 18. června 2026

WERK ARENA Třinec

**VSTUP ZDARMA**

**Program pro rodiny s dětmi / odbornou i širokou veřejnost**

**TATRA TRUCKS**
Projížďka v závodním speciálu

**GYROSKOP**
Staňte se astronautem

**Den s IZS**
112 v praxi

**ARMÁDA ČR**
Nejmodernější vojenské technologie


**STUDENT CAR**
Od návrhu po realitu

**MOBILNÍ BIATLON**
Objevte svůj nový talent

**PANELOVÉ DISKUZE S EXPERTY**
Pro všechny, kteří chtějí být o krok napřed

invent arena

inventarena.cz

# ČESKÁ HUTNICKÁ SPOLEČNOST
CZECH METALLURGICAL SOCIETY

**podpora a popularizace výzkumu, vývoje a inovací**
**propagace studia technických oborů**
**organizování kulturně vzdělávacích produkcí**
**podpora zlepšovatelství**
**odborné výstavy, semináře, konference**
**lektorská činnost**

## Českou hutnickou společnost podporují:

- TŘINECKÉ ŽELEZÁRNY
- STROJÍRNY A STAVBY TŘINEC
- ENERGETIKA TŘINEC AKCIOVÁ SPOLEČNOST
- Šroubárna Kyjov, spol. s r.o.
- TŘINECKÁ PROJEKCE TP A.S.
- SLÉVÁRNY TŘINEC, a.s.
- Třinecký inženýring, a.s.
- VÚHŽ a.s.
- BOHEMIA RINGS
- ENVIFORM

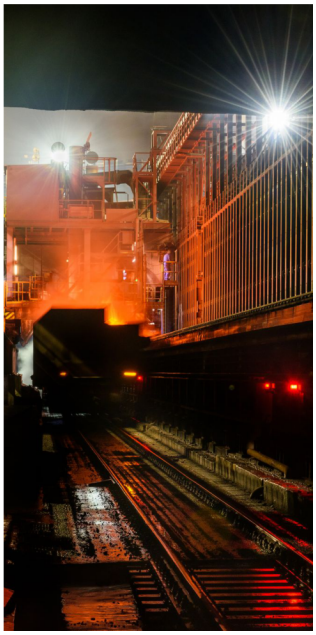

www.hutnickaspol.cz

PredsedaCHS@trz.cz